Stony Brook University

Transport Studies of Superconducting Materials

A Dissertation Presented

by

Cheng Zhang

to

The Graduate School

in Partial Fulfillment of the

Requirements

for the Degree of

Doctor of Philosophy

in

Materials Science and Engineering

Stony Brook University

August 2016

Stony Brook University

The Graduate School

Cheng Zhang

We, the dissertation committee for the above candidate for the

Doctor of Philosophy degree, hereby recommend

acceptance of this dissertation.

Dr. Qiang Li – Dissertation Advisor
Scientist, Brookhaven National Laboratory
Adjunct Professor of Materials Science and Engineering, Stony Brook University

Dr. Dilip Gersappe –Chairperson of Defense
Professor of Materials Science and Engineering

Dr. Genda Gu
Scientist, Brookhaven National Laboratory
Adjunct Professor of Materials Science and Engineering, Stony Brook University

Dr. Jie Wu
Scientist, Brookhaven National Laboratory

This dissertation is accepted by the Graduate School

Nancy Goroff

Interim Dean of the Graduate School

Abstract of the Dissertation

Transport Studies of Superconducting Materials

by

Cheng Zhang

Doctor of Philosophy

in

Materials Science and Engineering

Stony Brook University

2016

Superconducting materials are promising for future applications on energy transport and storage. The key properties for superconductors are critical temperature T_c, critical current density J_c and upper critical field H_{c2}. In this dissertation, detailed transport studies were performed on two superconducting materials: $FeSe_{0.5}Te_{0.5}$ thin films and the second generation $YBa_2Cu_3O_{7-\delta}$ coated conductors, in order to determine what limits the broad applications of these superconductors.

High quality of $FeSe_{0.5}Te_{0.5}$ thin films were grown by pulsed laser deposition. Low temperature oxygen annealing and proton irradiation were conducted on the films, as the post-treatment techniques in order to improve the transport performance. J_c at self-field was doubled, reaching ~3 MA/cm^2 in oxygen annealed films. An overall enhancement of in-field J_c was observed as well. An even greater enhanced J_c at high field was achieved in proton irradiated films,

simultaneously with a T_c enhancement, rather than the degradation commonly found after irradiation in cuprate superconductors. The enhancement of the irreversibility field and upper critical filed is also observed in the irradiated films. Low temperature oxygen annealing and proton irradiation are both controllable and cost-efficient ways to enhance the J_c performance of $FeSe_{0.5}Te_{0.5}$ thin films, making this class of material very promising in potential high field applications.

Gold ion irradiation was performed on second generation $YBa_2Cu_3O_{7-\delta}$ coated conductors. At the optimized dosage of 2×10^{11} cm^{-2}, J_c performance under the field of 3 T was significantly enhanced by 70%, 98% and 64% at 5 K, 30 K and 77 K, respectively. Though reduced after irradiation, T_c and self-field J_c in the samples can be effectively recovered by post-oxygen annealing. J_c at 77 K can also be further enhanced by post-oxygen annealing for samples irradiated at certain dosages. This ion irradiation technique is now developed into the reel-to-reel method for high performance mass produced second generation coated conductors.

Transport Studies of Superconducting Materials

List of Figures

List of Tables

Acknowledgments

First of all, I'm sincerely grateful to my dissertation advisor Dr. Qiang Li. As a student jumped into this field, I would have no chance to finish the PhD study without his continuously encouraging and support. During the PhD study, I have been learning not only the scientific knowledge and experimental skills from him, but also the ways and attitudes dealing with varies issues in practical world. It is an invaluable experience and will help me throughout my entire life.

I want to thank my colleagues in the group. Dr. Weidong Si has provided tremendous help during my entire PhD study on the aspect of laser system and thin film synthesis. Every discussion with him benefited me not only on knowledge, but also serious scientific attitude. I learned a lot from Dr. Xiaoya Shi about varies equipment set-up and maintenance, as well as the brilliant idea unifying lab experiments and cooking. I'm also deeply impressed by Dr. Toshinori Ozaki for his hard working and dedication on scientific research. He sets a very good example for me. Dr. Hang Chi helped me a lot on academic writing. He always keeps an optimistic view against any upcoming difficulties, which is something I would try my best to learn.

I want to thank my department, the Department of Materials Science and Engineering in Stony Brook University, for giving me the opportunity to pursue both my master's and doctor's degree in the United States. Professor Dilip Gersappe is the

one I want to give my special thanks. He has been giving very helpful advices on every step I have taken.

I'm also indebted to my collaborators and friends in Brookhaven National Laboratory. I want to thank Dr. Genda Gu and Ruidan Zhong for their help on crystal growth, Dr. Wei Ku, Dr. John Tranquada, Dr. Tonica Valla, Dr. Lijun Wu, Dr. Jie Wu and Xugang He for all those helpful discussions.

Finally I want to give my sincere thanks to my family who are always supporting me during the study. My wife Chen Liang stands behind me trusting all the choices I made, keeping me encouraged every time the difficulty comes. She is on my side no matter what happens. I give my thanks to my parents for allowing me to go abroad and constantly supporting me from the other side of the earth, leaving themselves lonely without their only child. I cannot complete my study without their love.

Publications

Published:

1 Q. Li, D. E. Kharzeev, **C. Zhang**, Y. Huang, I. Pletikosic, A. V. Fedorov, R. D. Zhong, J. A. Schneeloch, G. D. Gu, and T. Valla., *Nat. Phys.* **12**, 550 (2016).

2 Y. Zou, X. Qi, **C. Zhang**, S. Ma, W. Zhang, Y. Li, T. Chen, X. Wang, Z. Chen, D. Welch, P. Zhu, B. Liu, Q. Li, T. Cui, and B. Li, *Sci. Rep.* **6**, 22330 (2016).

3 X. Shi, J. Yang, L. Wu, J. R. Salvador, **C. Zhang**, W. L. Villaire, D. Haddad, J. Yang, Y. Zhu, and Q. Li, *Sci. Rep.* **5**, 14641 (2015).

4 R. Zhong X. He, J. A. Schneeloch, C. Zhang, T. Liu, I. Pletikosić, T. Yilmaz, B. Sinkovic, Q. Li, W. Ku, T. Valla, J. M. Tranquada, and G. Gu, *Phys. Rev. B* **91**, 195321 (2015).

5 J. Wang, R. Zhong, S. Li, Y. Gan, Z. Xu, **C. Zhang**, T. Ozaki, M. Matsuda, Y. Zhao, Q. Li, G. Xu, G. Gu, J. M. Tranquada, R. J. Birgeneau, and J. Wen, *Phys. Rev. B* **91**, 014501 (2015).

6 A. L. Tiano, G. C. Papaefthymiou, C. S. Lewis, J. Han, **C. Zhang**, Q. Li, C. Shi, A. M. M. Abeykoon, S. J. L. Billinge, E. Stach, J. Thomas, K. Guerrero, P. Munayco, J. Munayco, R. B. Scorzelli, P. Burnham, A. J. Viescas, and S. S. Wong, *Chem. Mater.* **27**, 3572 (2015).

7 Y. Sun, Y. Tsuchiya, S. Pyon, T. Tamegai, **C. Zhang**, T. Ozaki, and Q. Li, *Supercond. Sci. Tech.* **28**, 015010 (2015).

8 W. Si, **C. Zhang**, L. Wu, T. Ozaki, G. Gu, and Q. Li, *Appl. Phys. Lett.* **107**, 092601 (2015).

9 W. Si, **C. Zhang**, X. Shi, T. Ozaki, J. Jaroszynski, and Q. Li, *Appl. Phys. Lett.* **106**, 032602 (2015).

10 R. D. Zhong, J. A. Schneeloch, X. Y. Shi, Z. J. Xu, **C. Zhang**, J. M. Tranquada, Q. Li, and G. D. Gu, *Phys. Rev. B* **88**, 020505 (2013).

11 J. Wen, S. Li, Z. Xu, **C. Zhang**, M. Matsuda, O. Sobolev, J. T. Park, A. D. Christianson, E. Bourret-Courchesne, Q. Li, G. Gu, D.-H. Lee, J. M. Tranquada, G. Xu, and R. J. Birgeneau, *Phys. Rev. B* **88**, 144509 (2013).

In Preparation:

1 **C. Zhang**, W. Si, and Q. Li, Doubling the critical current density in superconducting $FeSe_{0.5}Te_{0.5}$ thin film by low temperature oxygen annealing, *Appl. Phys. Lett.* (submitted).

2 T. Ozaki, L. Wu, **C. Zhang**, J. Jaroszynski, W. Si, J. Zhou, Y. Zhu, and Q. Li, A route for a strong increase of critical current in nano strained iron-based superconductors, *Nat. Commun.* (accepted).

3 Z. Chen, R. Chen, R. Zhong, J. A. Schneeloch, **C. Zhang**, Y. Huang, F. Qu, Q. Li, G. Gu and N. Wang, Spectroscopic evidence for bulk-band inversion and three-dimensional massive Dirac fermions in $ZrTe_5$, *Proc. Natl. Acad. Sci. USA* (submitted).

1. Introduction

1.1 History of superconductivity

In 1911, H. K. Onnes discovered the phenomenon of superconductivity and started an avalanche of research in physics and materials science.[1] Certain types of metals were found to exhibit no direct current electrical resistivity below a certain temperature, which is usually several Kelvin above absolute zero, later defined as the superconducting critical temperature, T_c. In 1933, W. Meissner and R. Ochsenfeld found that, along with the electrical superconducting, superconductors show perfect diamagnetic property and the magnetic flux is completely screened from the interior at the temperature below T_c.[2] It is another fundamental property of the materials in the superconducting state.

The interpretation to this superconducting state, the coexistence of zero resistivity and perfect diamagnetism, was first brought out by the London brothers with their two-fluid model in 1935.[3] The theory assumes the carriers consist of normal electrons and superconducting electrons. A temperature dependent value n_s was then introduced, standing for superconducting electron density. Penetration depth λ was defined as

$$\lambda = (m/\mu_0 n_s e^2)^{1/2} \tag{1.1}$$

where m is the electron mass, μ_0 is the vacuum permeability and e is the electron charge. It stands for the thickness of a thin layer that the magnetic flux can go inside a superconductor, following

$$\boldsymbol{J}_s = -(1/\mu_0\lambda^2)\boldsymbol{A} \tag{1.2}$$

where $\boldsymbol{J}_s$ is the supercurrent density, $\boldsymbol{A}$ is the magnetic vector potential $\boldsymbol{B} = \nabla \times \boldsymbol{A}$..

It was a big step forward to describe the crucial properties of superconducting materials, even though it did not consider that the density of superconducting electrons may depend on the magnetic field and spatial coordinate. These have been taken into account in Ginzburg-Landau equation carried out in 1950,[4] given as

$$(1/2m)(-i\hbar\nabla - 2e\boldsymbol{A})^2\psi(r) + \alpha\psi(r) + \beta|\psi(r)|^2\,\psi(r) = 0 \tag{1.3}$$

where $\hbar$ is the reduced Planck constant. The first and second expansion coefficients α and β were introduced to describe the spatial density of superconducting electrons

$$n_s = |\psi(r)|^2 \tag{1.4}$$

In the Ginzburg-Landau model, coherence length, λ, was defined as the length over which ψ varies in space

$$\xi \equiv (\hbar^2/2m\alpha)^{1/2} \tag{1.5}$$

In 1957, the microscopic superconducting mechanism was finally established by J. Bardeen, L. Cooper, and J. Schrieffer. The so called BCS theory introduced the concept of the Cooper pair, which is formed as a result of the electron-phonon interaction and leads to superconductivity.[5] When the temperature is low enough, two electrons with opposite wave vector can form a pair due to the attractive interactions between them. Once condensed, these electron pairs move in a single coherent motion

and cannot be scattered by local impurities, which means the flow is without any dissipation.[5,6]

In the same year, the classification of two types of superconductors was introduced by A. Abrikosov, based on κ which is the ratio of the penetration depth λ and the coherence length ξ.[7] Type I superconductors with $\kappa < (1/2)^{1/2}$ excludes all magnetic field until the flux penetrates the material thoroughly. The superconducting state breaks up instantly after the magnetic field reaches the critical value. While in type II superconductors with $\kappa > (1/2)^{1/2}$, there are two critical fields – lower critical field (H_{c1}) and upper critical field (H_{c2}). The magnetic field is completely expelled by a type II superconductor below H_{c1}, and fully penetrates it when higher than H_{c2}. When magnetic field is between H_{c1} and H_{c2}, a type II superconductor is in a mixed state, where the magnetic flux is partially excluded and the material still remains superconducting.[6,7] Figure 1.1 shows the two types of superconductors via the magnetization and the applied external field.

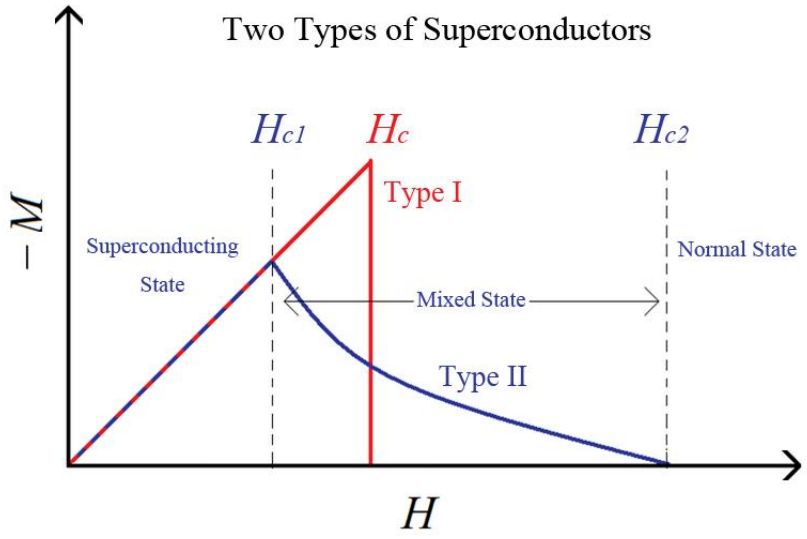

Figure 1.1 Magnetization vs. magnetic field for two types of superconductors. A mixed state is in type II superconductors when the magnetic field is between H_{c1} and H_{c2}.

In the mixed state, a lattice of quantized flux tubes, vortices, is formed when the magnetic flux penetrates type II superconductors. The core of the vortex is in normal state, surrounded by superconducting current, and the vortices are repelling one from another by Lorentz force, to form a lattice with the lowest free energy.[6] As the field increases, these vortices are driven into motion and dissipation appears.[8] Details about vortices in the mixed state of type II superconductors will be discussed in Section 1.2 and 1.4.

Superconducting tunneling effect, also known as Josephson Effect, was discovered in 1962 by B. D. Josephson, showing that Cooper pairs are able to tunnel through an insulator barrier if the barrier is thin enough. The idea of designing

superconducting junctions is then became possible and another field of application for electronic devices based on those junctions was developed.[6]

An impressive progress in the research of superconductivity was the discovery of cuprates as high temperature superconductors (HTS) in 1986. The first one was $La_{2-x}Ba_xCuO_4$ with the T_c of 30 K, found by J. G. Bednorz and K. A. Muller.[9] It was quickly followed by other cuprates with T_c higher than 77 K, which is within the reach of liquid nitrogen, such as the famous $YBa_2Cu_3O_{7-\delta}$ (YBCO)[10,11]. It was a monumental achievement since the cost of the liquid nitrogen is hundred times lower than the liquid helium. However, on the aspect of the application, there are still concerns for the cuprates such as their high production cost and strong anisotropic properties resulted from the weak inter-planar coupling.[6]

Superconductivity with $T_c \sim 40$ K was discovered in MgB_2 by J. Nagamatsu et al in 2001.[12] Its high T_c comes from the ultrahigh vibration energy in boron planes which has the similar structure as graphite. Both magnesium and boron are cheap and abundant which makes MgB_2 a potential candidate in future applications of superconductors.

In 2006, iron-based superconducting materials – a new family of superconductors – was discovered by Y. Kamihara and his colleagues, and was soon brought to attention by its lower anisotropy compared to cuprates.[13] The discovery was followed by many studies aimed at exploring new types of iron-based superconductor and trying to elucidate the superconducting pairing mechanisms in these systems.[14-16] This kind of materials consists of FeX layers, in which X is either pnictogen atom (As) or chalcogen

atom (Se, Te), in the unit cells along the *c*-axis. Iron-based pnictides and chalcogenides have defied the assumption that the large magnetic moment of iron would break the Cooper pairs and suppress the superconductivity. Currently the T_c for iron-based superconductors can reach over 100 K in iron selenium single layers.[17] High upper critical field is also one of the outstanding advantages of this kind of material. With the combination of high H_{c2} and low anisotropy, this class of superconductors is becoming a new potential candidate for high-field applications at the liquid helium temperature.[18]

For the application of superconductors, there are three major parameters reflecting the practical superconducting properties: critical temperature T_c, critical current density J_c and upper critical field H_{c2}. Figure 1.2, shows the superconducting properties, T_c, J_c and H_{c2} for several materials.[19] Details about how to enhance these parameters, mainly for J_c, in certain materials will be discussed in this dissertation.

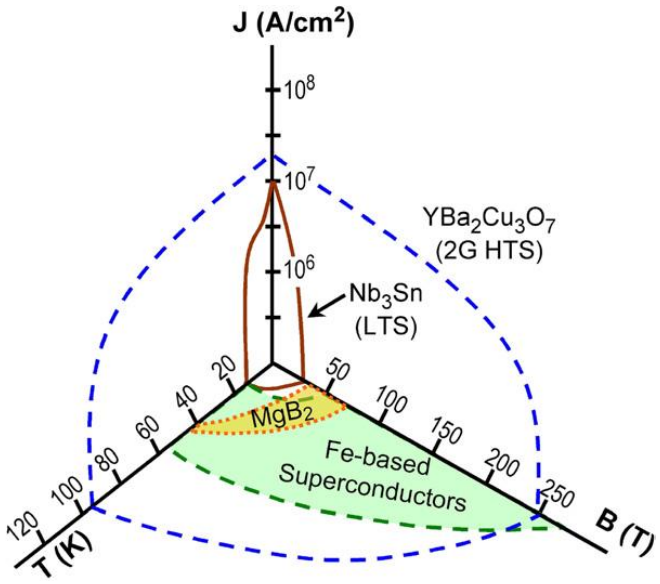

Figure 1.2 Electrical current density-temperature-magnetic field plot of several superconducting materials, adopted from Ref. 19.

1.2 Vortex and flux pinning in superconductors

Vortex pining is one of the most important issues on the aspect of the large scale application of superconducting materials. Due to the limit of the critical field and current density, type I superconductors can hardly be used for energy transport or storage. Currently, all large scale practical superconducting materials are type II with certain amount of defects as pinning centers.

As mentioned in the previous section, a type II superconductor shows complete diamagnetic behavior when the field is below H_{c1} – the expulsion of external magnetic field is complete and so that the B inside the superconductor is zero. When the field is between H_{c1} and H_{c2}, it is in a mixed state. For an ideal type II superconductor in the mixed state, magnetic flux partially penetrates the material and forms vortices, with the

core size of the coherent length ξ. The center of the vortex is in normal state with maximum magnetic flux density, surrounded by a supercurrent. The magnetic field decays from the center of the vortex and extends into the nearby regions at the depth of λ, which is the penetration depth. In this state the bulk still shows superconductivity. Magnetic flux in each quantized vortex is $\Phi_0 = h/2e = 2.07 \times 10^{-15}$ Tm^2. The periodic magnetic flux density in an ideal type II superconductor is shown in Figure 1.3.[20] At the core of the vortex, the order parameter $|\psi(r)|^2$ is minimized, where the magnetic flux density B reaches the maximum value.

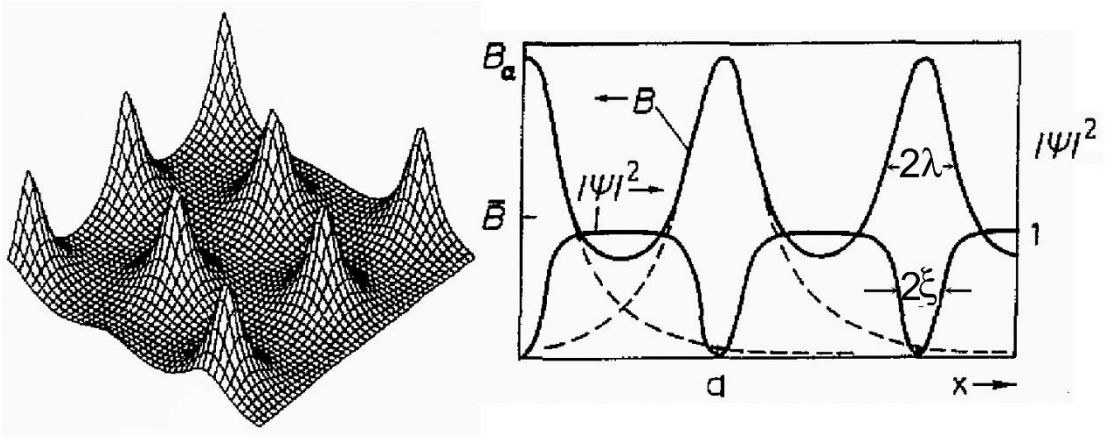

Figure 1.3 The periodic magnetic flux density B(x,y) on the surface of a type II superconductor (left panel), and the B and order parameter $|\psi(r)|^2$ profiles along an array of vortices (right panel). The figure is adopted from Ref. 20.

Under a fixed external magnetic field, an important factor which can affect the stability of the vortex matrix is the electrical current. With a large current applied, vortices are driven in motion, which is called flux flow, due to the Lorenz force. Moving vortices create a local change of magnetic flux and an electric field. With both

the electric field and the current, dissipation appears and leads to a non-zero resistivity. For an ideal type II superconductor in the mixed state, a small applied current is enough to create dissipation as there is nothing to prevent the motion of the vortices. Even without the external field, the current itself can also drive the vortices in motion. As long as the field generated by the current, or so called self-field, exceeding H_{c1} which brings the superconductor in to the mixed state, it can move the vortices and cause dissipation. The magnitude of this current could be estimated as $J \sim H_{c1}/d$, where d is the dimension of the material. The schematic of the vortex matrix and a single vortex in the mixed state with the Lorenz force induced by the applied current is shown in Fig. 1.4.[6]

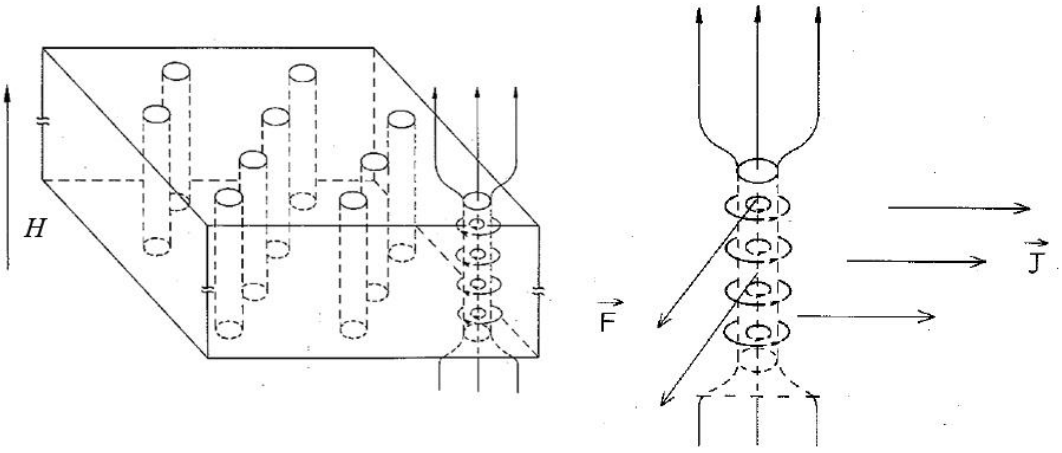

Figure 1.4 Schematic of the vortex matrix in the mixed state for an ideal type II superconductor (left panel) and an enlarged view of a single vortex under the Lorenz force induced by the current applied perpendicular to the field direction (right panel). The figure is adopted from Ref. 6.

However, certain impurities or structural defects can result in a non-uniform vortex distribution by having it pinned and support the bulk supercurrent, and the material remains to be superconducting. Note that the formation of magnetic flux in type II superconductors is the result of keeping the system in the lowest energy. The normal-superconducting interface energy is negative when $\kappa > (1/2)^{1/2}$,[6] where the energy cost for the formation of a normal state vortex core in the superconducting bulk is smaller than the energy cost for expelling the magnetic flux. This energy cost can be further reduced if the core stays in a non-superconducting or weak-superconducting region which already exists in the material caused by impurities or defects. Such a region can act as an energy trap, from which moving the vortex costs additional energy. This is the mechanism how vortices can be pinned by defects. The average force per unit volume preventing the motion of the vortices is defined as the vortex pining force $F_p = J \cdot B$.

As the applied current increasing, vortices in the material form a critical state where a balance of the maximum vortex pining force and Lorenz force induced by current is achieved. For type II superconductors, critical current density J_c is determined by the largest current density applied to the material which can still maintain the zero resistance. Upon this critical point, further increase of current will break the balance and drive vortices in motion which leads to the appearance of resistivity. Note that J_c is a magnetic field dependent value which normally decreases with the rising field. At a fixed temperature, the largest J_c can be obtained at $B = 0$ which is called self-field J_c. The J_c represents the pinning strength of the vortices by

defects in the superconductor. Thus the defects in type II superconductors are crucial for practical applications.

J_c usually marks the starting point of the flux flow which means as long as the applied current density is smaller than J_c, the vortex would supposed to be firmly pinned by F_p. However, thermal fluctuations will cause the flux lines to move when the current density is close to J_c, which will start to show a non-ohmic resistivity. This phenomenon is called flux creep.

As described above, defects and impurities can act as pining centers to enhance the pining force in type II superconductors, and thus enhancing J_c. With this understanding, people started to investigate the possibilities of artificially inducing defects into superconducting materials in order to have the J_c improved. Details will be discussed later in the chapter (Section 1.4), after introducing the superconducting materials studied in this thesis.

1.3 Superconducting materials studied in this dissertation

This dissertation focuses on transport studies in two kinds of superconducting materials: $FeSe_{0.5}T_{0.5}$ (FST) thin films and the second generation (2G) YBCO coated conductors. They are introduced below separately.

1.3.1 YBCO coated conductors

Exploring the commercial use of superconducting wires was carried out soon after the discovery of HTS in 1986. If successfully produced, a variety of power devices

including transmission cables, transformers, fault current controllers, motors and generators can be constructed using these superconducting wires.[21,22] The most commonly used materials in early HTS wires were bismuth-based, specifically $Bi_2Sr_2CaCu_2O_x$ (Bi-2212) and $Bi_2Sr_2Ca2Cu_3O_x$ (Bi-2223). These materials were made into multi-filament wires using silver tubes, known as the first generation (1G) HTS wire. These 1G wires have been commercially available since 1990, typically holding a J_c around 10^5 A/cm^2 at 77 K. Although 1G HTS wire can be operated at a high temperature up to 108 K (Bi-2223), which dramatically addressed the problem of costly cryogenics, the heavy reliance on silver as a raw material made the wire far too expensive to practically used in power devices.

Another HTS material YBCO has also been developed since its discovery. Unlike the synthesis method used in 1G wire, which is powder sintering in tubes, the development of YBCO wire was focused in the form of thin film.

Though having a lower T_c (92 K) compared to that of Bi-2223, YBCO shows very good performance on the aspect of J_c. In the form of thin film grown on lattice matched single crystal substrates, YBCO possess a self-field J_c above 1 MA/cm^2 at 77 K which is an order of magnitude higher than that of 1G wires.[23,24] However, problems came when considering the practical production of long tapes: films grown on metal substrates show poor superconducting properties. Though it was found that comparatively higher quality YBCO films can be grown with the help of a *c*-axis oriented yttria-stabilized zirconia (YSZ) as the intermediate layer on a metal substrate,

the J_c is still two orders of magnitude lower than those grown on single crystal substrate like $SrTiO_3$ or MgO [25,26].

This problem was then solved thanks to the technique of ion-beam-assisted deposition (IBAD). It can produce bi-axially aligned YSZ thin films on long metal tapes as a buffer layer, with the grain misorientation controlled below 5°.[27,28] With the well aligned and lattice matched buffer layer, high quality YBCO films can be grown on metal substrate, showing J_c above 1 MA/cm^2 at 77 K. Using IBAD technique, other buffer layers such as MgO and CeO_2 were also developed for further improving superconducting properties of YBCO tapes[29,30].

The superconducting thin films, typically YBCO films, grown on textured buffer layers on metal substrates are known as 2G coated conductors, or the 2G HTS, since 1997. It has been commercially produced by Superpower, as shown in the upper panel of Fig. 1.5. Another approach, using the rolling assisted biaxially textured substrate (RABiTS), was later developed to produce 2G coated conductors[30]. Epitaxial buffer layers are deposited on textured Ni-W substrate, supporting the growth of high quality YBCO layer. This RABiTS approach is used by American Superconductor to produce 2G coated conductors, as the schematic shown in the lower panel of Fig. 1.5.

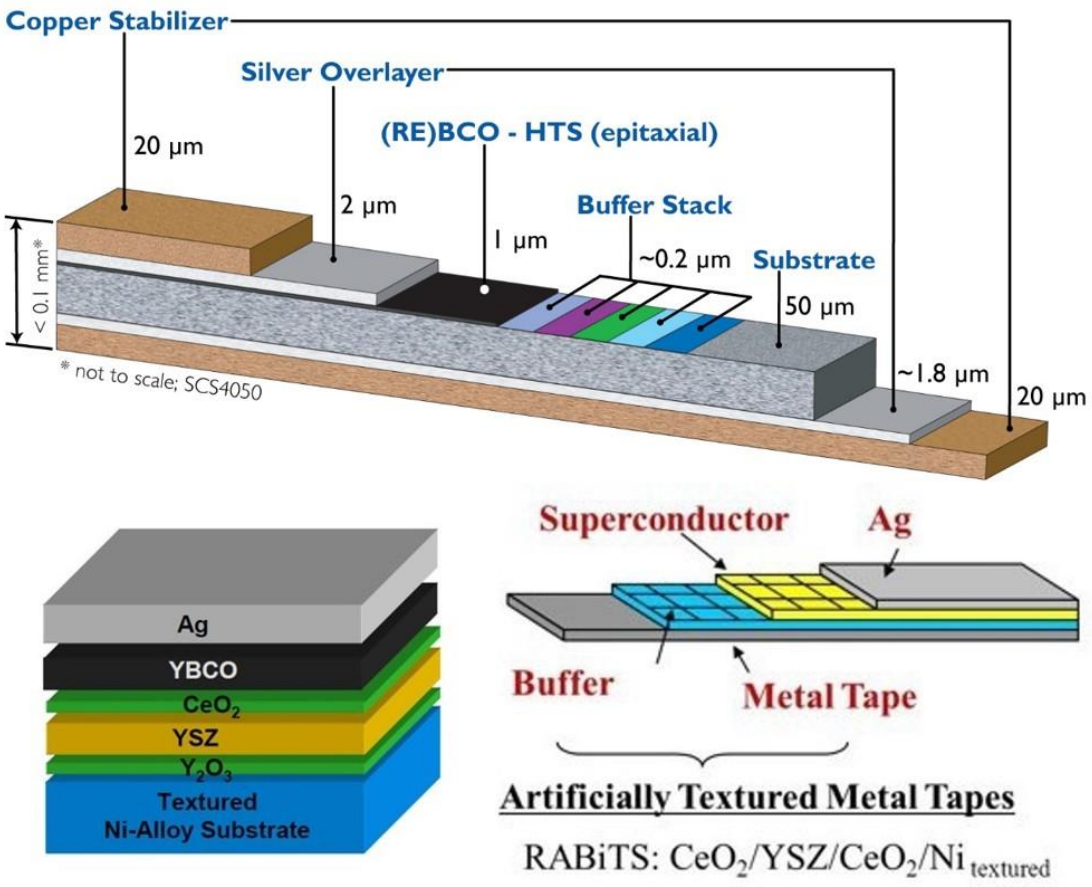

Figure 1.5 Configuration of 2G HTS coated conductors using IBAD (upper) and RABiTS (lower) techniques, adopted from webpage.[31]

In typical 2G HTS tapes with ~1 μm thick YBCO as the superconducting layer, the current carrying capability is over 500 A/cm-w at 77 K and 1000 A/cm-w at 30 K[32-34]. In addition to better performance under high magnetic field compared to 1G wire, 2G HTS wire also have other advantages such as lower cost. Long tapes can be effectively produced via reel-to-reel process, with ~97% of inexpensive Ni alloy and Cu as the base material[31,35-37]. It is promising to be practically used in transmission cable, transformers, fault current controllers, motors and generators.

1.3.2 Iron-chalcogenides

Iron-based superconductors was first discovered in 2006 by Y. Kamihara in the study of LaOFeP.[13].In 2008 another material $LaFeAsO_{1-x}F_x$ (x = 0.05 -0.12) joined the family with a T_c ~ 26 K, discovered by the same group.[14] Iron-based superconductors were soon becoming a hot topic and many studies have been performed accordingly.

These materials have FeX layers, where X represents pnictogen atom or chalcogen atom, along the *c*-axis in the unit cell and are currently categorized into four types in terms of the different stoichiometry, as shown in Figure 1.6[15].

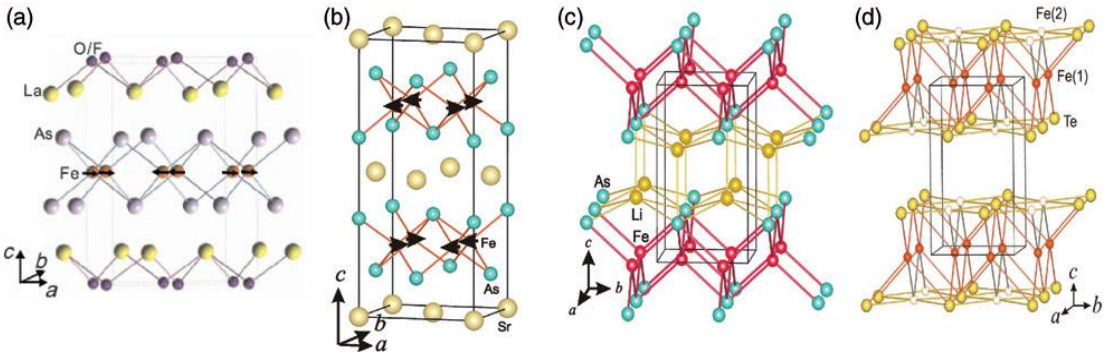

Figure 1.6 Crystal structure of four types of iron-based superconductors: (a) '1111' type, (b) '122' type, (c) '111' type and (d) '11' type, categorized by different stoichiometry The figure is adopted from Ref. 15

Among these four types of iron-based superconductor, the class of '11' type iron chalcogenides is the least toxic system and possesses the simplest structure. It was first discovered by F. Hsu *et al* in July 2008 in the form of FeSe with T_c = 8 K.[38] Thanked to the binary system which makes the studies on doping effect easier, it was not long before $FeSe_xTe_{1-x}$ was found with an enhanced T_c at 14 K with x = 0.5.[39] A phase

diagram of $FeSe_xTe_{1-x}$ was mapped by T. Liu et al[40], as shown in Fig. 1.7, where SC stands for superconductivity and AFM stands for anti-ferromagnetism. Focusing on the superconductivity part, it is seen that electrical zero-resistance starts to show at very low Se concentration, labelled as open diamonds, while pure FeTe is not superconducting. These filamentary superconductivity turns into bulk superconductivity at $x \sim 0.3$, confirmed by magnetization measurement.

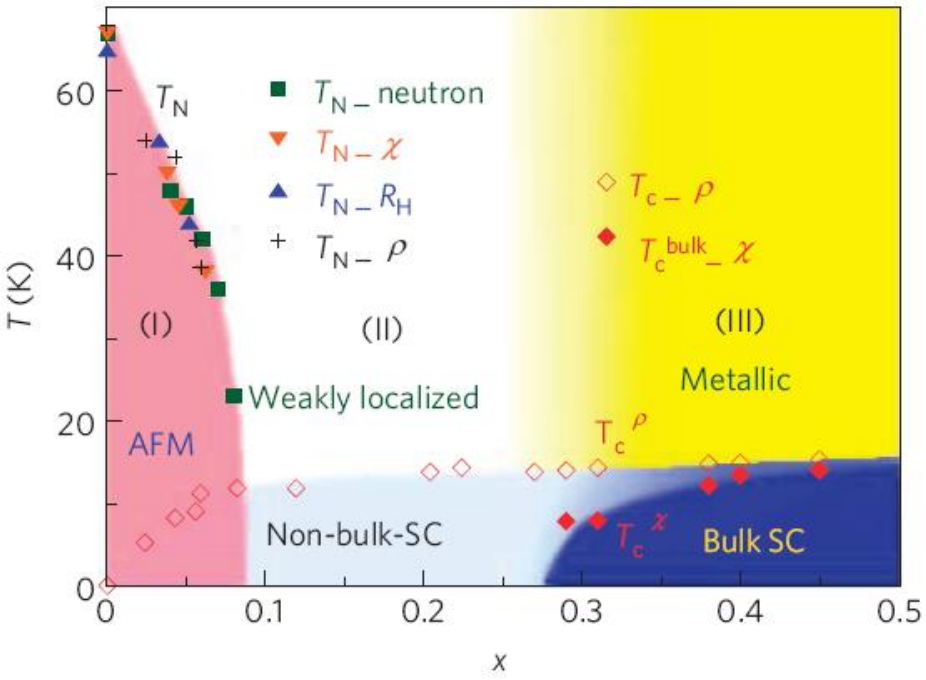

Figure 1.7 Phase diagram of $FeSe_xTe_{1-x}$ ($0 \leq x \leq 0.5$), adopted from Ref 40. Bulk superconductivity shows at $x \sim 0.3$, and the highest T_c occurs at $x = 0.5$

Studies in $FeSe_xTe_{1-x}$ were continued on the aspect of superconducting property enhancement. High T_c of 37 K was found in FeSe under 7 GPa pressure, reported by S. Margadonna *et al* in 2009.[41] The highest T_c over 100 K was found in FeSe monolayer.[17] However, these high T_cs achieved under pressure or in monolayer can hardly be applied

in practical condition. On the other hand, thin film fabrication of $FeSe_xTe_{1-x}$ has also made progress, with T_c and J_c enhanced compared to bulk. A series of studies on FST thin film synthesis was performed by E. Bellingeri *et al*, showing relation between T_c and compressive strain.[42-45] Thin films in their studies were grown on different substrates by pulsed laser deposition, with the highest T_c above 21 K. However, another crucial superconducting property J_c in those films were merely above 10^5 A/cm^2 (self-field) at 4.2 K, far lower than that of '122' thin film which is above 4 MA/cm^2.

The previous study performed by W. Si has shown the enhancement of both T_c and J_c in FST thin films by introducing a CeO_2 buffer layer.[18] The film and the buffer layer were epitaxially grown on single crystal substrate, exhibiting a T_c of 18 K and a J_c of 1 MA/cm^2. Note that with the CeO_2 buffer layer, J_c in FST material was first enhanced up to the level of 1 MA/cm^2, which is qualitatively comparable to that of '122' thin films. These films exhibited excellent in-field performance confirmed by the transport measurement conducted under high magnetic field carrying a $J_c \sim 10^5$ A/cm^2 at 4.2 K under 30 T.

1.4 Correlation between the structure and superconducting properties

1.4.1 Defects and vortex pinning

Defects in the material such as dislocations, stacking fault or grain boundaries may act as pinning centers for the vortices. As mentioned in Section 1.2, the center of the vortex is in normal state surrounded by supercurrent.

In order to effectively pin the vortex, the size of the defect or impurity should be similar to the size of the vortex core, which is the coherent length ξ determined by temperature. If the defect is too large or too small compare to the vortex core, the energy cost for the vortex formation, the form of normal-superconducting interface, would be increased. It reduces the stability of the vortex matrix so that the current can drive the vortex easier, results in a lower J_c. For conventional superconductors, the size of vortex core is usually on the order of hundreds nanometer. Thus extended defects such as grain boundaries or stacking fault would be ideal pining site for these materials. For cuprates and iron-based superconductors, the coherence length is a few nanometers which corresponds to point defects or small linear dislocations. For example, $\xi \sim 2$ nm in YBCO ab plane, so that the pinning for the rigid magnetic flux will be less effective by introducing large defects[64,68,69]. However, at the temperature near T_c, larger defects are needed to pin the vortex since the vortex lines are soft.

Introducing defects strengthens the vortex pining, but on the other hand, it also alters the local crystal structure and weakens the Cooper pairs, which may at some point severely destroy the superconductivity intrinsically. To find a balance between these two mechanisms is crucial on the aspect of application of the superconducting materials.

1.4.2 Introducing defects by ion irradiation

Tremendous efforts have been made to optimize the size and density of defects in order to effectively enhancing J_c, for both HTS and iron-based superconductor.[46-50] Among various methods, ion irradiation was found to be effective and has been

developed.[49,51-55] The main advantage of ion irradiation is that the created defects can be rather easily controlled on the aspect of density and morphology, by selecting appropriate ion source, accelerating energy and dosage. It can provide comparatively predictable results without altering the growth condition of the material.

In the process of irradiation, the ions are accelerated to a high energy and bombard the target material. Two major events happen during the irradiation process: ionization and recoil. Ionization is the interaction between the incident ions and the electrons in targeting material, and recoil is nucleus-ion collisions. Ionization generates a large amount of heat, which could melt the adjunct area along the way where the incident ion goes through. Too much impact on local crystal structure could severely suppress superconductivity, therefore thought to be a side effect. Recoil, as another event in irradiation, is considered to bring in effective pining centers to enhance J_c: the collisions between nucleus and incident ions create displacements on atomic level, forming dislocations. The density of these defects is also controllable by tuning the dosage of the irradiating beam.

In early years, HTS ion irradiation was conducted at high energy, with the level from hundred MeV to GeV.[49,53,54,56-59] Large columnar defects were found in irradiated materials. Though the enhancement of J_c is observed, there are always very large T_c degradations accompanied. High level of ionization and accompanied heating effect cannot be avoided in these high energy irradiation.

Transmission electron microscopy (TEM) cross-sectional images along the ion traces in 230 MeV Au-irradiated Bi-2212 single crystals showed several types of

morphology of defects in the HTS irradiated by ions with different energies, from parallel columnar defects to disordered cascade defects[60,61] The experiment indicated the possibility of inducing different types of defects by tuning the ion energy..

There are several positive aspects of low energy irradiation, besides the reduced cost and complexity of the system. The collision cross-section of an ion changes as $\sim 1/E^2$, thus less dosage is needed in order to generate the required defect density. The beam heating is reduced proportional to the product of the energy and dosage, therefore low energy irradiation significantly reduces need of cooling. Recent studies on low-energy ion irradiations suggests that it has great potential as a practically feasible approach to improve flux pinning in YBCO.[52,62,63]

Due to the damage caused by irradiation, T_c is always found much degraded in YBCO after irradiation regardless the ion energy and type. Post-oxygen annealing has been reported as an effective method to rearrange the structure and thus modify the influence of the defects in YBCO caused by ion irradiation.[58-60] It is seen as a structural reconstruction process which modifies the density the defect induced by ions. However, it is also possible that the enhanced pinning in YBCO by the defects may be reduced during the annealing.

Ion irradiation has also been applied to iron-based superconductors. In single crystal iron-based superconductors, it has been found that ion irradiation, as a whole, has the improving effect on J_c. The J_c enhancements persist higher fluencies than in cuprate superconductors, although T_c was suppressed with increasing irradiation

doses.[64-68] However, the irradiated iron-based superconducting films have not shown the positive effect as found in single crystals yet.[69,70]

1.4.3 Ferromagnetic impurities in iron-based superconductors

Superconducting materials can achieve higher J_c from stronger vortex pinning by inducing defects. However, certain defects may not be helpful since they will severely suppress the superconductivity, such as ferromagnetic impurities.

It is not hard to understand the conflict between superconductivity and ferromagnetism. According to Meissner effect, materials in superconducting state show diamagnetism which expels any applied magnetic field; whereas, a ferromagnet concentrates the magnetic force lines of the field inside its volume, which is known as the effect of magnetic induction. In 1957, Ginzburg explained the antagonistic phenomena between superconductivity and ferromagnetism based on this conception, that the magnetic induction exceeds the critical field.[71] This competing phenomenon is also understandable on the aspect of microscopic theory. In BCS theory, electrons can combine to form Cooper pairs through electron-phonon interaction at sufficient low temperature. The pairing requires the electrons having the opposite spin direction. Within this frame, the formation of Cooper pairs will be severely affected by ferromagnetism, where electron dipoles tend to align in one direction spontaneously.

Though some researches have been carried finding the coexistence of superconductivity and weak ferromagnetism[72-75], the general view of the antagonistism hasn't been changed[76-80].

When a ferromagnet acts as an impurity in a superconductor, it affects nearby regions due to the magnetic induction. The suppression of the superconductivity resulted from ferromagnetic impurities has been found in various superconducting materials.[80-84] This issue is more obvious in "11" system of iron-based superconductors. Though most of the Fe atoms are combined with chalcogenide atoms in the compound and lost the ferromagnetism, there are still interstitial Fe atoms inevitably left alone during the synthesis. In 2009, several reports have shown the suppression of superconductivity in $FeSe_xTe_{1-x}$ due to the excess Fe.[85-87] T. McQueen reports that even 3% extra Fe can totally eliminate the superconductivity in FeSe, which normally has a T_c of 8 K.[86]

A series of studies were performed in order to reduce the excess Fe, including the treatment through moisture, acid, even alcohol beverages[88-96]. It has been proved that superconductivity in $FeSe_xTe_{1-x}$ bulk materials can be improved with the removal of the interstitial Fe. Among these methods, oxygen annealing appeared to be the most effective and controllable way to achieve better superconducting performance[89,91,93-95]. However, for the thin film type of material, there is no report yet mentioned about the annealing effect on transport properties in $FeSe_xTe_{1-x}$. Given that FST thin films have intrinsically higher T_c and J_c compared to bulk, it would be of much value to conduct a systematically study to investigate the change of the transport properties influenced by oxygen annealing.

1.5 Motivation of the study

Fossil fuel has been the main source of energy for human being over hundreds of years and cannot be fully replaced in near future. It is not renewable and the price is rising up rapidly as a result of depletion. Thus, people are trying to find more efficient ways for the storage and transportation of energy. Superconducting materials have been considered for this purpose ever since they were discovered, due to their ability to carry electrical current without dissipation.

The discovery of HTS in the 80's initially offered the hope of engineering materials for long-distance energy relocation by means of bringing the T_c above the liquid nitrogen temperature. Years later, 2G coated conductors were developed and the synthesis conditions have been optimized. One of the current task is to explore the post-treatment techniques to further enhance their superconducting properties. In this dissertation, gold ion irradiation and accompanied oxygen post-annealing are conducted on 2G YBCO coated conductors, in order to enhance high field J_c performance. With the intrinsic high T_c above 90 K, once higher in-field J_c is achieved, this material would become more promising for further applications on energy transport and storage.

Though currently dominating the T_c and J_c among all superconductors, 2G coated conductors are still far from being perfect, due to its large field anisotropy, low tolerance to grain boundary angles and, most importantly, the high manufacturing cost.[97,98] Iron-based superconductors, such as FST, are becoming potential candidates for the future applied superconductors especially for high field application. High upper

critical field, low anisotropy and simple structure make them very competitive at liquid helium temperature. By utilizing thin film fabrication techniques, the superconducting properties are much enhanced compared to bulk. In this dissertation, results of detailed transport measurement for FST films grown on single crystal substrate with CeO_2 buffer layer are shown. More importantly, their superconducting properties can be further improved by two cost-efficient post-treatment techniques – low temperature oxygen annealing and proton irradiation.

2. Experiments

In this dissertation, experiments and transport studies were performed on two kinds of superconducting materials:

1) FST thin films – synthesized by pulsed laser deposition (PLD) with the details described in Section 2.1.2.

2) YBCO coated conductors – provided by collaborators.

2.1 Thin film growth and patterning

2.1.1 Introduction of PLD technique

In the past decades, PLD has gained lots of attention since it is a simple and effective method to deposit materials of complex stoichiometry. It has been playing an important role in the superconductivity research since successfully fabricated YBCO thin film in 1987.[99]

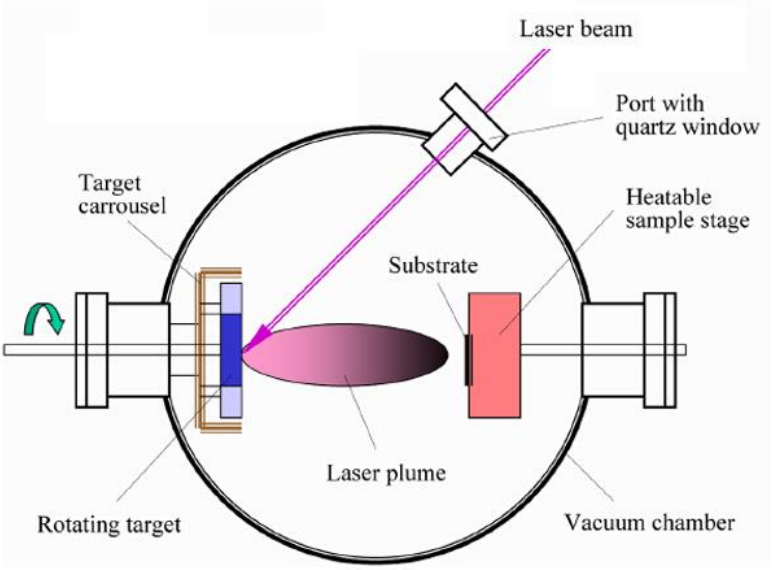

Figure 2.1 A schematic of PLD system, adopted from Ref. 100. The target material becomes plume after hit by pulsed laser and is deposited on the substrate.

As shown in Fig. 2.1[100], the rotating target material is ablated by high energy laser beam and becomes plasma in gas phase. Under certain temperature and pressure, it is then deposited on the surface of the substrate to form thin films. The experiments conducted in this dissertation was using KrF excimer laser to hit the FST and CeO_2 target.

PLD creates an ejected plume of the target material. The actual physical processes of material removal are complicated; one can consider that the ejection of material occurs due to rapid explosion of the target surface by superheating. PLD is considered to produce a plume of material with the same stoichiometry as the target material, thanks to the laser-induced expulsion. This is the main advantage for PLD compared with other deposition technologies, such as thermal evaporation which produces a

vapor with the composition depending on vapor pressures of the elements in the target material. It is therefore widely used to synthesize materials with complex composition especially for oxides. It is easy for PLD to make multi-layer thin films by change the target material. Besides, PLD is also considered to be a fast processing method, by which high quality thin films (50~100 nm thick) can be grown reliably in 10 or 15 minutes.

During growth, several parameters need to be optimized. The quality of the film is easily affected by the fluctuation of pressure or temperature. Therefore, the vacuum system and heating system are crucial, sometimes even more important than laser itself. The density of the plasma is an important factor which mainly depends on the pressure in the chamber and the energy density of the laser. Besides, the distance between the target material and the substrate will also affect the film quality. The optimum growth parameters varies a lot between different target materials. For example, oxides films are usually grown well in oxygen environment with certain pressure which avoids the loss of oxygen during growth. In addition to the growth environment, the selection of proper lattice-matched substrate is also important.

2.1.2 Synthesis of FST thin films with CeO_2 buffer layer

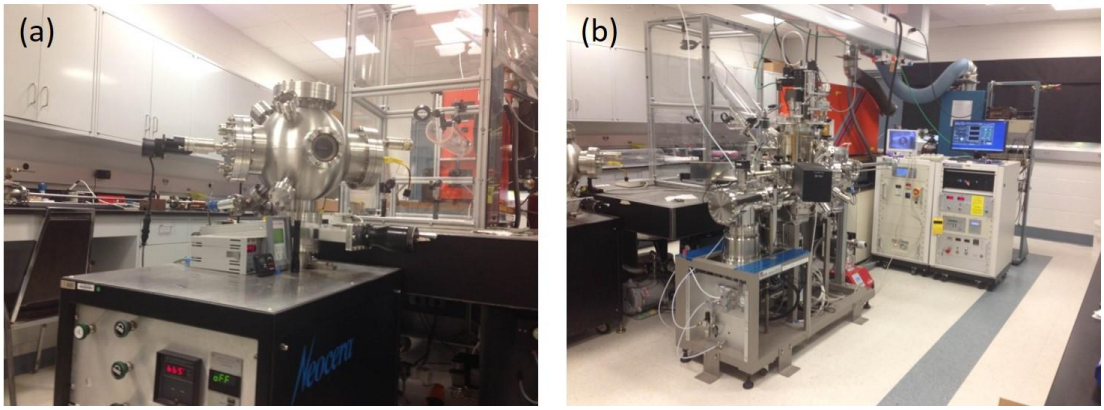

Figure 2.2 Two PLD systems used for $FeSe_{0.5}Te_{0.5}$ thin film synthesis.

Figure 2.2 shows the PLD systems for FST film growth. The rectangular box in orange is the KrF excimer laser system. Carefully tuned with a series of lenses, the laser beam at a proper spot size can be lead into the chambers where the films are synthesized.

Before February 2014, the FST films were synthesized using the chamber shown in Fig. 2.2a. It is a simple yet effective thin film growth chamber with the thermal irradiating heater on the back of the sample stage. The heating power is controlled by the electrical current applied on the heater. A thermocouple is soldered on the sample stage to read the temperature. The vacuum of the chamber can be well controlled on the level of 10^{-6} Torr with the turbo pump at elevated temperature. Up to six targets can be mounted on the target holder at the same time and can be toggled without opening the chamber. There is a shield mask on the target holder, exposing only one target and shielding other five to avoid inter-contamination. During the deposition, the target keeps rotating at the speed ~ 60°/s, controlled by a motor. Oxygen or nitrogen gas can

be introduced into the chamber to alter the growing environment depending on different materials. However, this old system is not able to reach ultra-high vacuum.

The larger one shown in the right photo in Fig. 2.2b is a more advanced deposition system purchased from Pascal Corp. Films synthesized since February 2014 were grown using this system. The chamber enables ultra-high vacuum growing environment of 10^{-9} Torr. The heating system is using laser as the source. The digital feedback loop can precisely control the temperature of the substrate with the variation below 1 °C. The target holder with a digital controlled shielding mask enables toggling up to six different targets during growth. The target can keep rotating and swinging with a controlled speed to realize the uniform laser excitation on the surface. Also, an attached load lock chamber protects high vacuum environment when transferring samples or targets. With the ultra-high vacuum and precisely controlled temperature, the quality of the films becomes more uniform.

In this dissertation, FST films were synthesized with CeO_2 buffer layers. The buffer layer is deposited on the substrate prior to the growth of FST, as shown in Fig. 2.3. The purpose of introducing this buffer layer is to enhance the superconducting properties of the FST films, as was previously reported by our group.[18] For a systematic transport study, the comparison of the transport properties between FST films with and without the buffer layer will be presented later in Chapter 3.

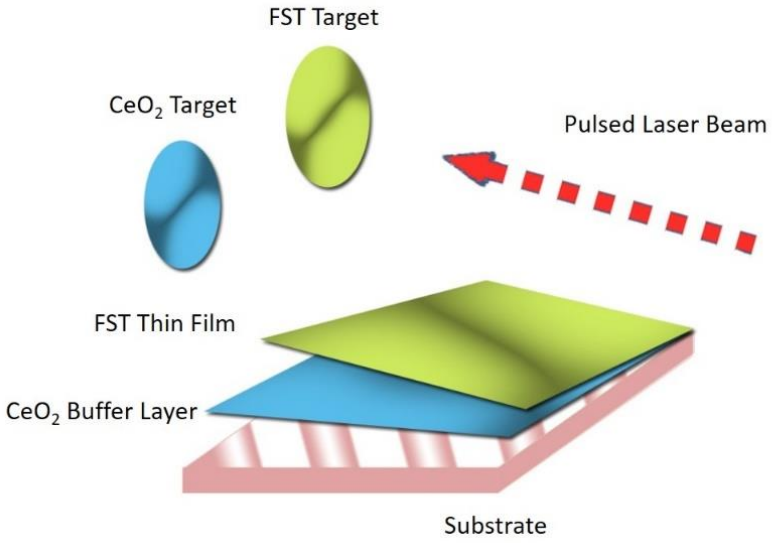

Figure 2.3 Schematic of a PLD grown $FeSe_{0.5}Te_{0.5}$ thin film with CeO_2 buffer layer between the film and the single crystal substrate.

Details of the sample preparation and growth parameters is described as below. Single crystal substrates were cut into 5 × 3 mm^2 rectangular pieces and put in the deposition chamber. A CeO_2 buffer layer was first deposited on the substrate at 600 °C, under 100 mTorr oxygen environment. FST was then deposited on the buffer layer at 300 °C under high vacuum. Energy density of the laser was set around 3 J/cm^2 during the deposition for both CeO_2 buffer layer and the FST film. After the deposition, films were cooled in vacuum in a relatively fast speed, by separating the sample holder from the heater immediately. The single crystal substrates used in FST film growth are (001) plane oriented $SrTiO_3$ (STO), $LaAlO_3$ (LAO) and Yttria-stabilized zirconia (YSZ).

2.1.3 Laser patterning

For FST thin film sample, a micro-bridge was patterned before measuring the J_c. Without the micro-bridge, it is impossible to complete the transport J_c measurement with the limited applicable current of the equipment, due to the high J_c in FST films. Besides, the micro-bridge can also enhance the measurement accuracy by regulating dimensions of the conducting area. Fig. 2.4a shows the laser patterning system which was used to make the micro-bridge. Pulsed laser beam with the energy of 3 mJ/pulse and the frequency of ~8 Hz was applied on the film surface, leaving a burnt insulation area to form the pattern. Laser spot size can be tuned by a rectangular aperture during patterning, typically set to 20 μm × 100 μm for the FST micro-bridge. These micro-bridges are usually 300 ~ 400 μm long and 10 ~ 30 μm wide. Critical current I_c can be obtained through measuring VI characteristic curve and the critical current density can be calculated by $J_c = I_c/wt$, where w is the bridge width and t is the film thickness. Fig 2.4b is a microscopic photo for a typical configuration for four-probe resistivity measurement. The bridge area is enlarged in Fig 2.4c for a clear view.

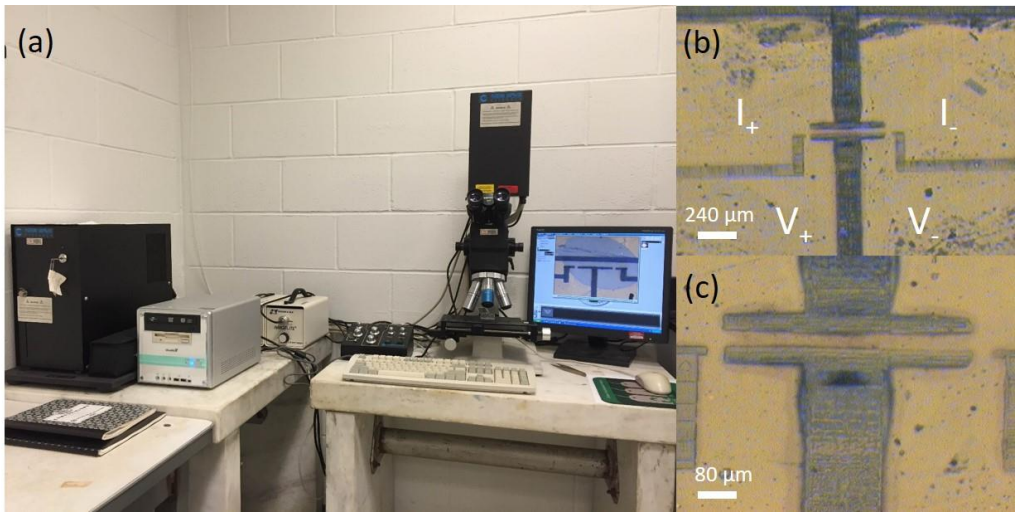

Figure 2.4 Laser patterning system (a) and a typical micro-bridge patterned on a $FeSe_{0.5}Te_{0.5}$ film (b,c). Current and voltage sections in (b) are for the standard four probe measurement.

2.2 Ion irradiation

As was introduced in Chapter 1, low energy ion irradiation is found to be an effective method to enhance J_c. In this dissertation, the effect of 22 MeV gold ion irradiation in YBCO tapes and 190 KeV proton irradiation in FST thin films have been carefully studied.

2.2.1 Gold ion irradiation in YBCO coated conductors

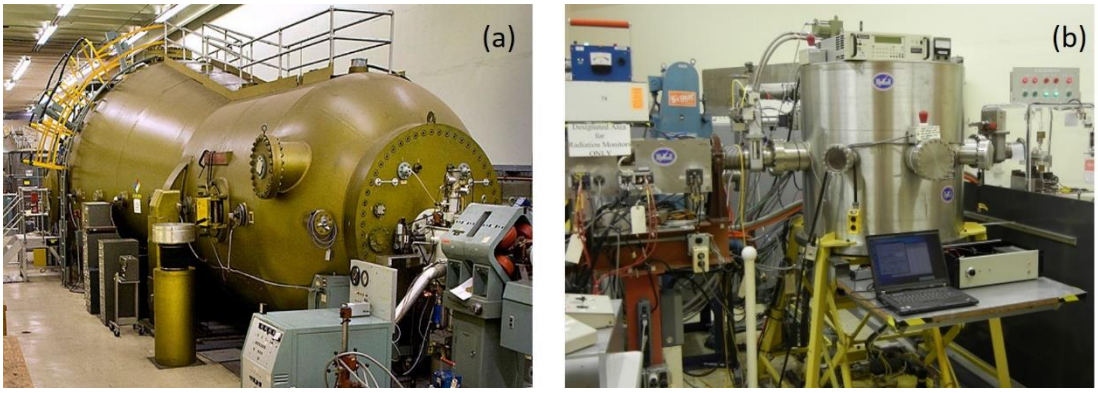

Figure 2.5 Tandem Van de Graaf accelerator (a) and the vacuum chamber (b) used in gold ion irradiation experiment.

Gold ion irradiation experiment was performed using the Tandem Van de Graaf accelerator at BNL (Fig 2.5a). Samples were 2G coated conductor tapes, obtained from an industrial collaborator. They were synthesized by depositing a 1.5 μm thick YBCO layer on RABiTS by reel-to-reel process. Before irradiation, tapes were coated with 1 μm thick silver layer by magnetron sputtering and annealed in flowing oxygen at 400 °C for 1 hour. They were then cut into 3×3 mm^2 squares and mounted on the sample board by silver paint (Fig. 2.6). Each round area on the sample board was prepared for being irradiated at different dosages.

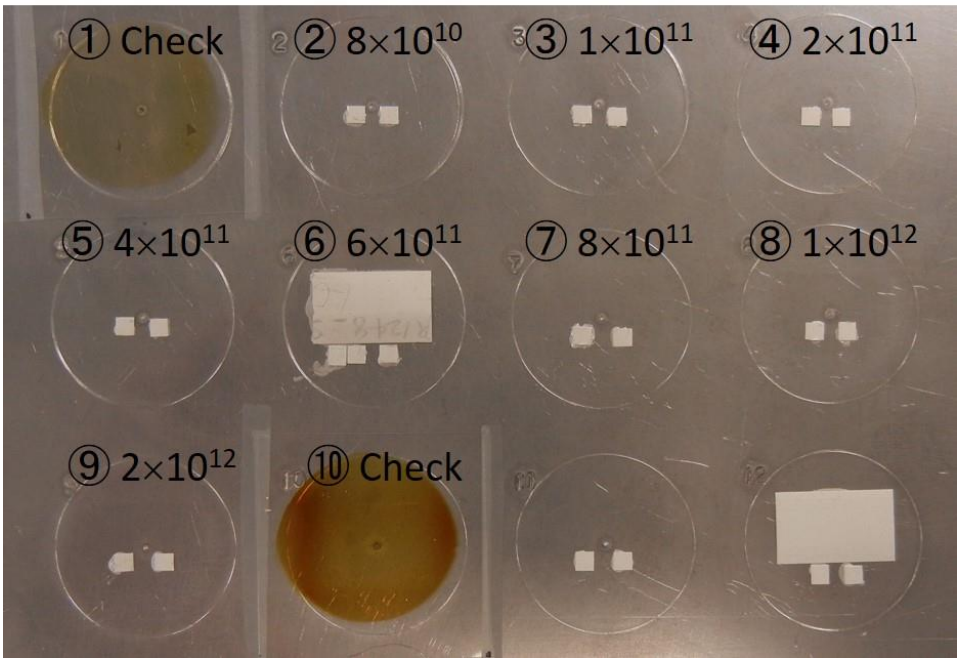

Figure 2.6 $YBa_2Cu_3O_{7-\delta}$ tapes mounted on the sample board, irradiated at different dosages. Colored circles are irradiated indicating films to check the alignment and uniformity of the ion beam.

The sample board was put into a chamber which was then pumped to a vacuum of 10^{-5} Torr (Fig. 2.5b). Au^{5+} ions were accelerated in the tandem to 22 MeV before bombarding the samples. Ion beam was first calibrated by hitting a transparent indicating film to align the beam position as well as to check the beam uniformity. The colored region on the top left in Fig 2.6 shows the ion beam influence profile. The beam was then hit on each circle on the sample board with 8 different dosages: 8×10^{10} cm^{-2}, 1×10^{11} cm^{-2}, 2×10^{11} cm^{-2}, 4×10^{11} cm^{-2}, 6×10^{11} cm^{-2}, 8×10^{11} cm^{-2}, 1×10^{12} cm^{-2} and 2×10^{12} cm^{-2}. After samples were irradiated, the ion beam was check again to hit the indicating film as shown in circle number 10. Magnetization measurement was performed to characterize the T_c and J_c in the irradiated samples. The reference T_c and

J_c data was averaged from three unirradiated samples and was used to analyze the change before and after the irradiation.

The irradiation condition was simulated by using Stopping and Range of Ions in Matter (SRIM) code[101]. The result is shown in Fig. 2.7.

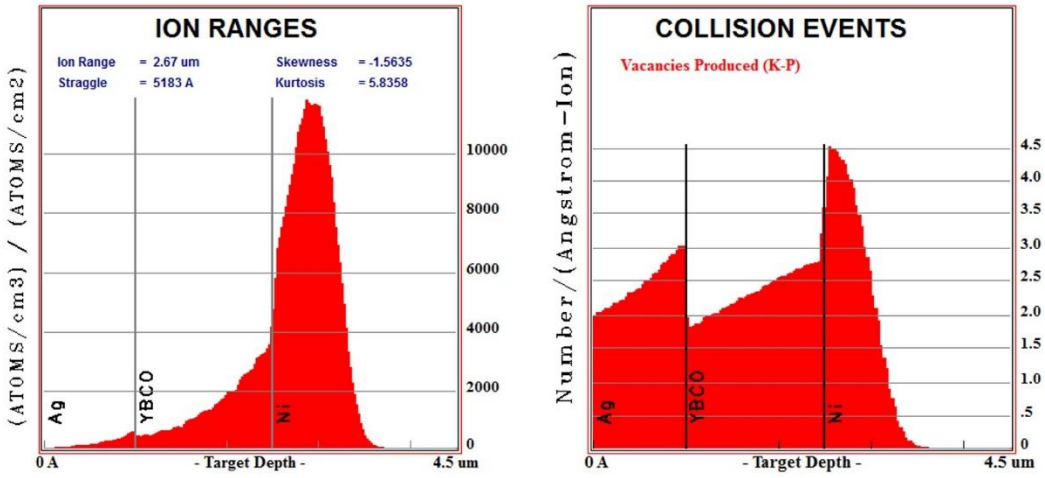

Figure 2.7 SRIM simulation result of 22 MeV gold ion irradiation for $YBa_2Cu_3O_{7-\delta}$ tape. Most of the incident ions stop in the metal substrate.

The result of the simulation shows that most of the 22 MeV gold ions barely penetrate the YBCO film and stop in the metal substrate (left panel). Collision events chart (right panel) shows the number of atoms in the target material hit by the incoming ions, which stands for the recoil process. Density of defects can be calculated through the collision number and the dosage. With the dosage from 8×10^{10} cm^{-2} to 2×10^{12} cm^{-2}, the defects created per volume unit varies from 1.8×10^{19} cm^{-3} to 4.6×10^{20} cm^{-3}.

2.2.2 Proton irradiation in $FeSe_{0.5}Te_{0.5}$ thin films

The FST films with micro-bridge patterned on the surface were covered by 1.5 μm thick aluminum foil mounted on a 4-inch Si wafer using silver paste (Fig. 2.8). Proton irradiation was carried out by Cutting Edge Ions LLC, Anaheim, CA. Two different proton energy, 190 KeV and 1 MeV were used. Dosages were set at 10^{15} cm^{-2} and 10^{16} cm^{-2} for 190 KeV energy, and 10^{16} cm^{-2} and 10^{17} cm^{-2} for 1 MeV energy. Magnetization measurement and electrical transport measurement were conducted before and after the irradiation.

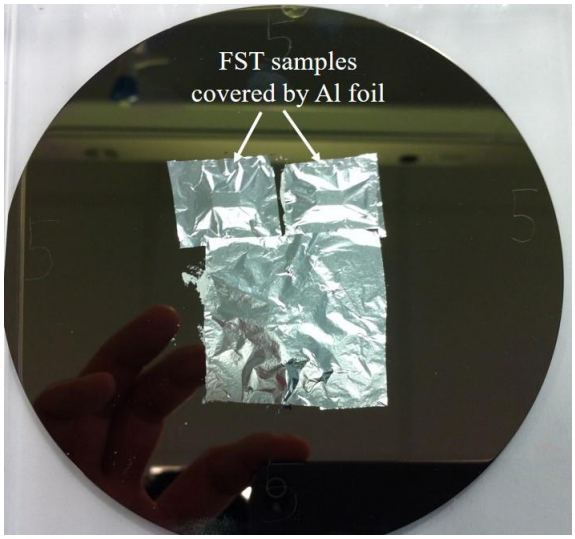

Figure 2.8 $FeSe_{0.5}Te_{0.5}$ samples on a 4-inch silicon wafer covered by 1.5 μm Al foil, prepared for being irradiated by protons.

The two chosen energies were for different scenarios, which are “implantation” and “penetration”. They were expected to create different types of defects and the discussion is presented in Chapter 3. 190 KeV irradiation would leave large amount of protons inside the FST film while 1 MeV irradiation would inject most of the protons

into the substrate beneath the FST film. The irradiations were simulated by SRIM code. Fig. 2.9 shows an example of the simulation result for 190 KeV proton irradiation.

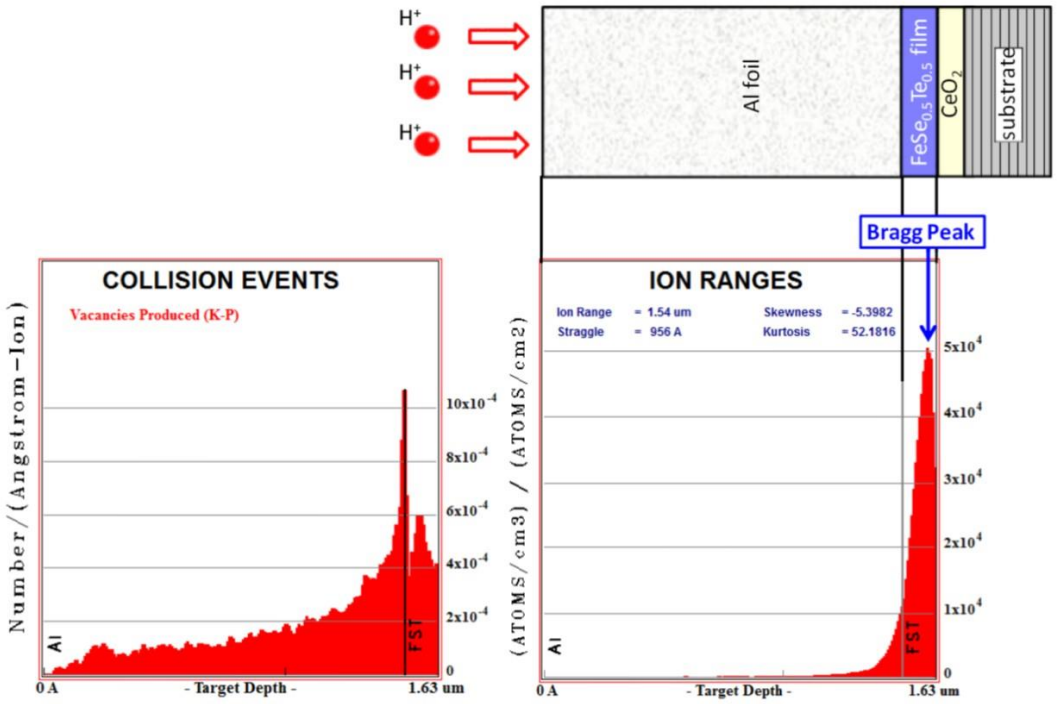

Figure 2.9 SRIM simulation result of 190 KeV proton irradiation for 130 nm thick $FeSe_{0.5}Te_{0.5}$ thin film. The Bragg peak shows inside the film.

The stopping range for 190 KeV protons is around 100 nm from the top of the FST film surface, where Bragg peak showed up, indicating the large energy loss in protons before finally stopped. For 10^{15} cm^{-2} dosage, the total number of the displacement per unit volume is calculated as 5.0×10^{19} cm^{-3}, leading to a mean distance of 3 nm between the introduced defects and an amount of displacement damage of 1.1×10^{-3} displacement per atom.

2.3 Annealing experiment

Oxygen annealing has been found to have positive effect on T_c and J_c in bulk FST materials by reacting with the excess iron, which was left in the sample during synthesis. For YBCO, oxygen annealing has also been proved as an effective method to rearrange the structure thus tune the landscape of the defects caused by ion irradiation.[58,102,103] It can partially recover the T_c.

In this dissertation, two sets of FST films were annealed in oxygen and vacuum environments after growth, to compare the difference in property change. Oxygen annealing for FST thin films was conducted in 100 mTorr oxygen at 90 °C. Samples were glued on the sample stage by silver paste and transferred into the old PLD chamber (Fig. 2.2a) for sequential annealing in four steps, with the annealing time of 15, 30, 60 and 120 minutes. Sequential vacuum annealing was done under the pressure of 10^{-8} Torr at 200 °C in Pascal PLD chamber (Fig. 2.2b), with the annealing time of 15, 30 and 60 minutes. After 3 steps of vacuum annealing, an additional 2-hour oxygen annealing was conducted at 90 °C, in order to compare the effect with and without the presence of oxygen. Magnetization measurements were performed to characterize T_c and J_c for as-grown films and after each step of annealing. The comparison of the annealing effect on two sets of films is presented in Chapter 3.

To get a comprehensive understanding of the oxygen annealing effect, some FST films were chosen to be placed in a desiccator, with the contact to the air, for one year long term aging. The aging experiment was expected to have a qualitatively similar

effect to low temperature oxygen annealing, for that the film reacts slowly with the oxygen in the air. Magnetization measurement was conducted before and after the aging.

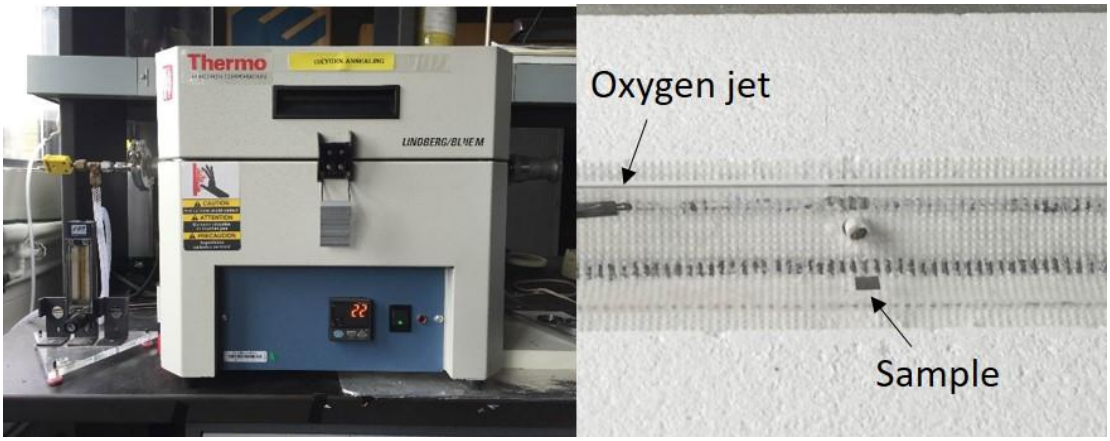

Figure 2.10 Lindburg tube furnace used in $YBa_2Cu_3O_{7-\delta}$ oxygen annealing experiment.

YBCO coated conductors were annealed in the oxygen environment after the irradiation using a Lindburg tube furnace, as shown in the left panel in Fig. 2.10. The right panel shows an enlarged picture for the middle part of the quartz tube, where the sample is placed during the annealing. Two steps of oxygen annealing experiment were conducted after irradiation: 200 ℃ for 12 hours and 300 ℃ for 1 hour, with the oxygen flow rate at 1 cm^3 per second. Three irradiated samples were selected in this experiment, with irradiation dosages of: 2×10^{11} cm^{-2}, 4×10^{11} cm^{-2}, and 6×10^{11} cm^{-2}. The reason to choose these samples is that they have the best J_c and T_c values after irradiation. Magnetization measurement was conducted after each step of the oxygen annealing.

2.4 Structural characterizations

2.4.1 X-ray diffraction

The Ultima III multipurpose X-ray diffraction system (Fig. 2.11) with Cu Kα radiation was used to characterize the phases in FST thin films. During the characterization, samples were put on a fixed stage and both the X-ray beam source and the detector are moving accordingly to conduct the scan. 2θ scans are obtained typically from 10 to 65 degrees, with a step size of 0.005 degree. Locations of peaks detected in the spectra were compared to the standard PDF database to identify the phase of the thin films.

Figure 2.11 Ultima III multipurpose X-ray diffraction system

2.4.2 Scanning electron microscopy (SEM)

Cross-sectional morphology characterization was conducted using Hitachi S-4800 scanning electron microscope, as shown in Fig. 2.12. One of the major purpose for SEM imaging is to measure the thickness of the FST films and CeO_2 buffer layers. After the synthesis, FST films along with the substrate were freshly cut vertically and mounted on the SEM vertical sample stage to expose the cross-section area under the scanning electrons.

Figure 2.12 Hitachi S-4800 scanning electron microscope

2.4.3 Transmission electron microscopy (TEM)

TEM images were taken to investigate the atomic-level structure in FST films, as well as the defect morphology after proton irradiation. Cross-sectional TEM samples were prepared using focus ion beam and were then characterized by using high resolution transmission electron microscopy (HRTEM).

2.5 Transport and magnetization measurement

Transport properties of superconducting materials are crucial on the aspect of applications. It is also the major part in this dissertation. As was described in the introduction, transport-wise, there are three key parameters for superconductors: T_c, J_c and H_{c2}. Two methods of measurement were conducted on the samples to obtain these important parameters, as described below.

2.5.1 Electrical transport measurement

Electrical transport properties directly reflect the superconductivity in materials. In this dissertation, most of the electrical transport measurements were conducted using Physical Property Measurement System (PPMS), shown in Fig. 2.13a, manufactured by Quantum Design. The cryogenic system is sourced by liquid helium and the temperature can be controlled between 1.8 K and 400 K with the resolution of 0.01 K. It is equipped with a magnet which can provide a magnetic field up to 9 Tesla. 12-pin DC resistivity sample puck enables 3 independent channels to measure simultaneously (Fig. 2.13b). Electrical current through DC bridge can be set from 5 nA to 5 mA in high resolution mode. When using AC module, the current can be charged up to 1000 mA. The system also includes a rotator puck which can be controlled by a motor and enables angular dependent resistivity measurement (Fig. 2.13c).

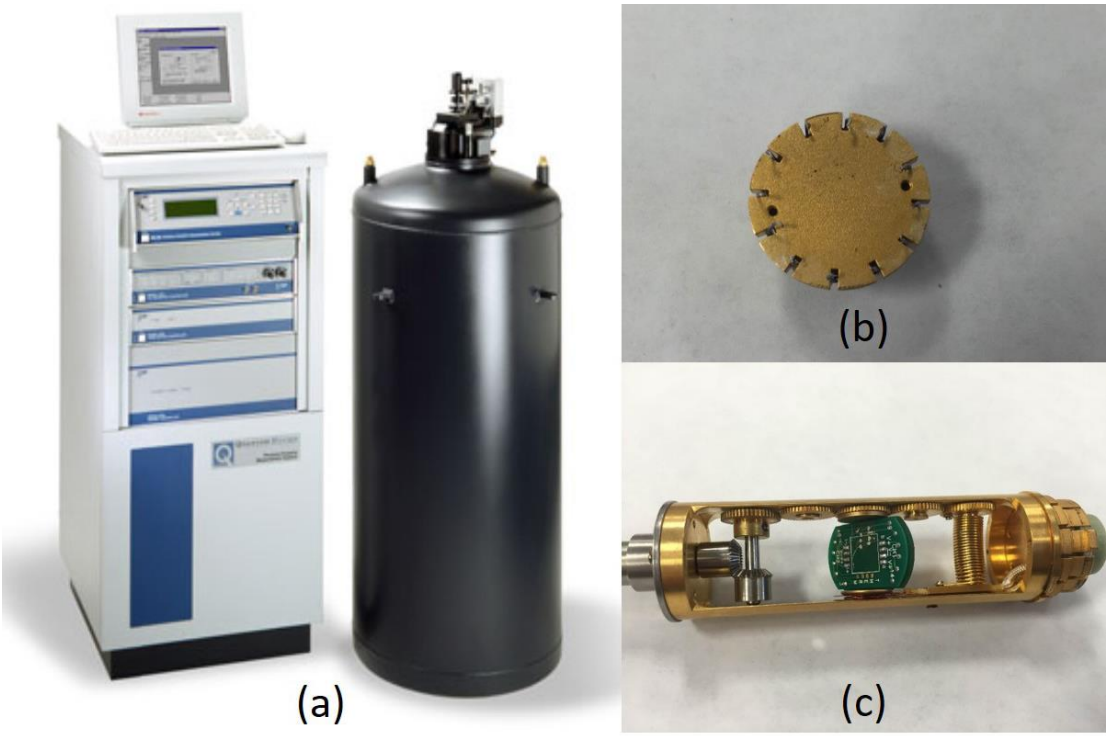

Figure 2.13 Physical Property Measurement System (a), equipped with 12-pin DC sample puck (b) and AC sample rotator (c).

FST films were measured using PPMS with micro-bridges patterned (see Section 2.2). The prepared sample was glued on a piece of micro glass using non-conductive varnish. Standard four-probe contact configuration was used for resistivity measurement, as shown in Fig. 2.14. Four gold wires, two current leads on the side and two voltage leads in the middle, were attached to the film surface with silver paint as the contact. The other ends of gold wires were connected to DC resistivity puck or AC sample holder by soldering. Gold wires were anchored on the micro glass by silver paint in order to protect the contacts when bonding to DC resistivity puck or AC sample holder. Rotator was used to tune the sample position, in order to measure the properties

under different field direction. In this dissertation, all resistivity measurement for FST films were under a 100 μA excitation current.

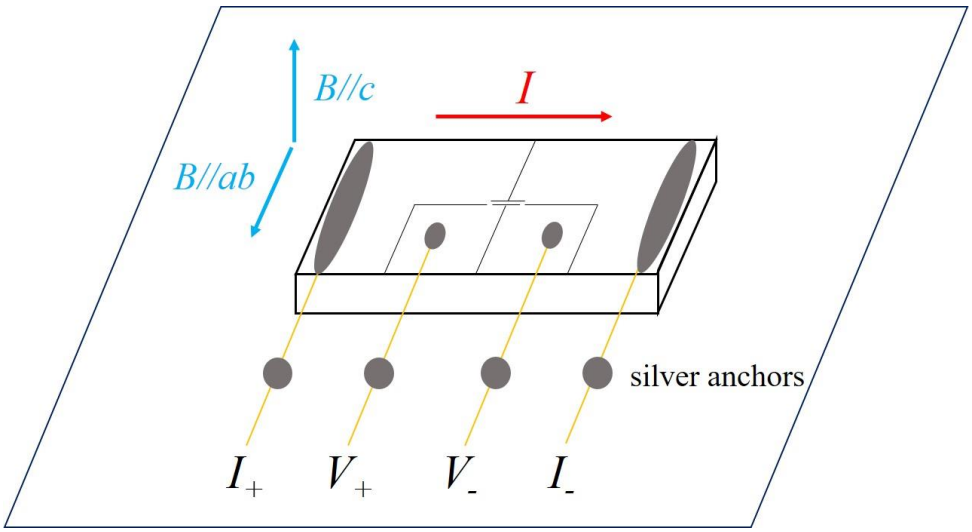

Figure 2.14 Contact configuration on patterned $FeSe_{0.5}Te_{0.5}$ film for electrical transport measurement.

Besides using PPMS, part of the measurements were done in National High Magnetic Field Laboratory (NHMFL), in order to obtain the superconducting properties under high magnetic field. Electrical transport measurement for FST films was performed in Cell 12 in NHMFL located in Tallahassee, Florida (Fig. 2.15). The powerful magnet enables high magnetic field up to 34.5 T.

Figure 2.15 Cell 12 in National High Magnetic Field Laboratory, equipped with a 34.5 T magnet.

2.5.2 Magnetization measurement

The unique magnetization behavior in superconductors enables another way to characterize the superconductivity. Magnetization measurements were conducted using Magnetic Property Measurement System (MPMS), as shown in the left panel in Fig. 2.16, manufactured by Quantum Design.

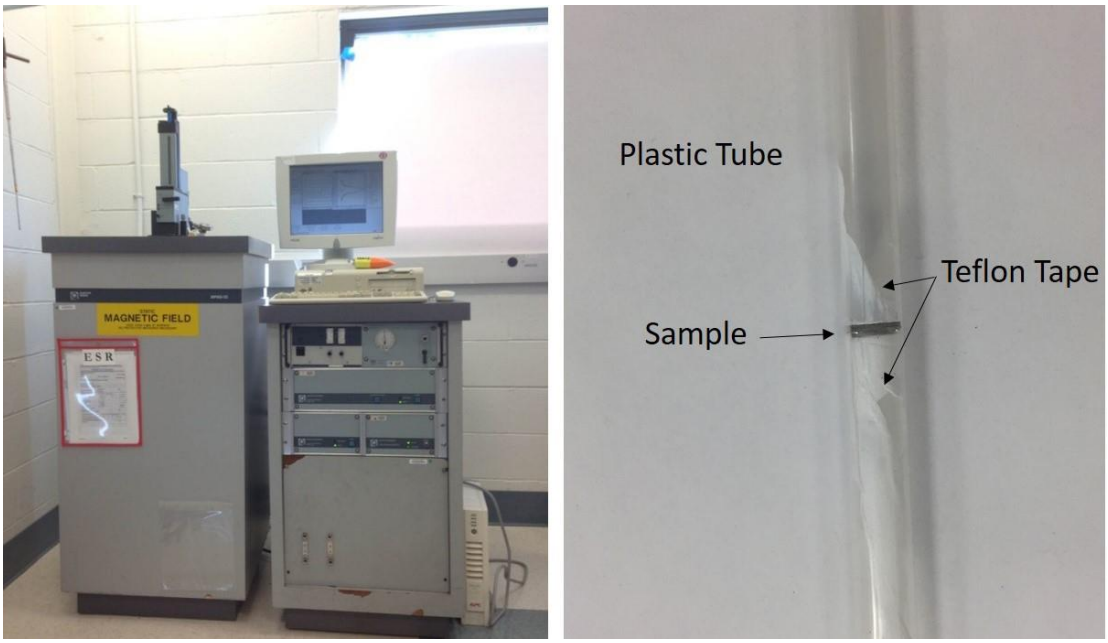

Figure 2.16 Magnetic Property Measurement System (left) and a $FeSe_{0.5}Te_{0.5}$ sample prepared for magnetization measurement (right).

Compared to electrical transport measurement, magnetization measurement is simple and non-destructive to the sample. There is no need for patterning or leads contacting for magnetic measurement, making it particularly suitable for continuously monitoring the property change. Samples, in a whole with the substrates, were fixed in plastic tubes prior to the measurement, as shown in the right panel in Fig. 2.16. In detail, three plastic tubes were used: an outer one and two inner ones. The outer tube was used as a shell and container for inter tubes and the sample. Two inner tubes were used to fix the sample in position with Teflon tape wrapped to protect the sample surface. They were then mounted on the sample holder and put into the MPMS for magnetization measurement, with the filed perpendicular to the sample surface. T_c and J_c can be derived using the method described in Section 2.5.3.

2.5.3 Data analysis

T_c, J_c and H_{c2} are core properties for the application of superconducting materials. After the measurement, the result data was analyzed using the method and criteria as described below.

For electrical transport measurement, zero resistance T_c, or T_c^0, is defined as the temperature at which the resistivity of the sample is 1% of its normal state resistivity, ρ_n, or so-called $0.01\rho_n$ criteria. Onset T_c, or T_c^{onset}, is obtained using $0.9\rho_n$ criteria – the temperature at which the resistivity reaches 90% of the normal state resistivity. Irreversibility field H_{irr} and upper critical field H_{c2} were also obtained using $0.01\rho_n$ and $0.90\rho_n$ criteria, similar to T_c^0 and T_c^{onset} but with the variable of magnetic field instead of temperature.

Transport critical current I_c was derived from VI characteristic curve measured by scanning excitation current on the patterned micro-bridge. In superconducting state, the voltage signal shows constant zero, or practically a very tiny value due to the background noise, as a flat line shown in VI curve. As the current increases, the superconducting state starts breaking up and the flat line instantly rises. In this dissertation, the corresponding current point where the VI curve deviated from the flat line (exceeding 1μV) was defined as the critical current I_c. Critical current density J_c is calculated by I_c/wt, where w is the bridge width and t is the sample thickness.

Magnetization T_c, can be easily obtained from magnetization measurement using MPMS. If the material was cooled down below its T_c without external field, or so called zero field cool (ZFC), then an external magnetic field is applied at low temperature, it

gives a negative magnetic moment signal due to the diamagnetism. As the temperature increases reaching its T_c, an obvious change on the magnetic moment from negative to zero would show up. If the magnetic field was applied to the material above its T_c prior to the cooling, or so called field cool (FC), magnetic flux stays inside the material and the temperature dependent magnetic moment curve deviates from the ZFC curve below T_c. The deviation point is defined as its magnetization T_c. This T_c is usually very close to, but a little lower than electrical transport T_c^0. The difference between these two values is usually around 1 K in the experiments included in this dissertation.

For magnetization measurement in well-established YBCO tapes, only ZFC curves were measured in order to save time and resources. Thanks to the sharp transition in YBCO, the T_c can be easily obtained by locating the temperature at which the ZFC curve deviates from the extrapolation of its flat part at the temperature above the superconducting transition. In Chapter 4, all magnetization T_c presented were obtained this way with the magnetic moment deviation of 1% of the magnetic moment at 60 K.

J_c can also be derived from the measurement of the magnetic hysteresis loop using Bean Critical Model:[104]

$$J_c = \frac{20\Delta M}{b(1-b/3a)},$$

where, a and b are sample width ($a > b$) on the plane perpendicular to the applied field, ΔM is the absolute value of magnetic moment change per unit volume between field increase and decrease.

3. Transport Properties of $FeSe_{0.5}Te_{0.5}$ Superconducting Thin Films

3.1 Structure and superconducting properties of as-grown $FeSe_{0.5}Te_{0.5}$ films

FST films were synthesized using PLD described above. After growth, the film on single crystal substrate shows a shining metal-like surface, as shown in the left panel in Fig. 3.1. The dimensions of the sample were typically 5 mm by 3 mm, as the substrates were cut at this size prior to the film growth. The thickness of the FST films and the CeO_2 buffer layers were about 130 nm and 110 nm, characterized by cross-section SEM, as shown in the right panel in Fig. 3.1. The bottom bright region is the STO single crystal substrate. The dark top layer is the FST film, and the grey layer between FST and the substrate is CeO_2 buffer. During the study, over one hundred FST films were synthesized and the thickness of the films grown during different period varies between 120 nm and 135 nm.

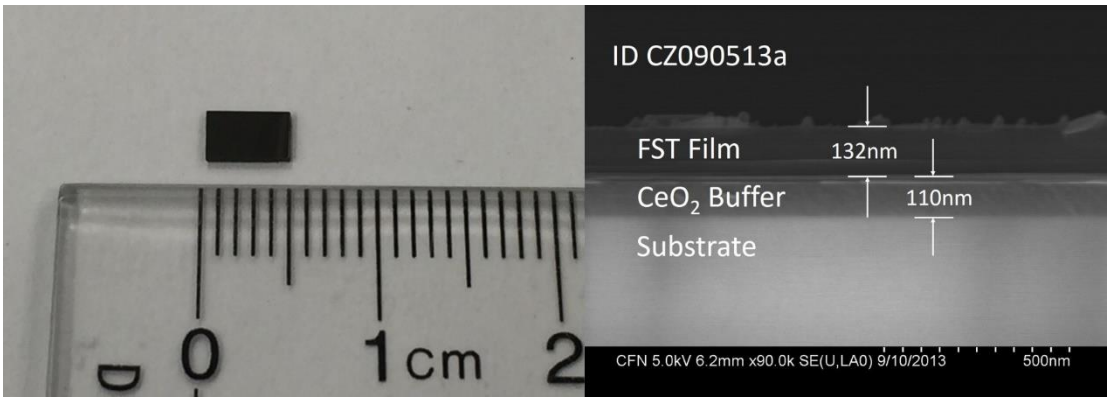

Figure 3.1 Dimensions of a typical $FeSe_{0.5}Te_{0.5}$ thin film sample. The thickness is 132 nm characterized by cross-sectional scanning electron microscopy.

Fig. 3.2 shows the XRD result of two typical FST films for phase and structure characterization. They were grown on different substrates –STO (Fig. 3.2a) and YSZ (Fig. 3.2b). In the scanned 2θ range, four FST (00l) peaks and one CeO_2 (200) peak are present at the same position. For both samples, only the (00l) peaks from the FST films, CeO_2 buffer and substrates are present, indicating good out-of-plane alignment.

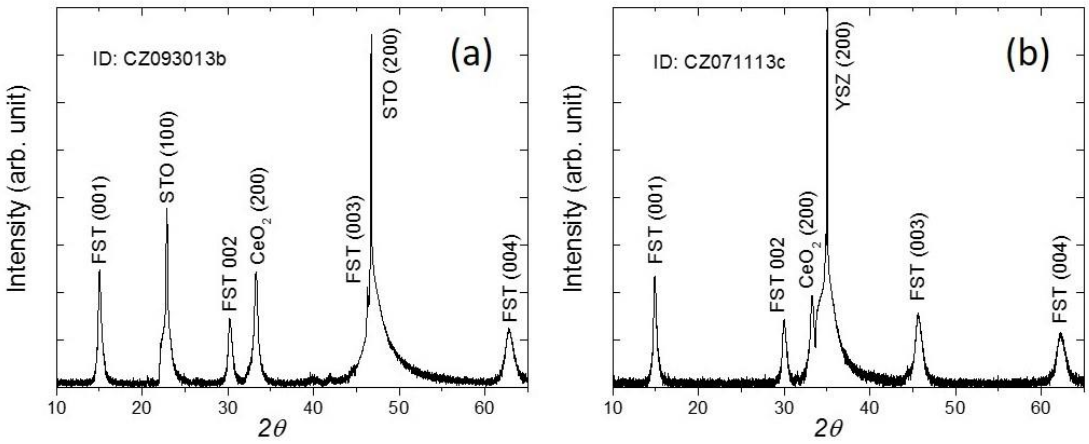

Figure 3.2 XRD θ-2θ scan of $FeSe_{0.5}Te_{0.5}$ thin films grown on (100) STO (a) and (100) YSZ substrates (b) with CeO_2 buffer layers. Only (00l) peaks are shown, indicating the films are epitaxially grown.

Electrical transport measurements were performed on these films to investigate the superconducting properties. Fig. 3.3 shows the resistive superconducting transitions of FST bulk material and FST films with and without CeO_2 buffer layers. In order to compare the superconducting transition in different samples, resistance was normalized as R/R^* where R^* is the normal state resistance at 22 K. It is clearly seen that FST in the form of thin film has higher T_c than that of bulk. Single crystal bulk FST material has a T_c^0 at 13.9 K. T_c^0 for FST films directly grown on single crystal substrates varies

from 15.5 K to 16.2 K, about 2 K higher than bulk T_c^0. The onset T_c for FST films is between 18.5 K and 18.8 K. With the a CeO_2 buffer layer, the T_c^0 of FST films can reach as high as 18 K and the T_c^{onset} reaches 19.2 K.

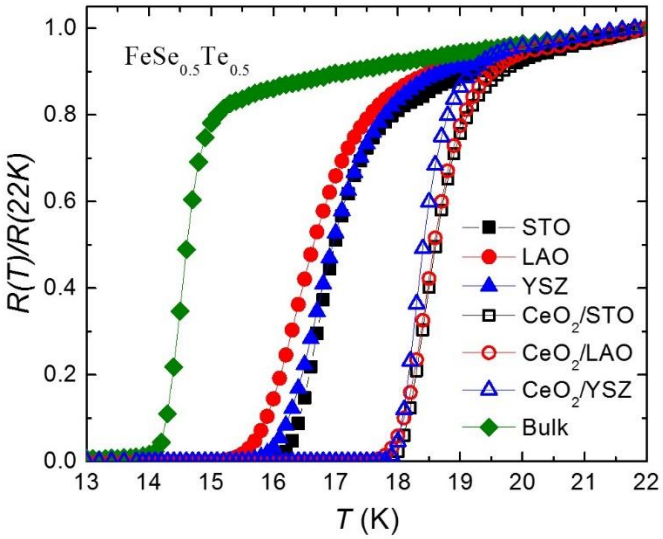

Figure 3.3 Normalized temperature dependent resistance curves of $FeSe_{0.5}Te_{0.5}$ films on varies substrates and of the bulk material. Films with buffer layers have a zero resistance T_c of 18 K, 4 K higher than that of bulk.

The T_c^0 in FST films shows slight variation when directly grown on different substrate which might be due to the different lattice mismatch. However, after introducing the buffer layer, this variation is reduced to below 0.3 K. Even for the films grown on the same substrate, larger differences may sometimes present between batches due to the variation of deposition temperature and pressure. Later in this chapter, all the FST films involved were the ones grown with the CeO_2 buffer layer.

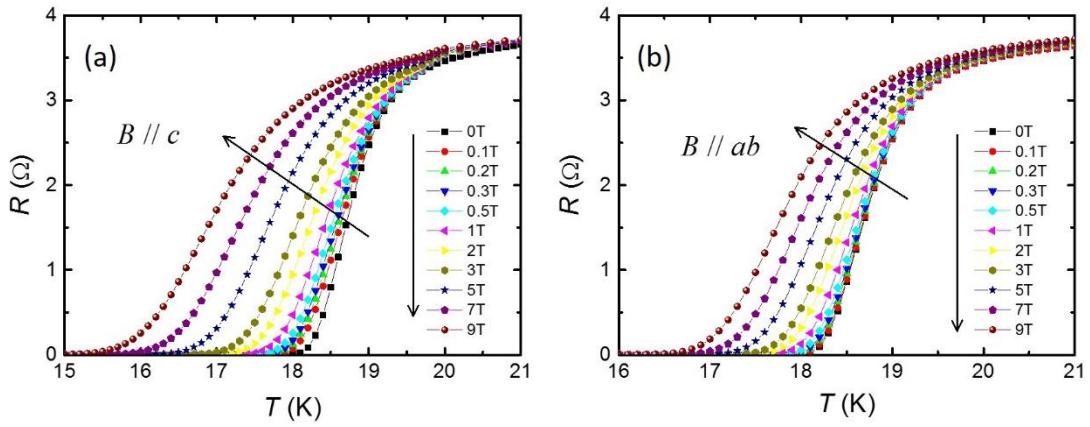

Figure 3.4 Temperature dependent resistance of $FeSe_{0.5}Te_{0.5}$ films with the CeO_2 buffer layers under the field applied parallel to *c*-axis (a) and parallel to *ab*-plane (b).

Detailed transport measurement was conducted on the FST films with the magnetic field applied along two directions: *B*//*c*-axis and *B*//*ab*-plane. Fig. 3.4 shows the measurement result for one of the FST/CeO_2/STO samples. It shows that even under 9 T external field, the film has a T_c^0 above 15 K and 16.5 K for *B*//*c*-axis and *B*//*ab*-plane, respectively, indicating an excellent in-field superconducting performance.

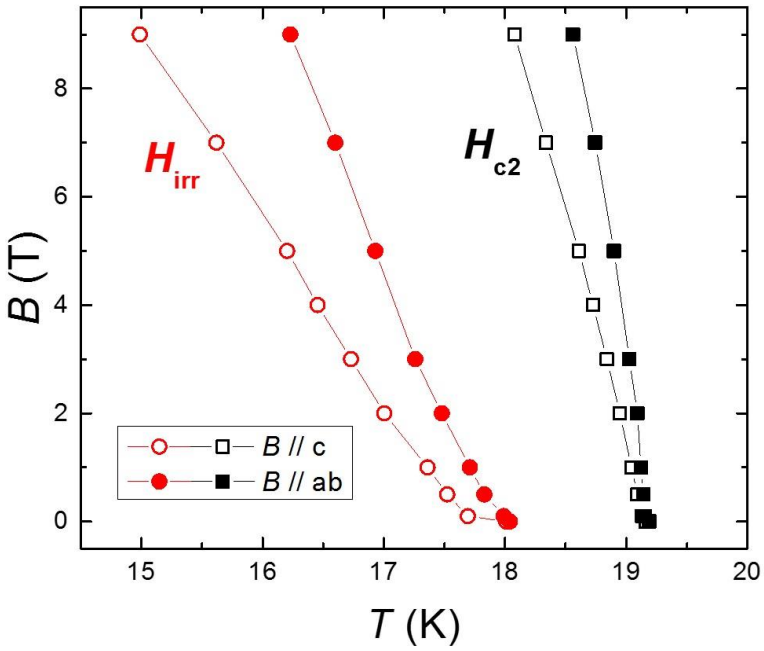

Figure 3.5 Irreversibility field and upper critical field as a function of temperature in $FeSe_{0.5}Te_{0.5}$ film with the field applied parallel and perpendicular to film surface.

Fig. 3.5 shows the temperature dependence of irreversibility field H_{irr} and upper critical field H_{c2}, derived from Fig. 3.4 by the criteria described in Section 2.5. Both H_{irr} and H_{c2} are higher when the magnetic field applied in-plane, due to the layered crystal structure. The ratio of H_{c2}^{ab}/ H_{c2}^{c} is between ~2, showing a less anisotropy than other iron-based superconductors reported[13,105].

Superconducting properties of the film were also characterized by magnetization measurement. As shown in Fig. 3.6a, ZFC and FC curves merged at 17.4 K. This magnetization T_c is about half degree lower than the electrical transport T_c. The flat bottom of ZFC at low temperature indicates a stabilized diamagnetism, indicating the good homogeneity of the film.

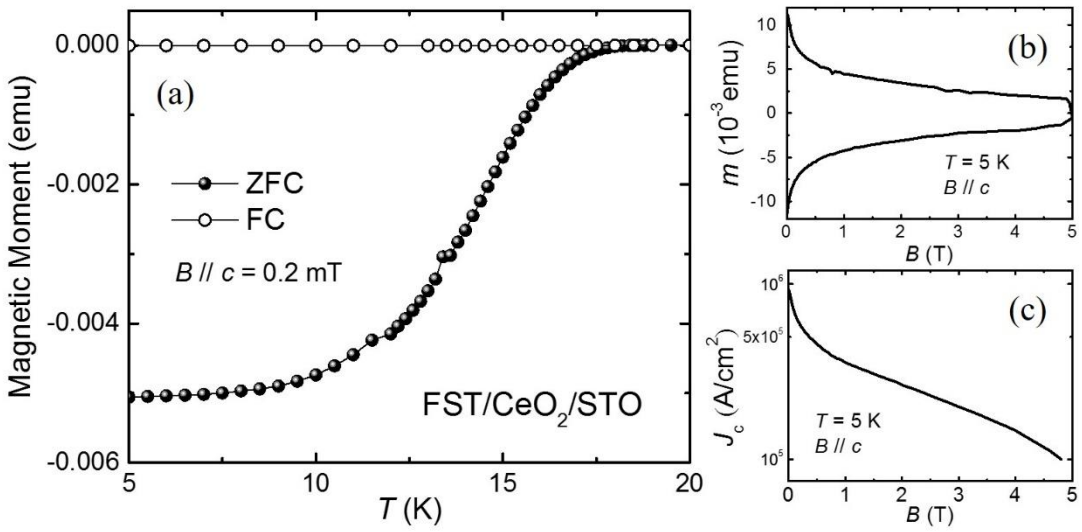

Figure 3.6 Magnetization measurement result of a typical $FeSe_{0.5}Te_{0.5}$ film, in terms of temperature dependent magnetic moment (a), magnetic half-hysteresis loop (b) and J_c as a function of magnetic field (c). Self-field J_c at 5 K is close to 1 MA/cm^2.

Magnetic hysteresis loop (*MH* loop) for the film was measured at 5 K and the result is shown in Fig. 3.6b. For the purpose of effectively extracting J_c, the *MH* loop was measured as a half-loop, started from -2 T to 5 T and went back to zero. Field dependent J_c at 5 K were calculated from the *MH* measurement using the Bean model, and the result is shown in Fig. 3.6c. J_c of the thin film sample is 0.93 MA/cm^2 at zero field (self-field) and keeps above 10^5 A/cm^2 under the magnetic field up to 5 T. Note that J_c of the films grown directly on single crystal substrates, without CeO_2 buffer layers, was never reach above 0.5 MA/cm^2 at 5 K under self-field.

3.2 Annealing effect in $FeSe_{0.5}Te_{0.5}$ films

After growth, two sets of films were sequentially annealed as described in Section 2.3. The measurement results for two typical films, film A and B, grown from the same batch and annealed in different atmosphere, are presented in this section.

For a clear view, Table 3.1 shows the annealing time and atmosphere for film A and B. Magnetization measurement was done on as-grown films and after each step of annealing. The result data is labelled as shown in brackets in Table 3.1. Oa0 and Va0 stand for as-grown film A and B, respectively.

Annealing Time	15 min	30 min	60 min	120 min
Film A	100 mT O_2 (Oa1)	100 mT O_2 (Oa2)	100 mT O_2 (Oa3)	100 mT O_2 (Oa4)
Film B	10^{-8} Torr (Va1)	10^{-8} Torr (Va2)	10^{-8} Torr (Va3)	100 mT O_2 (Va3+Oa)

Table 3.1 Time and atmosphere in $FeSe_{0.5}Te_{0.5}$ film annealing experiment.

Figure 3.7 shows temperature dependent magnetic moment for oxygen annealed film A, under an external magnetic field of 0.2 mT, perpendicular to the film surface. It is seen that T_c has gradually decreased as the annealing conducted step by step. The total change of T_c is 1.4 K after four steps of oxygen annealing, from 17.6 K to 16.2 K. While the superconducting transition becomes sharper after annealing. If using the criteria from $0.1m$ to $0.9m$, where m is the magnetic moment measured at 5 K, to define the magnetic superconducting transition width ΔT_c, the as-grown sample shows a ΔT_c of 4.8 K. This ΔT_c reduced to 2.8 K after four steps of oxygen annealing. The total change of ΔT_c is 2 K, larger than the degradation of T_c. It is noticed that the results after

the third and the forth annealing are almost the same and no further T_c change is observed.

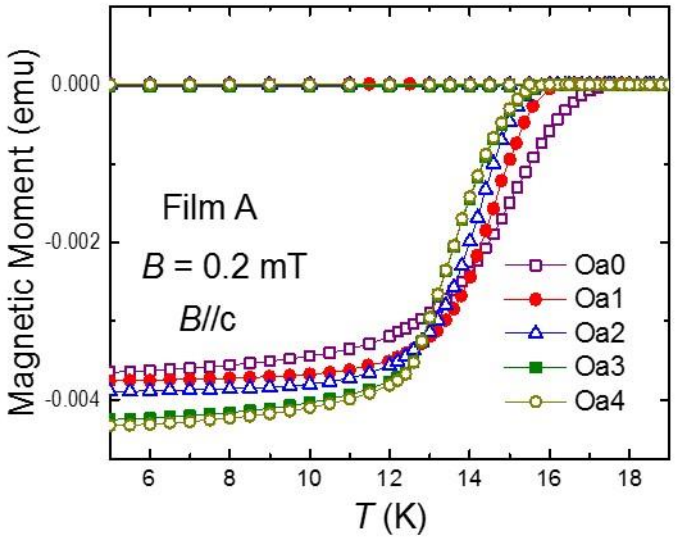

Figure 3.7 Temperature dependent magnetic moment in film A at each step of oxygen annealing, under the external field of 0.2 mT applied perpendicular to the film surface. Sharper transition and lower onset T_c are found after annealing.

The half *MH* loops measured at 5 K after each step of annealing are shown in Fig. 3.8a. It is seen that the area inside the loop increases during the annealing, suggesting higher J_c. Similar to the temperature dependent magnetic moment, Oa3 and Oa4 curves are almost identical, indicating the saturation of the oxygen annealing effect.

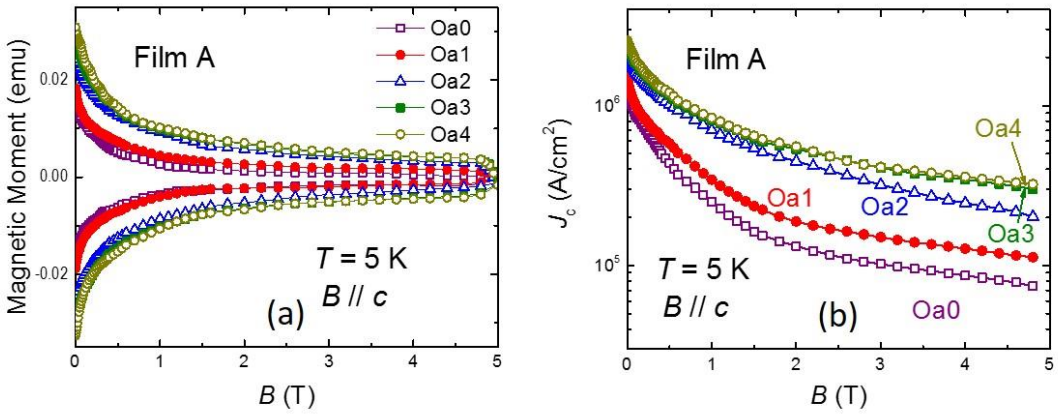

Figure 3.8 Half magnetization loops (a) and derived J_c as a function of magnetic field (b) for film A after each step of oxygen annealing at the temperature of 5 K. J_c keeps increasing during the annealing before saturated at the last step.

Field dependent J_c at 5 K is derived from the measurement of the half *MH* loop and the result is plotted in Fig. 3.8b. Self-field J_c has been enhanced from 1.24 MA/cm^2 to 2.54 MA/cm^2, more than doubled, after a series of oxygen annealing. High field J_c has also been enhanced. Above 2 T, over four-fold enhancement is observed. The difference between Oa3 and Oa4 curves is very small. The enhancement of J_c at 5 K as a function of the applied field is plotted in Fig. 3.9. J_c gain is calculated as $J_c^{annealed}/J_c^{pristine}$ - 1. Under the 3 T field, the enhancement after each step of annealing is approximately 50%, 200%, 300% and 310%, respectively.

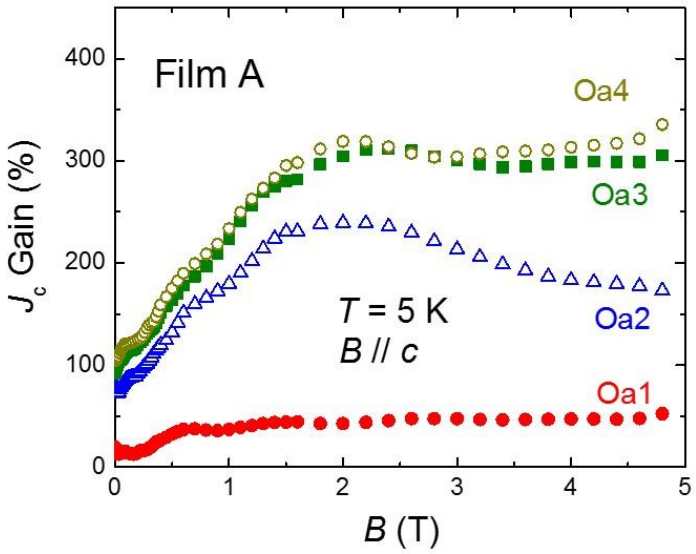

Figure 3.9 Field dependent J_c enhancement for film A after each step of oxygen annealing at 5 K. 300% enhancement is found above 2 T after fully annealed.

Magnetization measurement for vacuum annealed film B is shown in Fig. 3.10, plotted in the same style. T_c in film B has changed by 1.2 K, from 17.2 K to 16 K, after three steps of vacuum annealing, similar to the oxygen annealed ones. Sharper superconducting transition is also observed after annealing, and the sharpness increases as the annealing continues. The total change of transition width ΔT_c is 1.7 K after annealing, larger than the degradation of T_c. Comparing the result of oxygen annealing and vacuum annealing, one can conclude that these two types of annealing process have generally the same influence on the aspect of T_c, regardless the presence of oxygen. The reason for the T_c change after annealing will be discussed in Section 3.4.

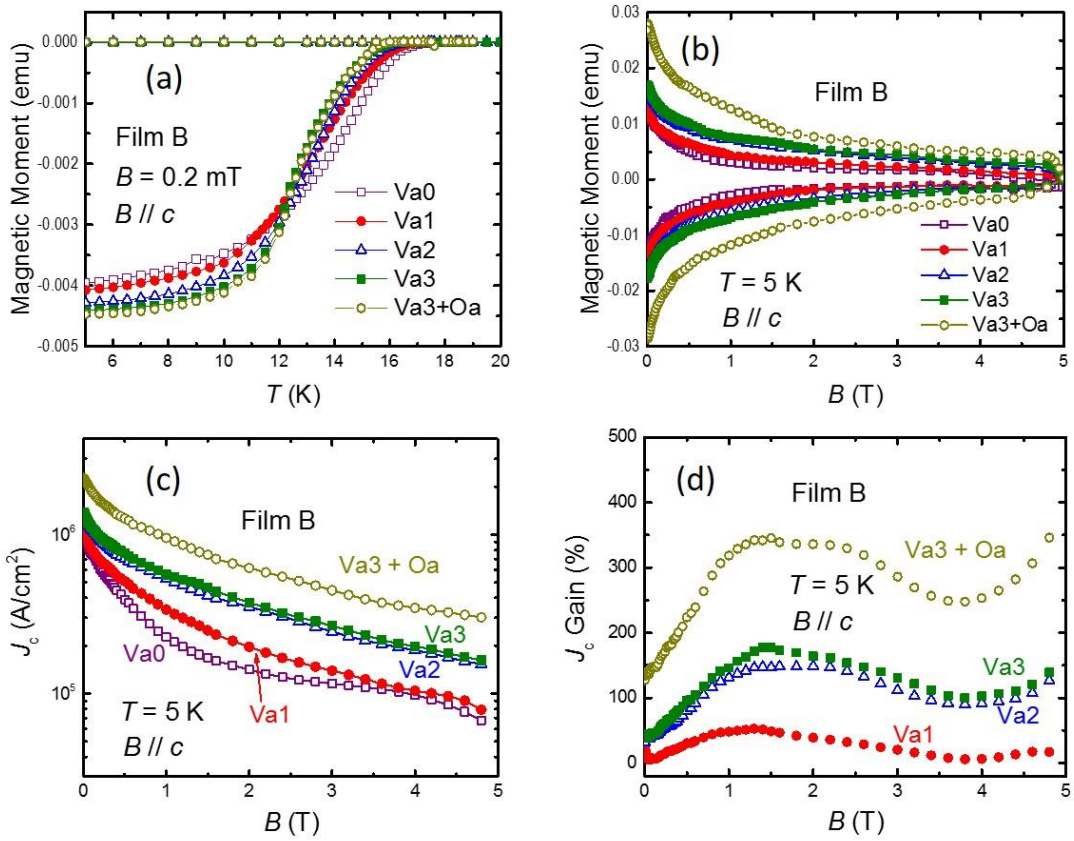

Figure 3.10 Magnetization measurement result of $FeSe_{0.5}Te_{0.5}$ film B for three steps of vacuum annealing and one additional oxygen annealing, in terms of temperature dependent magnetic moment (a), half magnetization loops (b), derived J_c (c) and J_c enhancement (d) as a function of the magnetic field. Small J_c enhancement is observed in fully vacuum annealed film and a significant enhancement is found after the additional oxygen annealing.

However, things are different on the aspect of J_c. The J_c enhancement induced by vacuum annealing saturates after three steps, and is much less than that after the oxygen annealing. The self-field J_c in this fully vacuum annealed film is 1.38 MA/cm^2, ~38% above that of the as-grown film and the average in-field J_c enhancement is less than

150%. This overall J_c enhancement, even though saturated, is even far less than the one observed in film A after the first two steps of oxygen annealing.

The large difference in J_c change between oxygen annealed and vacuum annealed samples indicates the importance of oxygen. However, one cannot completely rule out the possibility that it is due to the intrinsic quality difference between the two films, given that the self-field J_c is 1.24 MA/cm^2 in film A and only 1 MA/cm^2 in film B. In order to address this question, an additional 2-hour oxygen annealing was conducted on film B which had already being fully vacuum annealed. The result is plotted in Fig. 3.10 (open circles) for comparison, labelled as "Va3+Oa". It is clearly seen that J_c after this additional oxygen annealing increases significantly to 2.27 MA/cm^2 at self-field and in-field (B > 1 T) J_c enhancement reaches the level around 300%. This result is comparable to that of fully oxygen annealed film A. This means that the existence of oxygen is responsible for the big difference of J_c enhancement between two types of annealing. On the aspect of T_c this additional oxygen annealing shows virtually no effect upon vacuum annealing.

Table 3.2 lists detailed measurement result of this series of annealing experiment on film A and B.

		T_c^M (K)	ΔT_c^M (K)	ΔT_T (K)	J_c(0T) (MA/cm^2)	J_c(0T) Gain	J_c(3T) (KA/cm^2)	J_c(3T) Gain
Film A	**Oa0**	17.6	N/A	4.8	1.24	N/A	102	N/A
	Oa1	16.6	-1	3.0	1.48	19.4%	156	52.9%
	Oa2	16.4	-1.2	2.9	2.20	77.4%	318	212%
	Oa3	16.2	-1.4	2.8	2.38	91.9%	407	299%
	Oa4	16.2	-1.4	2.8	2.54	104.8%	415	307%
Film B	**Va0**	17.8	N/A	6.2	1.00	N/A	115	N/A
	Va1	17.4	-0.4	5.3	1.19	19%	138	20.0%
	Va2	17.2	-0.6	4.9	1.32	32%	244	122%
	Va3	16.6	-1.2	4.5	1.38	38%	268	133%
	Va3+Oa	16.6	-1.2	4.5	2.27	127%	452	293%

Table 3.2 Detailed measurement result of $FeSe_{0.5}Te_{0.5}$ thin film annealing experiment.

The process has been repeated in multiple films, where a similar magnitude of J_c enhancement was achieved. The highest self-field J_c in fully oxygen annealed films reaches 2.94 MA/cm^2 at 5 K. The result suggests that oxygen can interact with the film and have the J_c enhanced at the temperature as low as 90 ℃. Based on this, one can guess that similar enhancement may be obtained at room temperature in a rather slower process. Several films were then selected for long term aging as described in Section 2.3. Blue squares in Fig. 3.11 shows the aging effect on field dependent J_c in one of the as-grown film, labelled as film C. After one year stored in the air, J_c in film C has been enhanced: the self-field J_c increases from 0.96 MA/cm^2 to 1.53 MA/cm^2 and the in-field J_c increases by 90% ~ 100% from 2T to 4.5T. This overall J_c enhancement is in qualitative agreement with the oxygen annealing. On the other hand, for fully oxygen annealed film A, the one shown in Fig 3.7 ~ 3.9, the one-year aging produces virtually no effect. The average difference of field dependent J_c before and after the aging is within 5%.

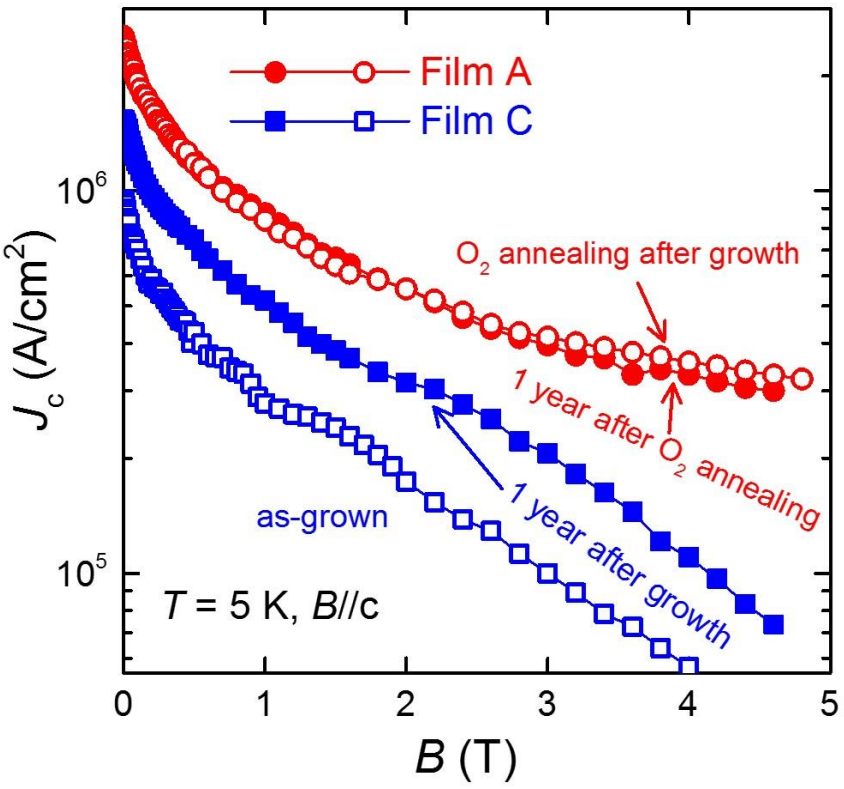

Figure 3.11 Field dependent J_c before and after long term aging in oxygen annealed film A and as-grown film C. An obvious J_c enhancement is found in film C while J_c in film A has virtually no change.

For a comprehensive understanding, oxygen annealing was conducted on aged films and further enhancement were observed, with a smaller magnitude of J_c enhancement compared to that of films annealed in oxygen right after growth. It indicates the mechanism behind aging and oxygen annealing is likely to be the same. Detail discussions will be brought out later in this chapter.

Electrical transport measurement was conducted on film A by patterning micro bridges on the surface after annealing and aging, to check the consistency of the

magnetization measurement result. Figure 3.12a shows the normalized electrical resistance as a function of temperature under different external magnetic field applied perpendicular to the film surface. Detectable resistance shows at 17 K at zero field, and gradually moves down to 14.5 K as the field rises up to 9 T. The zero field transition width is within 1 K if using 0.01~0.9 normal state resistance criteria. The transport T_c^0 is about 1 K lower than that of measured in as-grown films shown in Fig. 3.3 and 3.4. This is in line with the magnetization measurement result which shows the T_c degradation after annealing. Figure 3.12b shows the transport J_c at different temperatures as a function of the magnetic field up to 9 T, together with the magnetization-derived J_c at T = 5 K (solid circles in Fig. 3.11). It is seen that the J_c values obtained by the transport measurement and magnetization measurement are virtually the same, with the average deviation below 10%. The result reflects the reliability of the previous magnetization measurements during the annealing process.

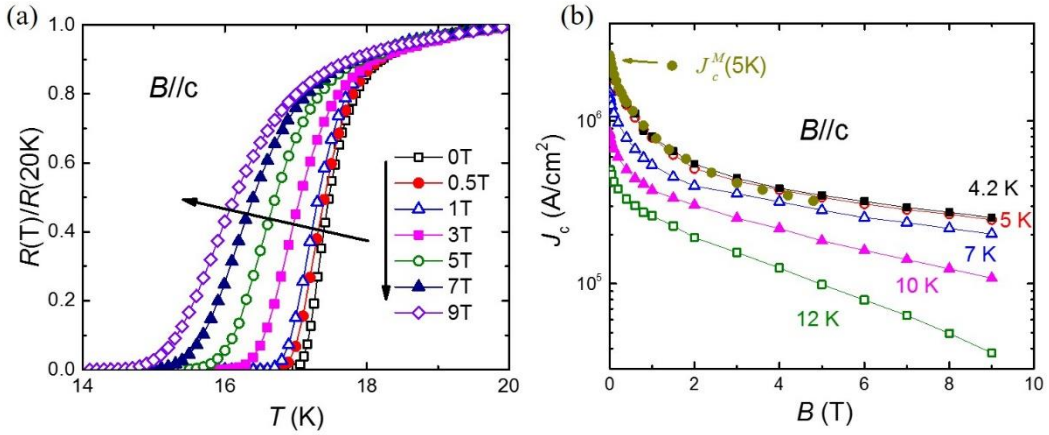

Figure 3.12 Electrical transport measurement result of film A after oxygen annealing and aging: normalized resistance as a function of temperature under different field (a) and field dependent J_c at various temperatures. Transport J_c is in well consistency with the magnetic measurement.

3.3 Superconducting property of FST thin films after proton irradiation

A series of samples were proton irradiated and the measurement result of six samples on zero field T_c is shown in Table 3.3, labelled as S1 to S6. Large T_c degradations were observed in samples irradiated by 1 MeV protons, as well as in the samples irradiated by 190 KeV protons with the dosage of 10^{16} cm^{-2}. Surprisingly, a T_c enhancement, though not much, was found in the samples irradiated by 190 KeV protons at 10^{15} cm^{-2}.

	190 KeV				1 MeV	
	S1 10^{15} cm^{-2}	S2* 10^{15} cm^{-2}	S3 10^{16} cm^{-2}	S4 10^{16} cm^{-2}	S5 10^{16} cm^{-2}	S6 10^{17} cm^{-2}
T_c^M pristine (K)	16.2	16.5 (18)	16.2	17.0	17.2	16.8
T_c^M irradiated (K)	16.7	N/A(18.5)	13.0	13.0	7.6	9.0
T_c^M change (K)	0.5	N/A (0.5)	-2.8	-4.0	-9.6	-6.8

*T_c^M stands for magnetization T_c. S2 for 10^{15} cm^{-2} dosage was patterned before irradiation and the numbers shown in brackets are electrical transport T_c^0.

Table 3.3 T_c for $FeSe_{0.5}Te_{0.5}$ films before and after proton irradiation.

It is interesting to observe the T_c enchantment, rather than degradation after the irradiation. Characterization through HRTEM was conducted by Dr. L. Wu (our collaborator from Condensed Matter Physics and Materials Science Department at Brookhaven National Laboratory) to examine the structural change in these films irradiated by 190 KeV protons at the dosage of 10^{15} cm^{-2}, as shown in Figure 3.13 in the cross-sectional view. Yellow dashed arrow indicates the direction of *c*-axis in the film and white arrows indicate the defects induced by protons. These splayed

disordered cascade defects were observed over the entire film. An enlarged view of a typical cascade defect is shown in inset, where a strain field was created in nearby area. This defect landscape could be responsible for the T_c enhancement and a proposed underline mechanism will be discussed later in the chapter, after presenting the detailed transport result.

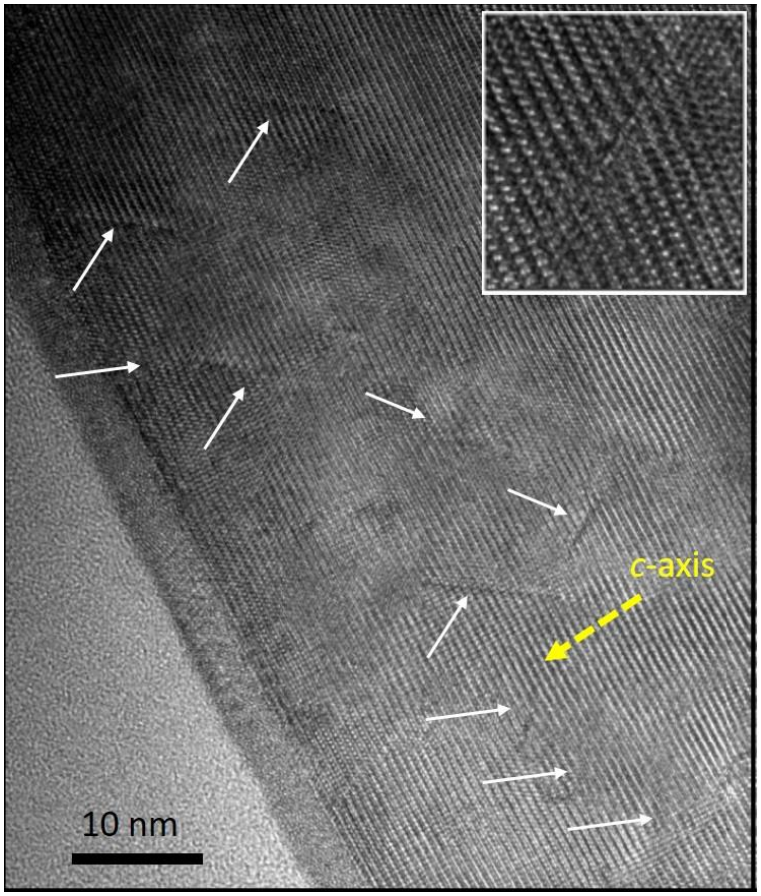

Figure 3.13 HRTEM image of a FST film irradiated by 190 KeV proton at the dosage of 10^{15} cm^{-2}. Disordered cascade defects are observed in the entire film. Inset shows an enlarged area where strain field produced by a splayed cascade defect.

A careful electrical transport measurement was performed on film S2, through the micro-bridge patterned on it, before and after being irradiated by 190 KeV proton with the dosage of 10^{15} cm^{-2}. Normalized temperature dependent resistance under different magnetic field up to 9 T, applied perpendicular to the film surface, is shown in Fig. 3.14.

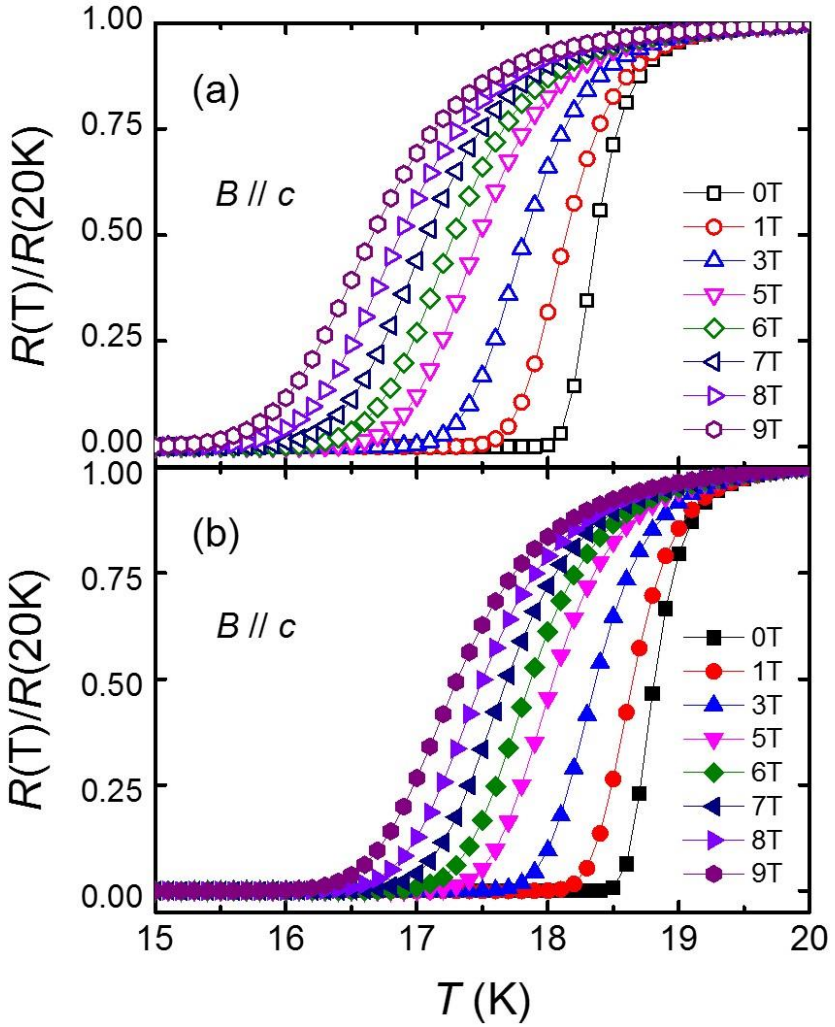

Figure 3.14 Normalized temperature dependent resistance under different magnetic field, up to 9 T perpendicular to the film surface, of the FST film before (a) and after (b) 190 keV proton irradiation at the dosage of 1×10^{15} cm^{-2}. Zero resistance T_c is enhanced by 0.5 K at zero field.

A general T_c enhancement is seen in the irradiated FST film. Under zero field, T_c^0 of the film was 18.0 K before irradiation, and was enhanced by 0.5 K after irradiation. The in-field T_c^0 enhancement is even larger as field increases: at 9 T, the T_c^0 enhancement is about 1 K. T_c^{onset} was also enhanced but with a smaller magnitude.

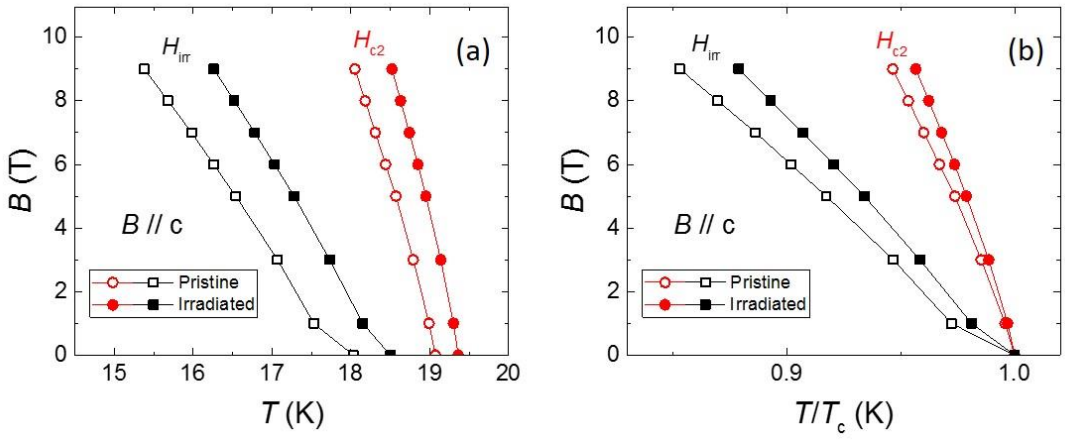

Figure 3.15 Irreversibility field H_{irr} and upper critical field H_{c2} before and after irradiation, plotted as the function of absolute temperature (a) and the temperature normalized by T_c (b), under the field applied perpendicular to the film surface. Error bars are of the size smaller than the data points. Larger enhancement is observed in H_{irr}.

Irreversibility field H_{irr} and upper critical field H_{c2} as a function of temperature were extracted from Fig. 3.14. Both curves shift to higher temperature after the proton irradiation, as shown in Fig. 3.15a. To show the effect brought by the enhancement in T_c, the critical field curves are replotted as the function of T/T_c for a clear view in Fig. 3.15b, where zero resistance T_c is used for H_{irr} and onset T_c is used for H_{c2}. The result shows enhancement effect on H_{irr} in irradiated sample. Though still can be observed, the improvement on H_{c2} is very small.

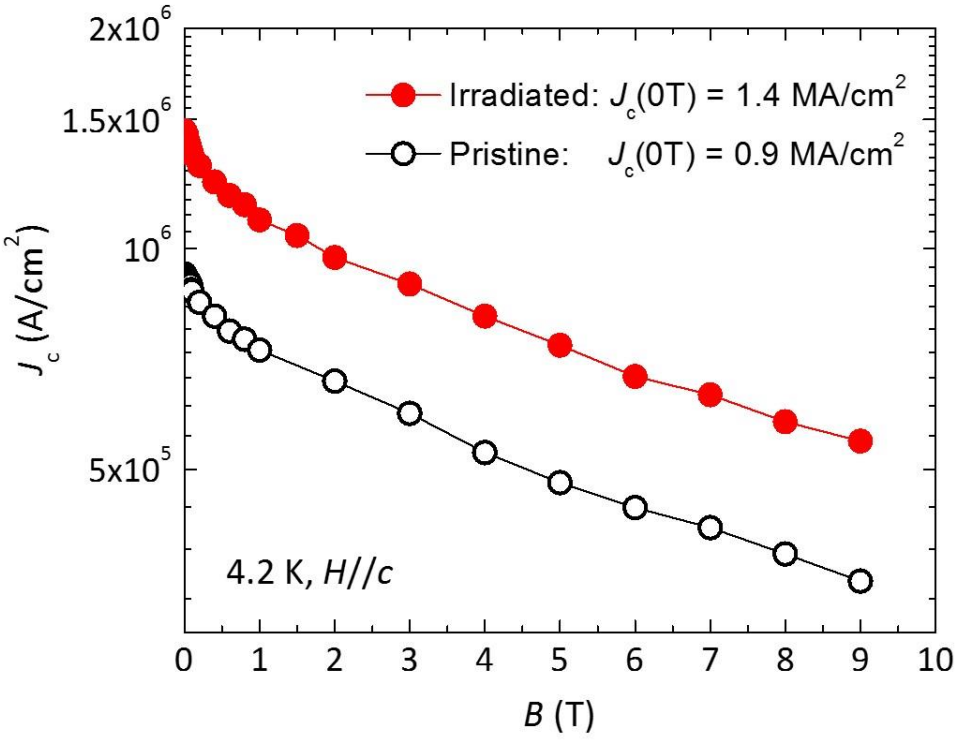

Figure 3.16 Transport J_c measured at 4.2 K before and after irradiation, as a function of magnetic field perpendicular to the film surface. The self-field J_c is enhanced by over 50%.

Figure 3.16 shows the transport J_c measured at 4.2 K before and after irradiation. An obvious enhancement is seen for the field range up to 9 T. Self-field J_c changed from 0.9 MA/cm^2 to 1.4 MA/cm^2, an enhancement more than 50%. After irradiation, the film has a J_c above 0.5 MA/cm^2 even under 9 T field, more than doubled that of the pristine film. The result suggests stronger vortex pining in the sample after irradiation.

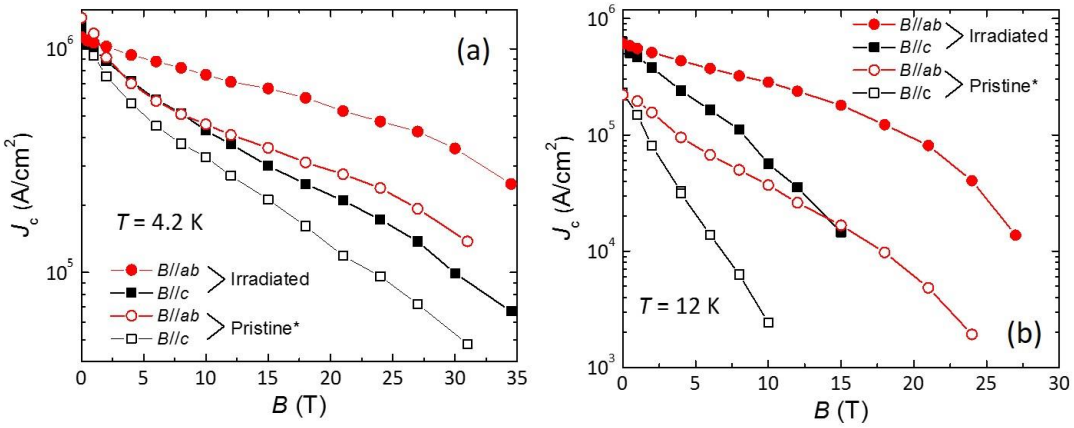

Figure 3.17 J_c in proton irradiated $FeSe_{0.5}Te_{0.5}$ film under the field up to 34.5 T, compared with the pristine film[18] at 4.2 K (a) and 12 K (b). Larger enhancement can be observed under higher field and at higher temperature.

Transport measurement of the irradiated FST film was performed under high magnetic field up to 34.5 T. Field dependent J_c in the irradiated FST film at 4.2 K and 12 K are plotted in Fig. 3.17, together with the data of the pristine film from Ref. 18 for comparison. The irradiated FST film clearly has a much better in-field performance for both field directions after irradiation, J_c at 12 K increased by one order of magnitude above 15 T for *B*//*ab* and above 6 T for *B*//*c*. Enhancement of vortex pinning at 12 K is much more significant compared to that at low temperature of 4.2 K.

3.4 Discussion and conclusion

Systematic transport studies were performed on FST films epitaxially grown on single crystal substrates with CeO_2 buffer layers. These films exhibit the zero resistance T_c at 18 K and the self-field J_c around 1 MA/cm^2. The upper critical field at zero temperature, $H_{c2}(0)$, can be estimated by using the Werthamer-Helfand-Hohenberg

approximation[106,107], $H_{c2}(0) = 0.7T_c |dH_{c2}/dT|_{T=T_c}$, yielding 112 T for $B//c$ and 208 T for $B//ab$. The field anisotropy is ~2. The J_c in these films can still be much enhanced by using the two methods described in this dissertation.

The oxygen annealing leads to a remarkable J_c enhancement, though slightly suppress the T_c. The reason for the J_c enhancement is likely to be the removal of excess Fe in the film. For $FeSe_xTe_{1-x}$ system, excess iron is almost unavoidable during the synthesis process. As was described in Chapter 1, magnetic moment in excess Fe will act as a pair breaker and severely damage the superconductivity. After annealing, the excess Fe is expected to be in the form of oxides. These iron oxides may still stay in the film and act as defects, but no longer provide the magnetic moment which is detrimental to superconductivity. In the experiment conducted for FST thin films, the intrinsic high J_c in FST thin films can be further improved to 2.54 MA/cm^2 (under self-field at 5 K) after 4 steps of oxygen annealing. Vacuum annealing also shows some enhancing effect, but the J_c enhancement is clearly much lower than that of oxygen annealed ones. The comparison of J_c enhancement between two different annealing experiments suggests the important role played by oxygen. This is in line with the result of the additional oxygen annealing on fully vacuum annealed films, where a large J_c enhancement exhibits. The saturation of J_c enhancement is observed in the last step of annealing which only shows very limited effect. It indicates that the enhancement by the process of excess Fe removal reaches the maximum effect after annealed for a few hours. The J_c enhancement observed in FST films is consistent with the study on single

crystal iron chalcogenides, where an enhanced self-field J_c up to 0.5 MA/cm^2 at 2 K was reported in $FeSe_{0.4}Te_{0.6}$ single crystals after oxygen annealing[94].

Long term aging experiment illustrates the relation between the J_c enhancement and the presence of oxygen from another angle. As-grown films clearly shows the J_c enhancement after 1-year aging in the air. It qualitatively has the same enhancing effect with the oxygen annealing, though with a less enhancement ratio. During the aging, excess Fe is slowly reacting with the oxygen in the air at the room temperature. In this scenario, it is not surprising to see no J_c change caused by aging in fully oxygen annealed films, in which the excess Fe had already been reacted previously. It is reasonable to conclude that the aging and oxygen annealing are based on the same mechanism by removing the excess Fe in the films, with the different reacting rate. The highest self-field J_c can reach up to 2.94 MA/cm^2 at 5 K in fully oxygen annealed FST films. It is not only the highest among the FST materials ever reported, but also comparable to that of "122" system which is more toxic and harder to synthesize.

Unlike the result showing an enhanced T_c in single crystal samples, T_c in FST films are suppressed, though not much, after oxygen annealing. It is found that during both annealing process, with or without oxygen, the T_c gradually decreases and the transition becomes sharper. One possible explanation is provided below.

The fast cooling process after FST film synthesis causes the inhomogeneity in the film and creates imbalanced local strain. It has been studied by E. Bellingeri *et al* that the compressive strain in *ab*-plane can enhance the T_c of FST films, and the in-plane lattice parameter is approximately linear-proportional to T_c.[43,44] In this scenario, the

inhomogeneity in the film would lead to a distribution of the strain field and hence T_c. The film comprises of high T_c regions with compressive strain and low T_c regions with tensile strain. The inhomogeneity in the as-grown films results in a relatively wider superconducting transition. One of the consequences of the sequential annealing, either in oxygen or vacuum, is to release the strain in the FST films, leading to a more homogenous strain distribution. This is consistent with the sharper superconducting transition and slightly lowered onset magnetization T_c observed in the annealed samples.

This 90 °C low temperature oxygen annealing is a simple and cost-efficient way to enhance the J_c for FST films after growth. Actually this annealing process can be further developed to an *in situ* process as a direct post-growth annealing. After carefully optimizing the conditions and the procedures, it can simplify the process for synthesizing high quality FST films with a much enhanced J_c.

Proton irradiation enhances J_c in another way – introducing defects which can act as pining centers to pin the vortices. As the experiment result shows, 190 KeV proton at the dosage of 10^{15} cm^{-2} can effectively enhance the J_c in FST film. J_c enhancement is about 50% under low field and much larger under high field, showing remarkable strengthened vortex pinning. Due to the enhanced pinning, H_{irr} and H_{c2} are also enhanced after irradiation, especially for H_{irr}, suggesting that the cascade defects are strong pining centers. More importantly, it is the first experiment to show a non-degraded T_c after irradiation meanwhile with the J_c enhancement. Actually the T_c can even be slightly enhanced.

It has been investigated in cuprates that irradiation induced cascade defects tend to become disordered in the depth where the incident ion energy is reduced to a very low value[60]. The disordered cascade defects observed in TEM imaging is consistent with the SRIM simulation: for low energy irradiation at 190 KeV, most of the protons were exhausted in the FST film and lose their last portion of energy before penetrating through. These disordered defects are likely responsible for the enhanced J_c at a proper density, by acting as effective pinning centers. On the other hand, films irradiated by 1 MeV were severely damaged with T_c suppressed below 10 K. According to the simulation, most of the ions with 1 MeV energy penetrate through the FST film and stop in the substrate in the irradiation. The experimental result shows that they are detrimental to the superconductivity in FST films. Choosing the appropriate ion energy is crucial to engineer the proper defect landscape.

Even with the same proton energy, there are still large differences between the samples irradiated under two different dosages. Two samples irradiated by 190 KeV, 10^{16} cm^{-2} protons have their T_c reduced to 13 K. Although with a less suppression compared to those irradiated by 1 MeV protons, the T_c is still lower than that of the bulk FST. It indicates that the density of defect is also very important. Calculation based on SRIM code shows that density of the collision are 5×10^{19} cm^{-3} and 5×10^{20} cm^{-3} caused by irradiation at the dosage of 10^{15} cm^{-2} and 10^{16} cm^{-2}, respectively, corresponding to an average distance between defects in *ab*-plane of ~3 nm and ~1 nm. The actual defect density observed in the cross-sectional view of the irradiated samples in TEM is lower than the simulation result. However, the defects created by 10^{16} cm^{-2}

protons might still be too much for the film, considering the in-plane coherence length of FST of 2~3 nm which is the size of the vortex core. These over-dense defects bring too much damage to the crystal structure and weaken the superconductivity.

Another question is why T_c can be enhanced after structural defects are introduced. A possible explanation can be provided based on the strain field observed surrounding the cascade defect described as below. Similar to the strain induced by the cooling process during synthesis, which has been discussed to cause the inhomogeneous T_c regions in the FST film, these irradiation-induced strain field can also alter the T_c in adjacent areas. High T_c and low T_c domains are formed due to the compressive and tensile strain. The difference is that these inhomogeneous domains caused by irradiation is much closer to each other, in a level of nanometers, compared to those of temperature induced ones. It makes large variation on the lattice constant in relatively small areas, leading to many local regions filled with entangled high T_c and low T_c domains. If the compressed high T_c domains are close enough, with the distance comparable to the coherence length of FST, the T_c will be enhanced in a larger area due to the proximity effect[19,108,109], where superconducting electrons can tunnel through. Hence the film would have an enhanced T_c and the self-field J_c.

The work of strain mapping and analysis through TEM imaging in irradiated FST films was done by our collaborator Dr. L. Wu. Figure 3.18a,d are the TEM image of a pristine film and an irradiated film, the later one contains cascade defects caused by irradiation. The pristine film has a uniform strain distribution for both in-plane ε_{xx} (Fig. 3.18b) and out-of-plane ε_{zz} (Fig. 3.18c). While the irradiated film shows an ε_{xx} with a

large spatial variation (Fig. 3.18e). The derived in-plane lattice parameter of the irradiated film is shown in Fig. 3.18g, varies from 3.7 Å to 3.9 Å. A 3D false-color image in Fig. 3.18h shows the spatial variation of T_c obtained by using the linear relation given by E. Bellingeri *et al.*[43,44]. High-T_c and low-T_c regions are linked in a network like a cobweb in the irradiated FST films, with the highest T_c reaching ~ 25 K and the lowest T_c reaching ~ 15 K. The enhanced T_c regions in the irradiated FST film rises from these contracted lattice parameter domains that are less than 5 nm apart on average. This is comparable to the in-plane coherence length of FST which is ~3 nm, allowing proximity effect to take into play. This result is consistent with the explanation that the T_c enhancement is due to the strain field caused by irradiation.

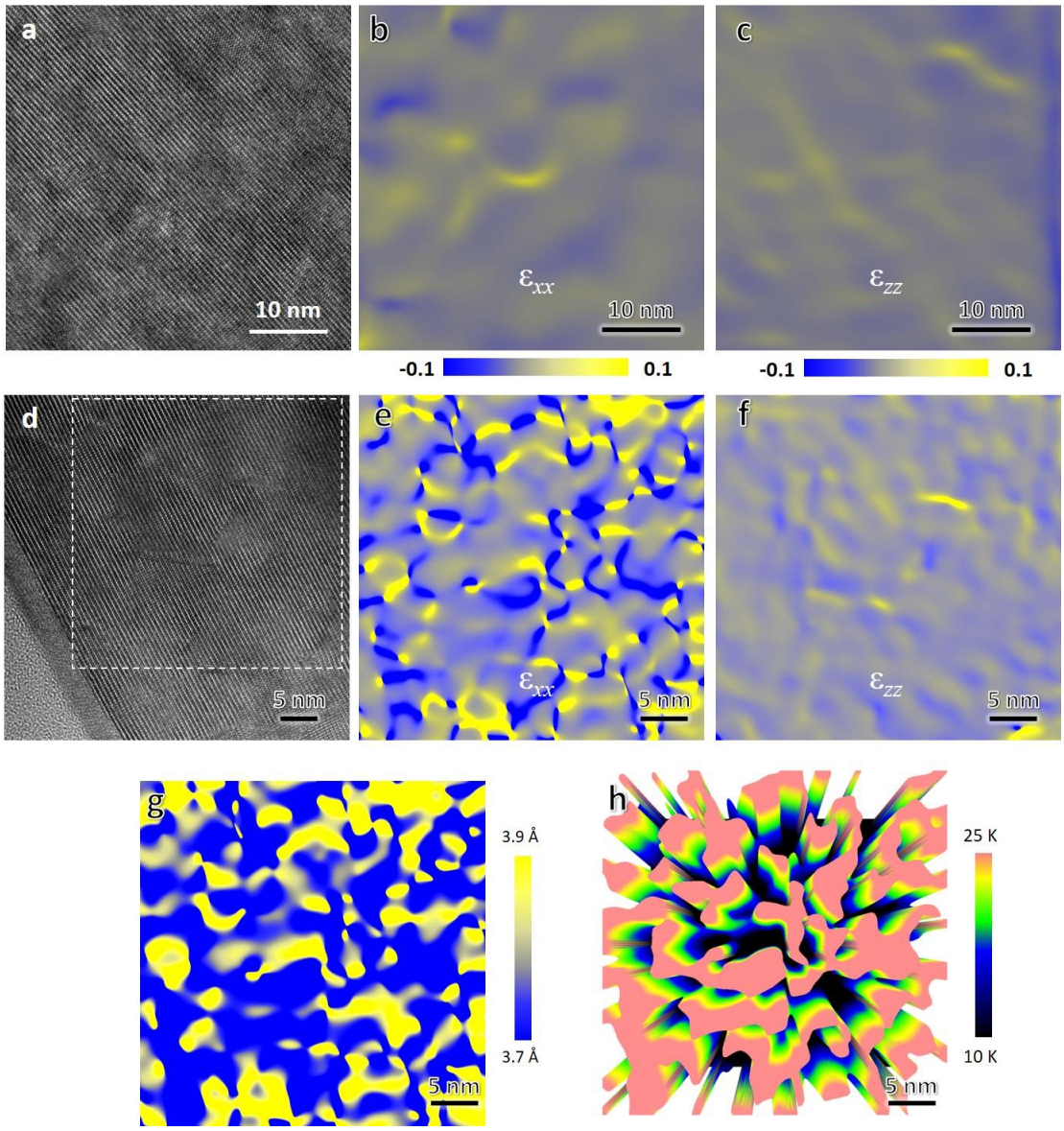

Figure 3.18 TEM image and strain analysis of a pristine and an irradiated $FeSe_{0.5}Te_{0.5}$ films. The pristine film (a) shows small strains which uniformly distributed on in-plane (b) and out-of-plane directions (c). Irradiated film (d) shows large strain variations on in-plane direction (e) and a similar out-of-plane strain distribution (f) to that of pristine one. The in-plane lattice parameter (g) and T_c (h) in the corresponding area can be converted from the in-plane strain distribution. Entangled high T_c and low T_c domains are shown in the irradiated film. The figure is adopted from Ref. 110.

It is interesting to have two methods, oxygen annealing and proton irradiation, with different mechanisms both enhancing J_c in FST films. Figure 3.19 compares the field dependent J_c (B//c) at 4.2 K for annealed FST film and irradiated FST film, along with the data of several other superconducting materials including 2G YBCO, NbSn and Nb-Ti, adopted from literatures[97,98,111-114]. It is seen that irradiated films show higher J_c under high field while annealed films perform better under low field. The irradiation-induced defects in the film can act as pining centers, resulted in larger pining forces and higher J_c under high field. While larger J_c enhancement in oxygen annealed film under low field mainly reflects the better intrinsic superconductivity, which is due to the mechanism of removing excess Fe. In-field J_c performance for both post-treated FST films is superior comparing to Nb-Ti. Even compared to Nb_3Sn, which once held the high field J_c record among the non-cuprate superconductors, J_c in irradiated FST films still dominates under the field above 8 T, though still lower than 2G YBCO wires.

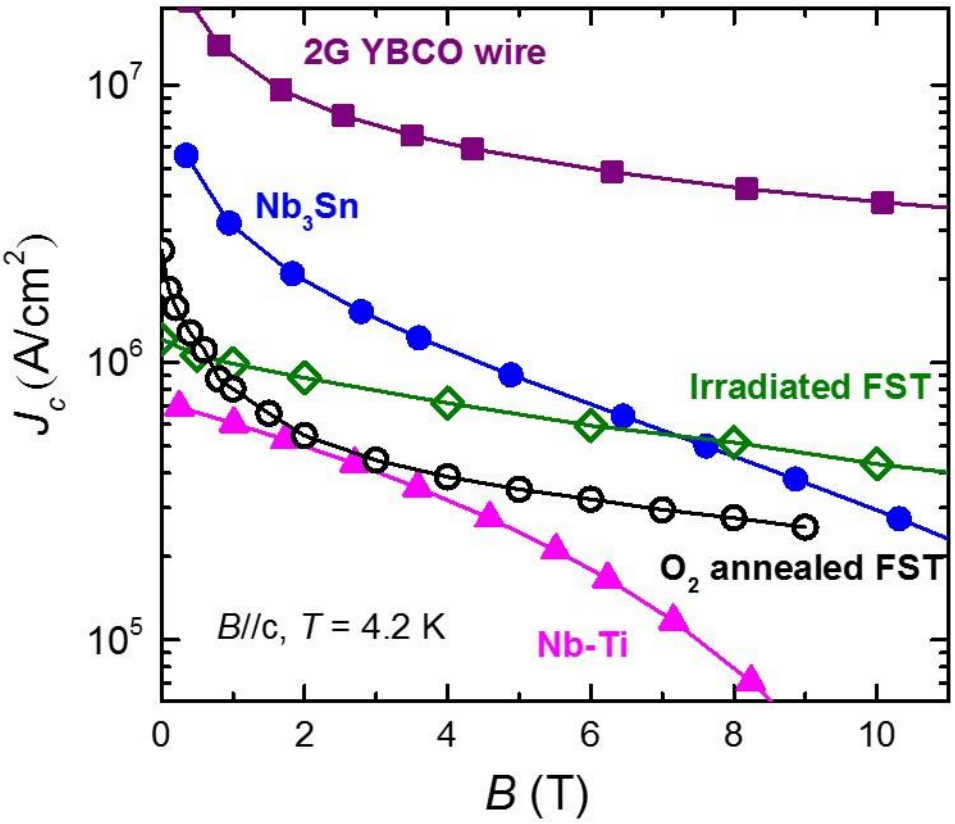

Figure 3.19 Comparison of the in-field J_c between oxygen annealed and the proton irradiated $FeSe_{0.5}Te_{0.5}$ films, along with several other superconducting materials. Annealed film shows higher J_c under low field and irradiated film shows higher J_c under high field. Data of YBCO, NbSn and NbTi are adopted from literatures.[97,98,111-114]

The post-treated FST films are promising for future practical high field applications at liquid helium temperature on the cost-effective bases. Note the production of FST films only needs ~ 400 ℃, far lower than that of YBCO films synthesis (>700 ℃). Limited oxidation of the metal substrate is expected at this much reduced processing temperature. It means thinner and less complicate textured buffer layers will be needed and the cost will be much lower. FST has been successfully grown

on RABiTS through PLD[18], with the enhanced high field J_c. If combined with the post-treatment methods in this dissertation, the iron chalcogenide coated conductors with superior in-field J_c performance can be expected in near future.

In summary, FST thin films were synthesized by PLD technique under optimized conditions with zero resistance T_c at 18 K and remarkably high J_c. At the temperature of 5 K, the J_c is approximately 1 MA/cm^2 at self-field and 0.2 MA/cm^2 at 3 T. The J_c of the films can be further enhanced by post-treatment methods. This study provides two practical ways: oxygen annealing and proton irradiation. Low temperature oxygen annealing is a simple and cost-efficient way to enhance the J_c by removing the excess Fe after growth which can double the self-field J_c. Low energy proton irradiation is also a practical method which can significantly enhance the high field J_c without T_c suppression by introducing cascade defects as pining centers.

FST materials have the simplest structure and the least toxicity in iron-based superconductors. Being properly treated after growth, these high quality FST films exhibit extraordinary high J_c which is comparable to that of iron pnictides, and thus become more promising for the next generation high field superconductors at liquid helium temperature. It would be interesting to further explore and optimize the combination of these post-treatment techniques, which may achieve an even better superconducting performance in this material.

4. Transport Properties of $YB_2C_3O_{7-\delta}$ Coated Conductors upon Gold Ion Irradiation and Post-annealing

4.1 T_c and J_c change in YBCO tapes after gold ion irradiation

22 MeV gold irradiation was performed on YBCO coated conductors at different dosages, as was described in Chapter 2. Magnetization measurement was conducted on pristine and irradiated YBCO tapes in order to investigate the influence in T_c and J_c. Preliminary measurements showed that films irradiated by 1×10^{12} cm^{-2} and 2×10^{12} cm^{-2} ions were heavily damaged with the T_c close to or lower than 77 K, the temperature of liquid nitrogen. On the other end, films irradiated by 8×10^{10} cm^{-2} ions exhibit little change on both T_c and J_c due to the low influence. Detailed measurement result of samples irradiated under the dosage of 1×10^{11} cm^{-2}, 2×10^{11} cm^{-2}, 4×10^{11} cm^{-2}, 6×10^{11} cm^{-2} and 8×10^{11} cm^{-2} are shown in this chapter. For a simple and clear view, these samples are labelled as 1E11, 2E11, 4E11, 6E11 and 8E11, respectively. The reference data, labelled as "Ref" were averaged from three unirradiated samples. All magnetic field applied on samples were along the *c*-axis.

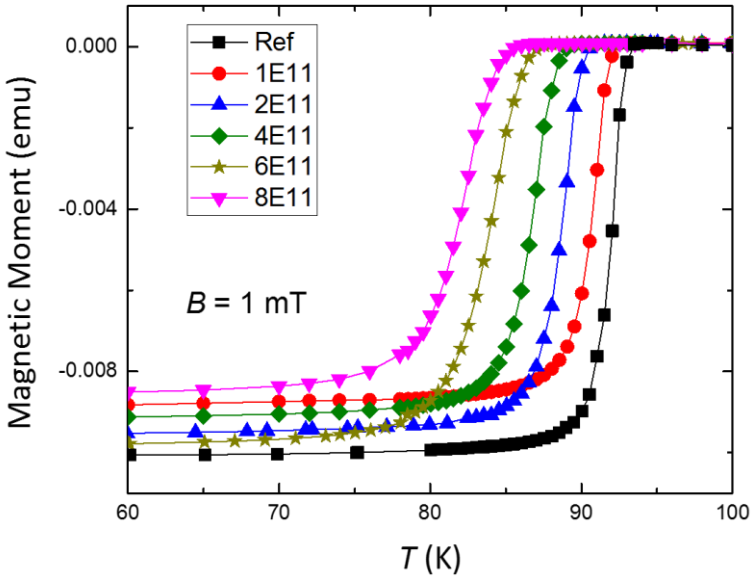

Figure 4.1 Superconducting transition of irradiated samples and the reference sample. The T_c is suppressed in irradiated samples and the suppression is larger at higher dosages.

The result of magnetic moment as a function of temperature is shown in Fig. 4.1, measured under an external field of 1 mT. T_cs of the irradiated samples are all degraded, and the magnitude of the degradation increases with the rising dosage. The value of T_c is 93.5 K in unirradiated samples, and shows as 85.5 K in the 8E11 sample, with a suppression of 8 K. T_c in 1E11 sample is 92.2 K, showing the smallest T_c degradation of 1.3 K (details can be found in Table 4.1). The trend of this T_c degradation upon the irradiation dosage was expected, which reflects the damage brought into the materials by the gold ions.

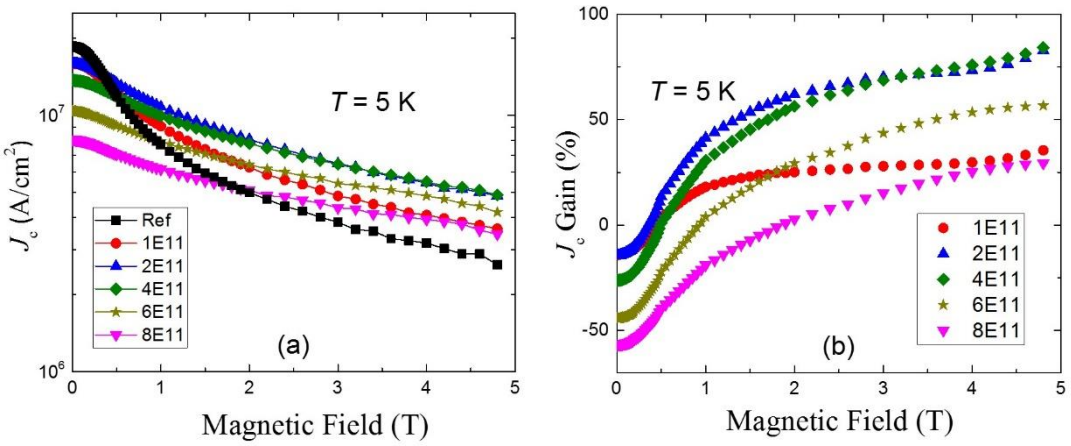

Figure 4.2 Field dependent J_c (a) and J_c enhancement (b) at 5 K in the samples irradiated at different dosages. Self-field J_c are suppressed while high field J_c are enhanced.

Figure 4.2a shows the field dependent J_c at 5 K in the samples after irradiation, as well as that in the reference sample, derived from the *MH* loop using the Bean model described in Chapter 2. The reference sample holds a self-field J_c of 18.6 MA/cm^2, whose in-field J_c rapidly decreases as the magnetic field increases. After the irradiation, all samples show degraded self-field J_c and the degradation generally grow larger as a function of rising ion dosage. The smallest degradation shows in the 1E11 and 2E11 samples, where self-field J_c yields 16 MA/cm^2. On the other hand, the in-field J_c shows large enhancement. Above 1 T external field, J_c in most of the irradiated samples begins showing a higher value compare to that of the reference sample, except for J_c in the 8E11 sample which starts showing enhancement under higher field above 2 T. The most prominent enhancement is observed in the 2E11 and 4E11 samples, with their J_c around 6.4 MA/cm^2 at 3 T and 4.8 MA/cm^2 at 4.8 T. These two samples show almost identical J_c (B) curves under the field above 2.5 T, though with different self-field J_c.

The 1E11 sample shows the lease self-field J_c suppression compare to other irradiated samples, but a relatively lower high field J_c.

The J_c enhancement at 5 K, calculated as $J_c^{gain} = J_c^{irradiated} / J_c^{ref} - 1$, for samples after irradiation is plotted in Fig. 4.2b. For the 2E11 and 4E11 samples, J_c^{gain} above 2.5 T is at the level of 70% ~ 90% which is the highest among all irradiated samples. The 6E11 sample also shows a relatively large J_c enhancement of almost 50% under high field. J_c^{gain} curves for the 1E11 and 8E11 samples are approaching to each other as the field increases. Both of them yield ~30% at 4.8 T, though having the largest difference at 0 T.

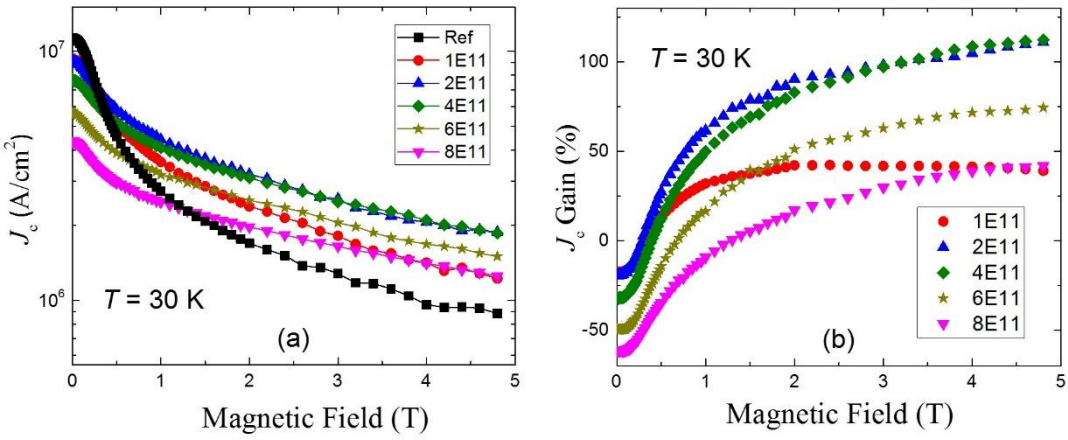

Figure 4.3 Field dependent J_c (a) and J_c enhancement (b) at 30 K in the samples irradiated at different dosages. Self-field J_c are suppressed while high field J_c are enhanced.

J_c in the irradiated samples and the corresponding J_c enhancement at 30 K are plotted in Fig 4.3. J_c of the reference sample is over 1.1 MA/cm^2 at 0 T and quickly drops as the field ramping up. Self-field J_c in irradiated samples shows the same dosage

dependent degradation profile as that of measured at 5 K. The smallest self-field J_c suppression shows in the 1E11 and 2E11 samples, and the largest suppression shows in the 8E11 sample. Compared to that of 5 K, the in-field J_c shows earlier crossover points at 30 K for all dosages: The J_c enhancement starts to show at the field of 0.4 T for the 1E11, 2E11 and 4E11 samples. Even for the 8E11 sample, J_c becomes higher than that of reference sample under the field above 1.2 T.

The highest J_c enhancement at 30 K under high field shows in the 2E11 and 4E11 samples, at a level of 90% ~ 120% above 2.5 T. Under this field range, J_c in the 6E11 sample has an enhancement around 60%. Like the behavior at 5 K, the 1E11 and 8E11 samples show a large difference in self-field J_c, but yield similar enhancement of about 40% under the field above 3T. The average J_c enhancement at 30 K is higher than that of at 5 K.

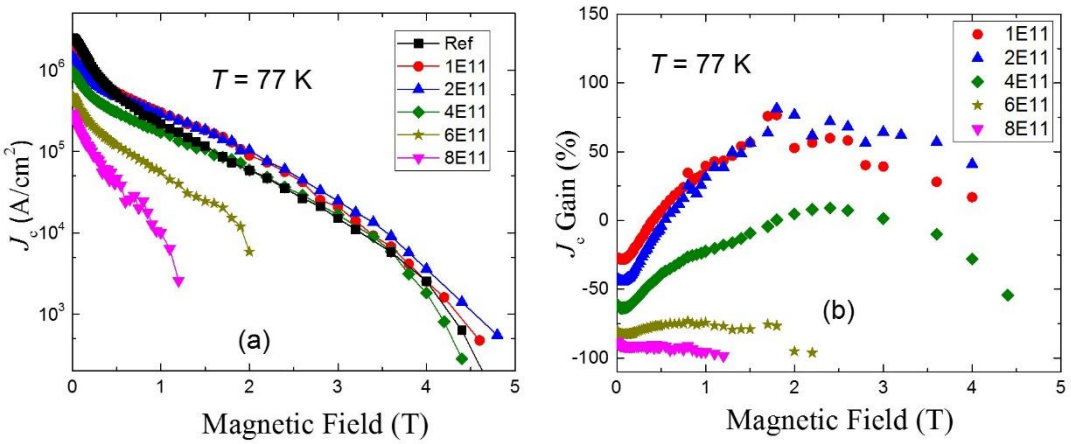

Figure 4.4 Field dependent J_c (a) and J_c enhancement (b) at 77 K in the samples irradiated at different dosages. J_c in heavily irradiated samples crashes under a rather low field. Enhancement only shown in 1E11 and 2E11 samples.

The same measurement was performed at 77 K and the result is plotted in Fig. 4.4. Unlike what was found at 5 K and 30 K, where all the field dependent J_c curves display a slower decay under high field, J_c at 77 K in the reference sample shows a rapid crush when field ramps above 3 T. It is likely resulted from that the applied field is close to the irreversible field at this temperature. J_c in irradiated samples also shows similar rapid decay. With the increasing field above 3 T, J_c in the 1E11, 2E11 and 4E11 samples goes down very quickly. J_c in the 6E11 and 8E11 samples start to crush at even lower fields of 2 T and 1 T, respectively. It is reasonable since the T_c degradation is larger in samples irradiated under higher dosage.

The J_c enhancement can still be seen in the 1E11 and 2E11 samples under the field above 0.5 T. For the 6E11 and 8E11 samples, J_c is totally suppressed in all measured field range. For the 4E11 sample, the J_c is mostly suppressed and the enhancement is only observed in the field range between 2 T and 3.5 T.

Table 4.1 lists detailed measurement result for the irradiation experiment. The discussion of the structure and the superconducting properties will be presented later in Section 4.3.

		Ref	1E11	2E11	4E11	6E11	8E11
T_c^M		93.5	92.2	90.7	88.5	87	85.5
ΔT_c^M		N/A	-1.3	-2.8	-5	-6.5	-8
5K	J_c (0T)	18.6	16.0	16.0	13.7	10.4	8.08
	J_c^{gain} (0T)	N/A	-14%	-14%	-26%	-44%	-57%
	J_c (3T)	3.82	4.85	6.48	6.44	5.42	4.36
	J_c^{gain} (3T)	N/A	26%	70%	69%	42%	14%
30K	J_c (0T)	11.3	9.33	9.21	7.69	5.66	4.35
	J_c^{gain} (0T)	N/A	-17%	-18%	-32%	-50%	-61%
	J_c (3T)	1.28	1.81	2.54	2.52	2.05	1.64
	J_c^{gain} (3T)	N/A	42%	98%	97%	60%	29%
77K	J_c (0T)	2.50	1.82	1.45	0.98	0.50	0.29
	J_c^{gain} (0T)	N/A	-27%	-42%	-61%	-80%	-88%
	J_c (3T)	0.0150	0.0207	0.0246	0.0206	N/A	N/A
	J_c^{gain} (3T)	N/A	39%	64%	37%	N/A	N/A

T_c^M and ΔT_c^M are shown in the unit of Kelvin, J_c is shown in the unit of MA/cm^2.

Table 4.1 Detailed magnetization measurement result of $YBa_2Cu_3O_{7-\delta}$ irradiation experiment.

4.2 Post-annealing effect on irradiated YBCO tapes

Two steps of oxygen annealing were conducted under the condition described in Chapter 2. Three samples – 2E11, 4E11 and 6E11 which consist comparatively higher J_c and T_c among all the irradiated samples – were involved in this annealing experiment. The result is shown separately for each sample, comparing the T_c and J_c at each step of annealing. “a1” and “a2” stands for the result measured after the first and the second step of oxygen annealing.

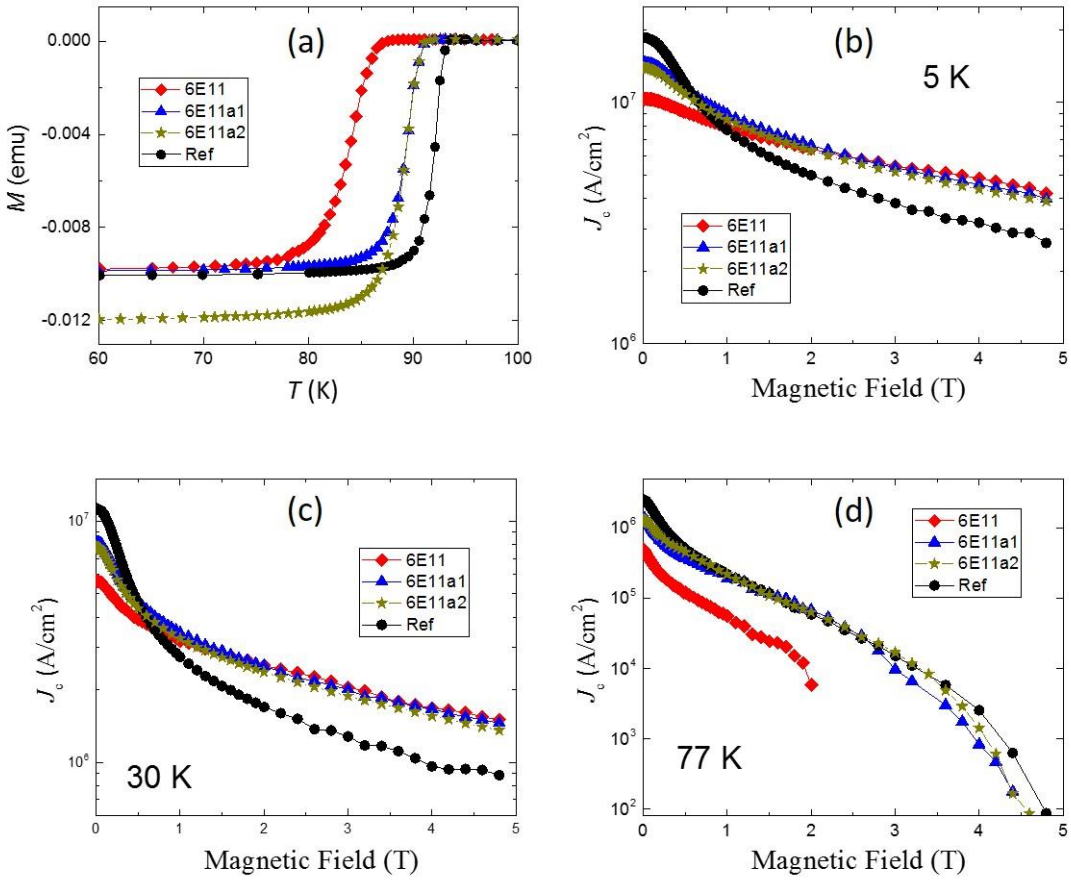

Figure 4.5 Post-annealing effect on T_c (a) and field dependent J_c at 5 K (b), 30 K (c) and 77 K (d) in the sample irradiated by 6×10^{11} cm^{-2} ions, derived from magnetic measurement result. J_c at 77 K is almost fully recovered.

Figure 4.5 shows the T_c and field dependent J_c derived from magnetization measurement for the 6E11 sample before and after the post-annealing. Big changes was observed on the aspect of T_c: after the first oxygen annealing, T_c is partially recovered (solid triangles in Fig. 4.5a) from the degradation caused by irradiation, which goes up to 91.5 K. Considered the T_c dropping from 93.5 K to 87 K after irradiation, the annealing recovered almost 70% of the degradation. While the second annealing at a

higher temperature (solid stars) does not show any further change, indicating the saturation of the T_c recovering.

Self-field J_c was also partially recovered at all three measured temperatures after the first annealing. At 5 K, self-field J_c drops from 18.6 MA/cm^2 to 10.4 MA/cm^2 after irradiation, and is recovered to 14.6 MA/cm^2. Approximately half of the self-field J_c degradation is gained back. The recovering ratio in self-field J_c are at the same level, yielding 45% at 30 K and 44% at 77 K.

However, high-field J_c at 5 K and 30 K is slightly suppressed after annealing. The suppression started to show at the field of 2.5 T. An average degradation of 4% is observed at 5 K and 30 K, within the field range from 2.5 T to 4.8 T. Note that even being suppressed, the in-field J_c at 5 K and 30 K is still much higher than that of unirradiated sample. At 77 K, the annealing seems to bring back the in-field J_c, which was severely suppressed after irradiation. If compared to the reference sample at 77 K, no promising change of the in-field J_c can be found in the post-annealed sample.

The second step of annealing seems to make no obvious further change on the aspect of J_c. At all three measured temperatures, field dependent J_c shows a small variation of 5% after the second annealing. Most of the changes in J_c caused by the second annealing are suppressions, except for certain field ranges (0.2 ~ 1 T, 3 ~ 4.2 T) at 77 K.

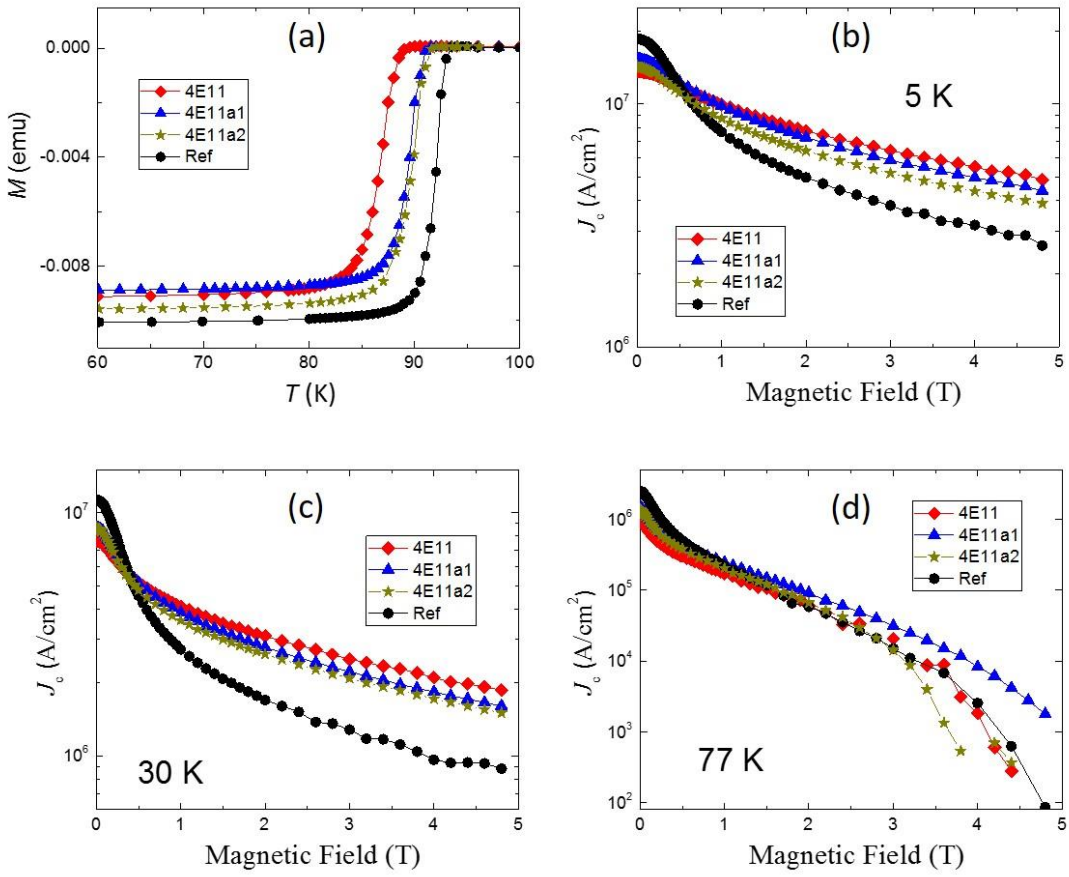

Figure 4.6 Post-annealing effect on T_c (a) and field dependent J_c at 5 K (b), 30 K (c) and 77 K (d) in the sample irradiated by 4×10^{11} cm^{-2} ions, derived from magnetic measurement result.

Figure 4.6 shows the magnetization measurement result of the 4E11 sample before and after two steps of the post oxygen annealing. Similar to that of the 6E11 sample, T_c in the 4E11 sample is partially recovered from the degradation caused by irradiation, going up to 91 K after the first annealing. Compared to the T_c dropping from 93.5 K to 88.5 K after irradiation, the annealing recovers half of the degradation. Self-field J_c has also been partially recovered by annealing, with the ratio of 44%, 27% and 31% at 5 K, 30 K and 77 K, respectively.

At 5 K and 30 K, J_c is suppressed after the first annealing under the field above 0.5 T. Within the field range between 2.5 T and 4.8 T, the J_c suppression is at the level of 10%, larger than that of annealed 6E11 sample. Though suppressed by annealing, in-field J_c under this field range is still higher than unirradiated sample. The result at 77 K turns different way, where the annealed sample shows an enhanced in-field J_c under the field above 1 T. Note this enhanced in-field J_c due to annealing was higher than that of either the reference sample or the irradiated sample, which was not found in the 6E11 sample. The enhancement is larger as the field increases, yields by the factor of 3 compare to reference sample under 3 T. Though the enhancement seems even greater above 3 T, it is less meaningful to compare the exact value due to the rapid J_c dropping in the reference sample. However, it is clearly seen that the annealing indeed slows down the high field J_c dropping at 77 K.

After the second step of annealing, T_c was further recovered by 0.5 K. On the other hand, both self-field J_c and in-field J_c has been suppressed at all three measured temperatures compare to that of 4E11a.

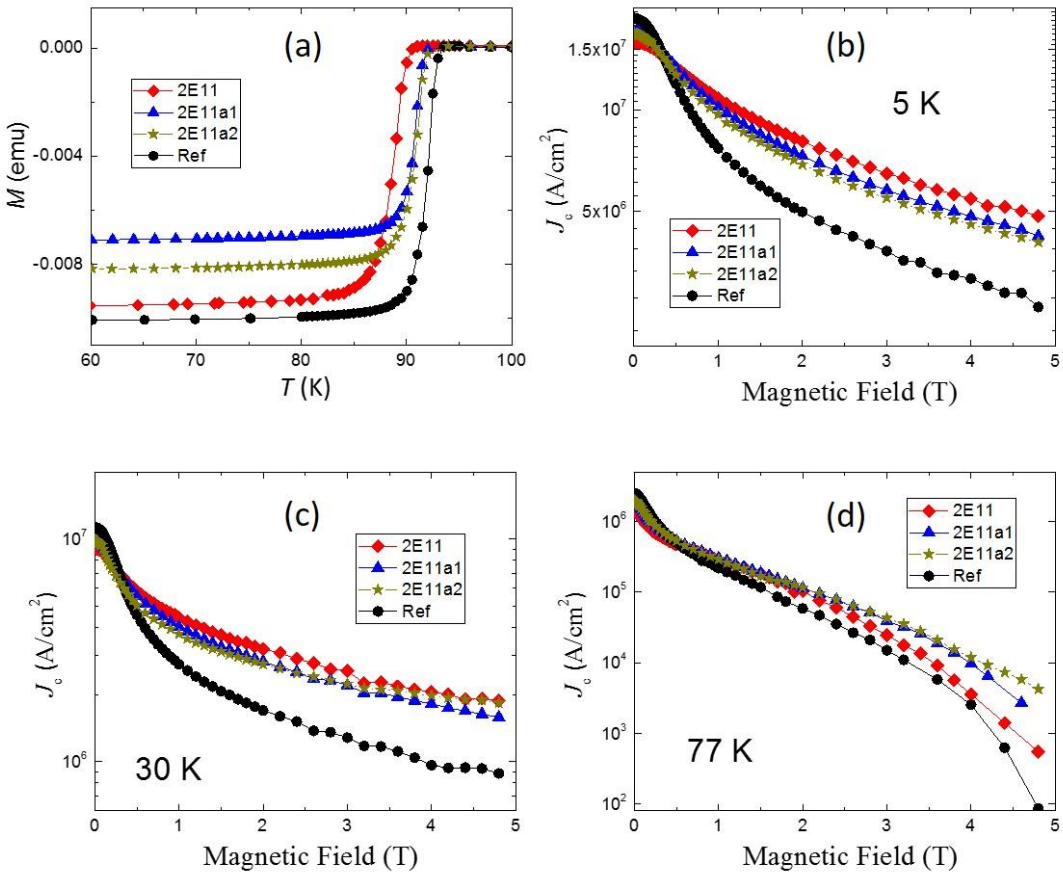

Figure 4.7 Post-annealing effect on T_c (a) and field dependent J_c at 5 K (b), 30 K (c) and 77 K (d) in the sample irradiated by 2×10^{11} cm^{-2} ions, derived from magnetic measurement result. Further J_c enhancement is shown at 77 K.

Figure 4.7 shows the T_c and field dependent J_c derived from the magnetization measurement result for the 2E11 sample before and after the oxygen annealing. Similar to that of 6E11 and 4E11 samples, T_c in 2E11 sample is partially recovered to 92.5 K after the first annealing. Though it is only 1.8 K in absolute value, the recovery is still promising given that the total T_c degradation in the 2E11 sample caused by irradiation was only 2.8 K. Self-field J_c has also been partially recovered by annealing, with the ratio of 36%, 28% and 38% at 5 K, 30 K and 77 K, respectively.

Similar to that of in 4E11 sample, the oxygen annealing after the irradiation gives a negative influence to 2E11 sample on the aspect of in-field J_c at 5 K and 30 K, under the field above 0.5 T. After the first annealing, the J_c enhancement under 3 T field compare to reference sample was reduced from 70% to 50% and from 100% to 70% at 5 K and 30 K, respectively. While, a clear positive influence is observed at 77 K, where the annealed 2E11 sample holds a higher J_c at all measured field. It is the further enhancement upon the irradiation which already had the J_c enhanced under the field above 0.5 T. The enhancement turns larger under higher field: at 3T, the 64% J_c enhancement after irradiation is further boosted to 158% after annealing. The J_c decay at 77 K under high field becomes slower in annealed sample and the enhancement is much more obvious above 3 T.

The second step annealing still further recovers the T_c in a detectable manner, thought the absolute T_c change is less than 0.2 K. On the aspect of in-field J_c, the second annealing doesn't show a clear positive result at 5 K and 30 K. However, at 77 K, J_c is further enhanced under the field higher than 2.5 T, which was not found in 4E11 and 6E11 after the second annealing.

Table 4.2 lists the detailed magnetization measurement result of post-annealing experiment on irradiated YBCO tapes.

		2E11			4E11			6E11		
		*a*0	*a*1	*a*2	*a*0	*a*1	*a*2	*a*0	*a*1	*a*2
T_c^M		90.7	92.5	92.6	88.5	91	91.5	87	91.5	91.5
ΔT_c^M		-2.8	-1	-1	-5	-2.5	-2	-6.5	-2	-2
5K	J_c (0T)	16.0	16.9	16.8	13.7	15.2	14.3	10.4	14.6	14.0
	J_c^{gain} (0T)	-14%	-9%	-9%	-26%	-18%	-23%	-44%	-22%	-25%
	J_c (3T)	6.48	5.79	5.49	6.44	5.88	5.20	5.32	5.37	5.15
	J_c^{gain} (3T)	70%	52%	44%	69%	54%	36%	39%	41%	35%
30K	J_c (0T)	9.21	9.80	9.90	7.69	8.63	8.69	5.66	8.20	7.87
	J_c^{gain} (0T)	-18%	-13%	-12%	-32%	-24%	-23%	-50%	-27%	-30%
	J_c (3T)	2.55	2.20	2.21	2.49	2.21	2.08	2.05	2.01	1.88
	J_c^{gain} (3T)	99%	72%	73%	94%	73%	63%	60%	57%	47%
77K	J_c (0T)	1.45	1.85	1.95	0.98	1.45	1.36	0.50	1.38	1.29
	J_c^{gain} (0T)	-42%	-26%	-22%	-61%	-42%	-46%	-80%	-45%	-48%
	J_c (3T)	0.0246	0.0387	0.0426	0.0206	0.0312	0.0304	N/A	0.0087	0.0168
	J_c^{gain} (3T)	64%	158%	184%	37%	108%	103%	N/A	-42%	12%

T_c^M and ΔT_c^M are in the unit of Kelvin, J_c is in the unit of MA/cm^2. All changes are the comparison to the unirradiated reference sample.

Table 4.2 Detailed magnetization measurement result of post annealing experiment on irradiated $YBa_2Cu_3O_{7-\delta}$ tapes.

4.3 Discussion and conclusion

The production of 2G coated conductors has been well established. Samples used in the experiment were produced at the optimized condition with the high T_c at 93.5 K. During the ion irradiation, collisions happen to the nuclei of the YBCO atoms and push them away from the original places. Thus structural defects can be created and act as the pinning centers to improve the in-field J_c. Accompanied T_c and self-field J_c suppression also shows as a side effect, due to the damage in the original crystal structure. It is in line with the result that larger degradation of T_c and self-field J_c is

found in samples irradiated by higher dosage of ions. This irradiation-induced suppression has been found in many previous reports[51-53,56,57].

In the study, all measured samples show enhanced J_c under high field (> 2 T) at 5 K and 30 K, with different enhancement rate. The J_c enhancement at 30 K is higher than that at 5 K. At 77 K, J_c enhancement is only observed in the 1E11 and 2E11 samples, while samples irradiated under high dosages has severe J_c suppressions. This is likely due to the T_c suppression caused by irradiation. When at lower temperatures, the in-field J_c performance is not likely affected by the T_c suppression, since the suppressed T_c is still much higher than 5 K or 30 K. However, at 77 K which is close to the degraded T_c in heavily irradiated samples, the pairing is weakened and the superconductivity can be significantly suppressed under a rather low magnetic field. Thus it is not surprising to see the early crash of the in-field J_c, even with the pining centers introduced.

According to the experiment result, the optimum dosage for the 22 MeV gold ion irradiation, considering overall performance, is 2×10^{11} cm^{-2}. At this dosage the T_c degradation is 2.8 K and the in-field J_c enhancement is on the highest level at all three measured temperatures. 4×10^{11} cm^{-2} dosage irradiation also leads to a comparably high enhancement at 5 K and 30 K, but is not effective at 77 K due to the higher T_c suppression.

The SRIM simulation shows the defect density in 2E11 sample is 4.6×10^{19} cm^{-3}. The distance between the defects can be estimated at 3 nm, which is a little larger than the coherence length of YBCO in *ab*-plane (~2 nm). The coherence length is the size

of the normal state core of the vortex. If the defect density is too high, the pinning centers will be too close to each other where the vortices pinned on the nearest defects suffer from the expelling force. It is less effective and brings unnecessary damage to superconductivity. It is consistent with the observation that samples irradiated under the dosage higher than 4×10^{11} cm^{-2} exhibit less J_c enhancement. Optimizing the irradiation dosage is actually to achieve a proper defect density, balancing between the introduced pinning centers and the structural damage. When properly done, the irradiation does not harm the intrinsic superconductivity too much and meanwhile effectively pins the vortices to enhance the J_c at high field.

For a comprehensive understanding, structural characterization through TEM was conducted by our collaborator Dr. L. Wu, in order to investigate the landscape of the defects caused by incident Au^{5+} ions. Fig. 4.8a shows the cross-sectional TEM images for a YBCO sample irradiated by gold ions with 18 MeV energy at the dosage of 6×10^{11} cm^{-2}. The defects in these TEM samples are expected similar to that of 22 MeV irradiated ones discussed above, as simulated using SRIM. In Fig. 4.8a, the red arrow indicates the direction of the incident gold ion, white doted arrow indicates the *c*-axis of the YBCO sample and the yellow arrows point at the ripples with the length up to hundreds nanometers. They are actually splits between the atom layers, parallel distributed over the entire sample. Fig. 4.8b shows the TEM image for a pristine sample, where none of such defects is observed. The atom positions are indicated in the inset with red, blue and green filled circles, representing Y, Ba and Cu atoms, respectively. Enlarged images for one of the typical defects in irradiated film are shown in Fig.4.8c,d.

The splits are found between the Ba-O layers which is likely due to that large Ba atoms burden the most collisions during the irradiation. The split is of large width in the middle and gradually smears out on the side. The T_c and self-field J_c suppression observed in irradiated samples are resulted from the structural damage caused by these defects. On the other hand, they also act as pinning centers to pin the vortex and are responsible for the J_c enhancement under higher field.

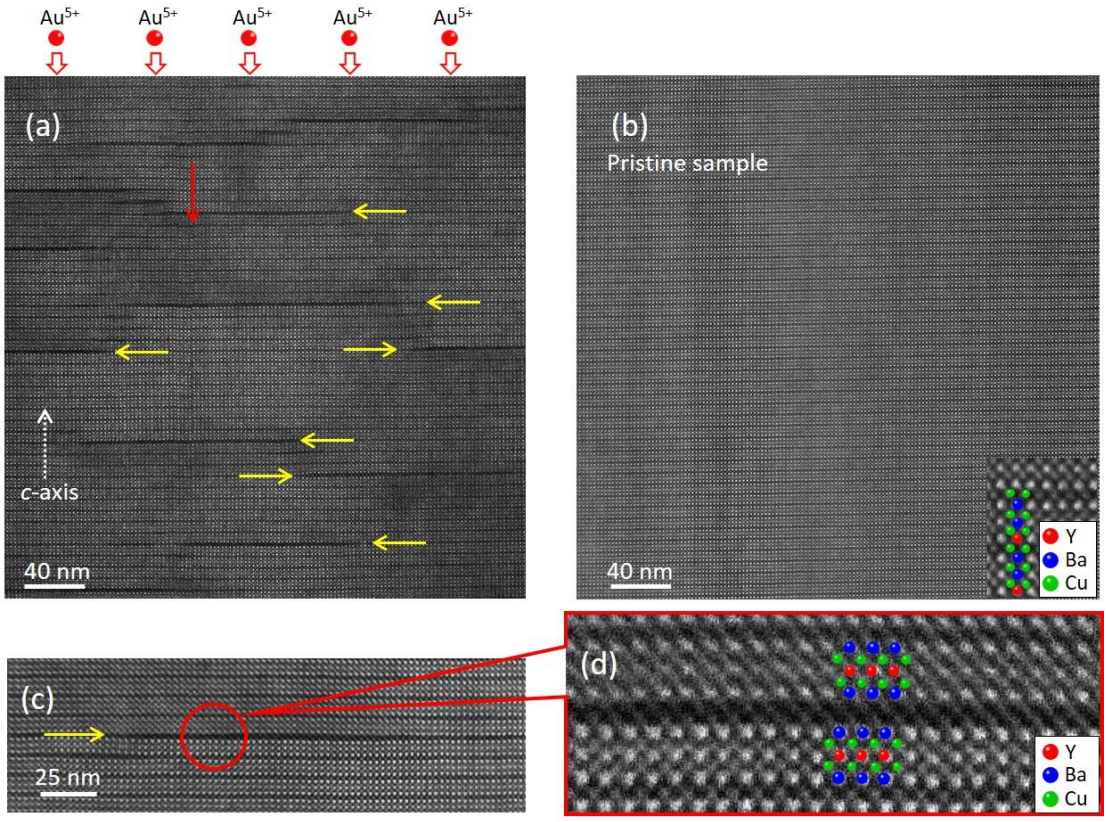

Figure 4.8 Cross-sectional TEM image of a gold ion irradiated (a) and a pristine (b) $YBa_2Cu_3O_{7-\delta}$ coated conductors. Inset in (b) is an enlarged image in the pristine sample and the atom positions are indicated. Enlarged images for a typical defect in the irradiated sample are shown in (c) and (d). Splits between Ba-O atom layers are observed which parallel distributed over the entire sample, caused by the incident gold ions. The figure is adopted from Ref. 115.

The oxygen annealing after irradiation changes superconducting properties both on T_c and J_c. The suppression of T_c and self-field J_c caused by irradiation can be partially recovered in all annealed samples. At 5 K and 30 K, the in-field J_c enhancement is reduced after annealing, indicating a reduced pinning effect. Interestingly, an increase of in-field J_c was found in all three samples at 77 K. Especially for 2E11 sample, J_c keeps rising after each step of annealing, yields a total enhancement of 184%. For 6E11 sample, though the J_c after annealing doesn't reach a higher value compare to that of the pristine sample, the severe suppression due to the irradiation is almost fully recovered.

It has been reported that T_c and self-field J_c can be recovered to certain level by oxygen annealing after the irradiation[58,102,103,116]. One explanation is that this recovery is due to the structural reconstruction which removes some of the defects caused by irradiation. In this case, annealed samples, if previously irradiated under optimum ion dosages, should consist a reduced in-field J_c due to the reduced pinning centers. It is consistent with the annealing result in 2E11 and 4E11 samples at 5 K and 30 K which show the highest in-field J_c after irradiation.

However, a contradiction is raised. In 6E11 sample the lower in-field J_c enhancement (compared to that of 2E11 and 4E11 samples) is resulted from the over-dosed irradiation which brings too much defects. According to the assumption that the oxygen annealing reduces the defect density, it would be expected to see an in-field J_c increase in 6E11 sample. However, the experimental result doesn't show such a J_c improvement.

This inconsistency indicates that the defect density may not be affected much by oxygen annealing. Here another explanation is proposed. Though it has been reported that annealing can reduced the density of the small defect, such as point defect[117-119], it is also possible that some larger defects, like columnar defects or the splits found in this study which spread through many unit cells, cannot be completely repaired. However, the oxygen annealing, as a process of reconstruction, can cure part of the deformations on the edge of those large defects by releasing the strain. In this case, the oxygen annealing is mainly to reduce the size of the defect, rather than lower the defect density. Defects with reduced size can still pin the vortices and would have less damage to the original crystal structure. This is also in line with the recovered T_c and self-field J_c in annealed samples. There are actually still some small defects in irradiated samples which may be completely removed by annealing, but the amount is very limited as seen in Fig.4.8a. So that the defect density would not change much.

Let's then try to explain what happens in 6E11 sample. The high defect density is considered to be the key factor which limits the in-field J_c enhancement at 5 K and 30 K in irradiated 6E11 sample. Given that the oxygen annealing mainly cuts down the defect size rather than reduces the density, the problem of over-dense pinning centers in 6E11 sample still exists. It is reasonable to see no enhancement on the aspect of in-field J_c at 5 K and 30 K after annealing. At 77 K, the rapid decay of in-field J_c after irradiation is mainly due to the large suppression of T_c in 6E11 – a decrease from 93.5 K to 87 K. Thanks to the smaller defect size after annealing, the T_c recovered back to 91.5 K and the in-field J_c almost returns to that of the pristine sample. The further J_c

enhancement at 77 K in annealed 2E11 and 4E11 samples is also resulted from the reduced damage in the crystal structure. With the partially recovered T_c, the enhanced pinning effect is more obviously seen at this relatively high temperature.

The key to achieve a high in-field J_c is to find a balance between the number of the pining centers and the damage to the crystal structure. The post-oxygen annealing is an effective method to recover part of the irradiation-induced damage by reducing the defect size, without changing the defect density significantly. Thus the major enhanced pinning effect still remains in the annealed sample while the suppression of T_c and self-field J_c becomes less. The J_c enhancement at 77 K is also due to this reconstruction process and the optimum effect can be seen in the 2E11 sample.

In summary, in-field J_c of YBCO coated conductors can be effectively enhanced by 22 MeV gold ion irradiation at varies dosages. The optimum dosage is found to be 2×10^{11} cm^{-2}, corresponding to a defect density of 4.6×10^{19} cm^{-3}. At this dosage, the J_c enhancement under 3 T yields 70%, 98% and 64% at the temperature of 5 K, 30 K and 77 K, respectively. The enhancement comes from the introduced defects which can effectively pin the vortices. The accompanied structural damage leads to a suppression on T_c and self-filed J_c. This suppression can be partially recovered by oxygen post-annealing, which is a structural reconstruction process to reduce the defect size. It further enhances the 77 K in-field J_c of the sample irradiated at the dosage of 2×10^{11} cm^{-2}, with a total enhancement of 184% at 3 T, almost tripled compared to that of the pristine sample. By now this gold ion irradiation technique has been further developed into the reel-to-reel irradiation for 2G coated conductors.

References

[1] H. K. Onnes. *Comm. Phys. Lab. Univ. Leiden*, **120b** (1911).

[2] W. Meissner and R. Ochsenfeld. *Naturwiss* **21**, 787 (1933).

[3] F. London and H. London. *Proc. Roy. Soc.(London)* **A149**, 71 (1935).

[4] V. L. Ginzburg and L. D. Landau. *Zh. Eksp. Teor. Fiz.* **20**, 1064 (1950).

[5] J. Bardeen, L. N. Cooper, and J. R. Schrieffer. *Phys. Rev.* **108**, 1175 (1957).

[6] M. Cyrot and D. Pavuna, *Introduction to Superconductivity and High-Tc materials*. (World Scientific Publishing, 1992).

[7] A. A. Abrikosov. *Zh. Eksp. Teor. Fiz.* **32**, 1442 (1957).

[8] S. R. Foltyn, L. Civale, J. L. Macmanus-Driscoll, Q. X. Jia, B. Maiorov, H. Wang, and M. Maley. *Nat. Mat.* **6**, 631 (2007).

[9] J. G. Bednorz and K. A. Mueller. *Zeitschrift für Physik B* **64**, 189 (1986).

[10] M. K. Wu, J. R. Ashburn, C. J. Torng, P. H. Hor, R. L. Meng, L. Gao, Z. J. Huang, Y. Q. Wang, and C. W. Chu. *Phys. Rev. Lett.* **58**, 908 (1987).

[11] R. J. Cava, B. Batlogg, R. B. Van Dover, D. W. Murphy, S. Sunshine, T. Siegrist, J. P. Remeika, E. A. Rietman, S. Zahurak, and G. P. Espinosa. *Phys. Rev. Lett.* **58**, 1676 (1987).

[12] J. Nagamatsu, N. Nakagawa, T. Muranaka, Y. Zenitani, and J. Akimitsu. *Nature* **410**, 63 (2001).

[13] Y. Kamihara, H. Hiramatsu, M. Hirano, R. Kawamura, H. Yanagi, T. Kamiya, and H. Hosono. *J. Am. Chem. Soc.* **128**, 10012 (2006).

[14] Y. Kamihara, T. Watanabe, M. Hirano, and H. Hosono. *J. Am. Chem. Soc.* **130**, 3296 (2008).

[15] J. W. Lynn and P. Dai. *Physica C: Superconductivity* **469**, 469 (2009).

[16] S. Lee, J. Jiang, Y. Zhang, C. W. Bark, J. D. Weiss, C. Tarantini, C. T. Nelson, H. W. Jang, C. M. Folkman, S. H. Baek, A. Polyanskii, D. Abraimov, A. Yamamoto,

J. W. Park, X. Q. Pan, E. E. Hellstrom, D. C. Larbalestier, and C. B. Eom. *Nat. Mat.* **9**, 397 (2010).

[17] J.-F. Ge, Z.-L. Liu, C. Liu, C.-L. Gao, D. Qian, Q.-K. Xue, Y. Liu, and J.-F. Jia. *Nat. Mat.* **14**, 285 (2015).

[18] W. Si, S. J. Han, X. Shi, S. N. Ehrlich, J. Jaroszynski, A. Goyal, and Q. Li. *Nat. Commun.* **4**, 1347 (2013).

[19] Q. Li, W. Si, and I. K. Dimitrov. *Rep. Prog. Phys.* **74**, 124510 (2011).

[20] E. H. Brandt. *Rep. Prog. Phys* **58**, 1465 (1995).

[21] C. L. Briant, E. L. Hall, K. W. Lay, and I. E. Tkaczyk. *J. Mater.Res.* **9**, 2789 (1994).

[22] T. P. Beales, J. Jutson, L. Le Lay, and M. Molgg. *J. Mater. Chem.* **7**, 653 (1997).

[23] C. Blue and P. Boolchand. *Appl. Phys. Lett.* **58**, 2036 (1991).

[24] N. Savvides and A. Katsaros. *Appl. Phys. Lett.* **62**, 528 (1993).

[25] R. P. Reade, P. Berdahl, R. E. Russo, and S. M. Garrison. *Appl. Phys. Lett.* **61**, 2231 (1992).

[26] R. E. Russo, R. P. Reade, J. M. Mcmillan, and B. L. Olsen. *J. Appl. Phys.* **68**, 1354 (1990).

[27] Y. Iijima, N. Tanabe, O. Kohno, and Y. Ikeno. *Appl. Phys. Lett.* **60**, 769 (1992).

[28] A. Goyal, D. P. Norton, J. D. Budai, M. Paranthaman, E. D. Specht, D. M. Kroeger, D. K. Christen, Q. He, B. Saffian, F. A. List, D. F. Lee, P. M. Martin, C. E. Klabunde, E. Hartfield, and V. K. Sikka. *Appl. Phys. Lett.* **69**, 1795 (1996).

[29] S. Gnanarajan, A. Katsaros, and N. Savvides. *Appl. Phys. Lett.* **70**, 2816 (1997).

[30] A. Goyal, M. P. Paranthaman, and U. Schoop. *MRS Bull.* **29**, 552

[31] http://www.superpower-inc.com/content/2g-hts-wire; http://brookhaventech.com/technolgies/2g-cable/

[32] S. R. Foltyn, P. N. Arendt, P. C. Dowden, R. F. Depaula, J. R. Groves, J. Y. Coulter, J. Quanxi, M. P. Maley, and D. E. Peterson. *IEEE Trans. on Appl. Supercond.* **9**, 1519 (1999).

[33] H. Liu, G. Li, H. Zhang, and Y. Wang. *IEEE Trans. on Appl. Supercond.* **25**, 1 (2015).

[34] V. Selvamanickam, M. H. Gharahcheshmeh, A. Xu, Y. Zhang, and E. Galstyan. *Supercond. Sci. Tech.* **28**, 072002 (2015).

[35] U. Floegel-Delor, T. Riedel, P. Schirrmeister, D. Wippich, R. Rothfeld, R. Koenig, and F. N. Werfel. *IEEE Trans. on Appl. Supercond.* **25**, 1 (2015).

[36] G. A., *Second-Generation HTS Conductors*. (Springer US, 2005).

[37] U. Floegel-Delor, T. Riedel, R. Rothfeld, P. Schirrmeister, R. Koenig, and F. N. Werfel. *IEEE Trans. on Appl. Supercond.* **26**, 1 (2016).

[38] F. C. Hsu, J. Y. Luo, K. W. Yeh, T. K. Chen, T. W. Huang, P. M. Wu, Y. C. Lee, Y. L. Huang, Y. Y. Chu, D. C. Yan, and M. K. Wu. *PNAS* **105**, 14262 (2008).

[39] M. H. Fang, H. M. Pham, B. Qian, T. J. Liu, E. K. Vehstedt, Y. Liu, L. Spinu, and Z. Q. Mao. *Phys. Rev. B* **78**, 224503 (2008).

[40] T. J. Liu, J. Hu, B. Qian, D. Fobes, Z. Q. Mao, W. Bao, M. Reehuis, S. a. J. Kimber, K. Prokeš, S. Matas, D. N. Argyriou, A. Hiess, A. Rotaru, H. Pham, L. Spinu, Y. Qiu, V. Thampy, A. T. Savici, J. A. Rodriguez, and C. Broholm. *Nat. Mat.* **9**, 718 (2010).

[41] S. Margadonna, Y. Takabayashi, Y. Ohishi, Y. Mizuguchi, Y. Takano, T. Kagayama, T. Nakagawa, M. Takata, and K. Prassides. *Phys. Rev. B* **80**, 064506 (2009).

[42] E. Bellingeri, R. Buzio, A. Gerbi, D. Marrè, S. Congiu, M. R. Cimberle, M. Tropeano, A. S. Siri, A. Palenzona, and C. Ferdeghini. *Supercond. Sci. Tech.* **22**, 105007 (2009).

[43] E. Bellingeri, I. Pallecchi, R. Buzio, A. Gerbi, D. Marrè, M. R. Cimberle, M. Tropeano, M. Putti, A. Palenzona, S. Kaciulis, and C. Ferdeghini. *J. Supercond. Nov. Mag.* **24**, 35 (2010).

[44] E. Bellingeri, S. Kawale, V. Braccini, R. Buzio, A. Gerbi, A. Martinelli, M. Putti, I. Pallecchi, G. Balestrino, A. Tebano, and C. Ferdeghini. *Supercond. Sci. Tech.* **25**, 084022 (2012).

[45] E. Bellingeri, S. Kawale, I. Pallecchi, A. Gerbi, R. Buzio, V. Braccini, A. Palenzona, M. Putti, M. Adamo, E. Sarnelli, and C. Ferdeghini. *Appl. Phys. Lett.* **100**, 082601 (2012).

[46] J. L. Macmanus-Driscoll, S. R. Foltyn, Q. X. Jia, H. Wang, A. Serquis, L. Civale, B. Maiorov, M. E. Hawley, M. P. Maley, and D. E. Peterson. *Nat. Mat.* **3**, 439 (2004).

[47] J. Gutierrez, A. Llordes, J. Gazquez, M. Gibert, N. Roma, S. Ricart, A. Pomar, F. Sandiumenge, N. Mestres, T. Puig, and X. Obradors. *Nat. Mat.* **6**, 367 (2007).

[48] B. Maiorov, S. A. Baily, H. Zhou, O. Ugurlu, J. A. Kennison, P. C. Dowden, T. G. Holesinger, S. R. Foltyn, and L. Civale. *Nat. Mat.* **8**, 398 (2009).

[49] L. Civale, A. D. Marwick, T. K. Worthington, M. A. Kirk, J. R. Thompson, L. Krusin-Elbaum, Y. Sun, J. R. Clem, and F. Holtzberg. *Phys. Rev. Lett.* **67**, 648 (1991).

[50] M. Miura, B. Maiorov, T. Kato, T. Shimode, K. Wada, S. Adachi, and K. Tanabe. *Nat. commun.* **4** (2013).

[51] B. Roas, B. Hensel, G. Saemann‐Ischenko, and L. Schultz. *Appl. Phys. Lett.* **54**, 1051 (1989).

[52] H. Matsui, H. Ogiso, H. Yamasaki, T. Kumagai, M. Sohma, I. Yamaguchi, and T. Manabe. *Appl. Phys. Lett.* **101**, 232601 (2012).

[53] B. Roas, B. Hensel, S. Henke, S. Klaumünzer, B. Kabius, W. Watanabe, G. Saemann-Ischenko, L. Schultz, and K. Urban. *EPL* **11**, 669 (1990).

[54] V. Hardy, D. Groult, M. Hervieu, J. Provost, B. Raveau, and S. Bouffard. *Nucl. Instr. Meth. Phys. Res. B* **54**, 472 (1991).

[55] M. Toulemonde, S. Bouffard, and F. Studer. *Nucl. Instr. Meth. Phys. Res.B* **91**, 108 (1994).

[56] Y. Zhu, Z. X. Cai, R. C. Budhani, M. Suenaga, and D. O. Welch. *Phys. Rev. B* **48**, 6436 (1993).

[57] W. N. Kang, D. H. Kim, S. Y. Shim, J. H. Park, T. S. Hahn, S. S. Choi, W. C. Lee, J. D. Hettinger, K. E. Gray, and B. Glagola. *Phys. Rev. Lett.* **76**, 2993 (1996).

[58] D. Behera, T. Mohanty, S. K. Dash, T. Banerjee, D. Kanjilal, and N. C. Mishra. *Radiat. Meas.* **36**, 125 (2003).

[59] E. Mezzetti, R. Cherubini, R. Gerbaldo, G. Ghigo, L. Gozzelino, and B. Minetti. *Il Nuovo Cimento D* **18**, 1099 (1996).

[60] D. X. Huang, Y. Sasaki, S. Okayasu, T. Aruga, K. Hojou, and Y. Ikuhara. *Phys. Rev. B* **57**, 13907 (1998).

[61] M. Frischherz, M. Kirk, J. Zhang, and H. Weber. *Philos. Mag. A* **67**, 1347 (1993).

[62] Y. Jia, M. Leroux, D. J. Miller, J. G. Wen, W. K. Kwok, U. Welp, M. W. Rupich, X. Li, S. Sathyamurthy, S. Fleshler, A. P. Malozemoff, A. Kayani, O. Ayala-Valenzuela, and L. Civale. *Appl. Phys. Lett.* **103**, 122601 (2013).

[63] M. W. Rupich, S. Sathyamurthy, S. Fleshler, Q. Li, V. Solovyov, T. Ozaki, U. Welp, W. K. Kwok, M. Leroux, A. E. Koshelev, D. J. Miller, K. Kihlstrom, L. Civale, S. Eley, and A. Kayani. *IEEE Trans. on Appl. Supercond.* **26**, 1 (2016).

[64] T. Tsuyoshi, T. Toshihiro, Y. Hidenori, T. Yuji, M. Shyam, T. Tomotaka, N. Yasuyuki, O. Satoru, S. Masato, K. Hisashi, M. Takeshi, K. Tadashi, and K. Yasuyuki. *Supercond. Sci. Tech.* **25**, 084008 (2012).

[65] L. Fang, Y. Jia, C. Chaparro, G. Sheet, H. Claus, M. A. Kirk, A. E. Koshelev, U. Welp, G. W. Crabtree, W. K. Kwok, S. Zhu, H. F. Hu, J. M. Zuo, H.-H. Wen, and B. Shen. *Appl. Phys. Lett.* **101**, 012601 (2012).

[66] L. Fang, Y. Jia, V. Mishra, C. Chaparro, V. K. Vlasko-Vlasov, A. E. Koshelev, U. Welp, G. W. Crabtree, S. Zhu, N. D. Zhigadlo, S. Katrych, J. Karpinski, and W. K. Kwok. *Nat. commun.* **4** (2013).

[67] T. Taen, Y. Nakajima, T. Tamegai, and H. Kitamura. *Phys. Rev. B* **86**, 094527 (2012).

[68] Y. Nakajima, T. Taen, Y. Tsuchiya, T. Tamegai, H. Kitamura, and T. Murakami. *Phys. Rev. B* **82**, 220504 (2010).

[69] M. Eisterer, R. Raunicher, H. W. Weber, E. Bellingeri, M. R. Cimberle, I. Pallecchi, M. Putti, and C. Ferdeghini. *Supercond. Sci. Tech.* **24**, 065016 (2011).

[70] B. Maiorov, T. Katase, I. O. Usov, M. Weigand, L. Civale, H. Hiramatsu, and H. Hosono. *Phys. Rev. B* **86**, 094513 (2012).

[71] V. Ginzburg. *Soviet Physics Jetp-Ussr* **4**, 153 (1957).

[72] S. Saxena, P. Agarwal, K. Ahilan, F. Grosche, R. Haselwimmer, M. Steiner, E. Pugh, I. Walker, S. Julian, and P. Monthoux. *Nature* **406**, 587 (2000).

[73] E. Sonin and I. Felner. *Phys. Rev. B* **57**, R14000 (1998).

[74] T. Kontos, M. Aprili, J. Lesueur, and X. Grison. *Phys. Rev. Lett.* **86**, 304 (2001).

[75] A. I. Buzdin. *Rev. Mod. Phys.* **77**, 935 (2005).

[76] N. F. Berk and J. R. Schrieffer. *Phys. Rev. Lett.* **17**, 433 (1966).

[77] E. A. Yelland, S. M. Hayden, S. J. C. Yates, C. Pfleiderer, M. Uhlarz, R. Vollmer, H. V. Löhneysen, N. R. Bernhoeft, R. P. Smith, S. S. Saxena, and N. Kimura. *Phys. Rev. B* **72**, 214523 (2005).

[78] Y. A. Izyumov, Y. N. Proshin, and M. G. Khusainov. *Uspekhi Fizicheskih Nauk* **172**, 113 (2002).

[79] H. R. Khan and C. J. Raub. *Annual Rev. of Mater. Sci.* **15**, 211 (1985).

[80] J. W. Lynn, G. Shirane, W. Thomlinson, and R. N. Shelton. *Phys. Rev. Lett.* **46**, 368 (1981).

[81] A. I. Goldman, C. Stassis, P. C. Canfield, J. Zarestky, P. Dervenagas, B. K. Cho, D. C. Johnston, and B. Sternlieb. *Phys. Rev. B* **50**, 9668 (1994).

[82] V. A. Vas'ko, V. A. Larkin, P. A. Kraus, K. R. Nikolaev, D. E. Grupp, C. A. Nordman, and A. M. Goldman. *Phys. Rev. Lett.* **78**, 1134 (1997).

[83] R. P. Panguluri, K. C. Ku, T. Wojtowicz, X. Liu, J. K. Furdyna, Y. B. Lyanda-Geller, N. Samarth, and B. Nadgorny. *Phys. Rev. B* **72**, 054510 (2005).

[84] D. Samal and P. S. Anil Kumar. *J. Appl. Phys.* **109**, 07E129 (2011).

[85] T. J. Liu, X. Ke, B. Qian, J. Hu, D. Fobes, E. K. Vehstedt, H. Pham, J. H. Yang, M. H. Fang, L. Spinu, P. Schiffer, Y. Liu, and Z. Q. Mao. *Phys. Rev. B* **80**, 174509 (2009).

[86] T. M. Mcqueen, Q. Huang, V. Ksenofontov, C. Felser, Q. Xu, H. Zandbergen, Y. S. Hor, J. Allred, A. J. Williams, D. Qu, J. Checkelsky, N. P. Ong, and R. J. Cava. *Phys. Rev. B* **79**, 014522 (2009).

[87] L. Zhang, D. J. Singh, and M. H. Du. *Phys. Rev. B* **79**, 012506 (2009).

[88] Y. Mizuguchi, K. Deguchi, S. Tsuda, T. Yamaguchi, and Y. Takano. *Phys. Rev. B* **81**, 214510 (2010).

[89] T. Noji, T. Suzuki, H. Abe, T. Adachi, M. Kato, and Y. Koike. *J. Phys. Soc. Jpn.* **79**, 084711 (2010).

[90] K. Deguchi, Y. Mizuguchi, Y. Kawasaki, T. Ozaki, S. Tsuda, T. Yamaguchi, and Y. Takano. *Supercond. Sci. Tech.* **24**, 055008 (2011).

[91] Y. Mizuguchi, K. Deguchi, Y. Kawasaki, T. Ozaki, M. Nagao, S. Tsuda, T. Yamaguchi, and Y. Takano. *J. Appl Phys.* **109**, 013914 (2011).

[92] K. Deguchi, D. Sato, M. Sugimoto, H. Hara, Y. Kawasaki, S. Demura, T. Watanabe, S. J. Denholme, H. Okazaki, T. Ozaki, T. Yamaguchi, H. Takeya, T. Soga, M. Tomita, and Y. Takano. *Supercond. Sci. Tech.* **25**, 084025 (2012).

[93] Y. Kawasaki, K. Deguchi, S. Demura, T. Watanabe, H. Okazaki, T. Ozaki, T. Yamaguchi, H. Takeya, and Y. Takano. *Solid State Commun.* **152**, 1135 (2012).

[94] Y. Sun, T. Taen, Y. Tsuchiya, Z. X. Shi, and T. Tamegai. *Supercond. Sci. Tech.* **26**, 015015 (2013).

[95] Y. Sun, Y. Tsuchiya, T. Taen, T. Yamada, S. Pyon, A. Sugimoto, T. Ekino, Z. Shi, and T. Tamegai. *Sci. Rep.* **4**, 4585 (2014).

[96] L. Zhi, P. Jun-Ping, Z. Hui-Min, Z. Wen-Hao, D. Hao, D. Peng, C. Kai, S. Can-Li, J. Shuai-Hua, W. Lili, H. Ke, C. Xi, X. Qi-Kun, and M. Xu-Cun. *J. Phys. Condens. Matter* **26**, 265002 (2014).

[97] A. Xu, J. J. Jaroszynski, F. Kametani, Z. Chen, D. C. Larbalestier, Y. L. Viouchkov, Y. Chen, Y. Xie, and V. Selvamanickam. *Supercond. Sci. Tech.* **23**, 014003 (2010).

[98] Z. Chen, F. Kametani, Y. Chen, Y. Xie, V. Selvamanickam, and D. C. Larbalestier. *Supercond. Sci. Tech.* **22**, 055013 (2009).

[99] D. Dijkkamp, T. Venkatesan, X. D. Wu, S. A. Shaheen, N. Jisrawi, Y. H. Min - Lee, W. L. Mclean, and M. Croft. *Appl. Phys. Lett.* **51**, 619 (1987).

[100] http://groups.ist.utl.pt/rschwarz/rschwarzgroup_files/PLD_files/PLD_schem.jpg

[101] J. F. Ziegler. *Nucl. Instr. Meth. Phys. Res. B* **219–220**, 1027 (2004).

[102] S. Vadlamannati, P. England, N. G. Stoffel, R. Ramesh, T. S. Ravi, D. M. Hwang, A. Findikoglu, Q. Li, T. Venkatesan, and W. L. Mclean. *Appl. Phys. Lett.* **57**, 2265 (1990).

[103] F. M. Sauerzopf. *Phys. Rev. B* **57**, 10959 (1998).

[104] C. P. Bean. *Rev. Mod. Phys.* **36**, 31 (1964).

[105] J. Jaroszynski, F. Hunte, L. Balicas, Y.-J. Jo, I. Raičević, A. Gurevich, D. C. Larbalestier, F. F. Balakirev, L. Fang, P. Cheng, Y. Jia, and H. H. Wen. *Phys. Rev. B* **78**, 174523 (2008).

[106] N. R. Werthamer, E. Helfand, and P. C. Hohenberg. *Phys. Rev.* **147**, 295 (1966).

[107] R. D. Zhong, J. A. Schneeloch, X. Y. Shi, Z. J. Xu, C. Zhang, J. M. Tranquada, Q. Li, and G. D. Gu. *Phys. Rev. B* **88**, 020505 (2013).

[108] Y. Mizuguchi, F. Tomioka, S. Tsuda, T. Yamaguchi, and Y. Takano. *Appl. Phys. Lett.* **94**, 012503 (2009).

[109] H. Meissner. *Phys. Rev.* **117**, 672 (1960).

[110] T. Ozaki, L. Wu, C. Zhang, J. Jaroszynski, W. Si, J. Zhou, Y. Zhu, and Q. Li, *A route for a strong increase of critical current in nano strained iron-based superconductors, Nat. Commun.* (accepted).

[111] R. M. Scanlan, W. A. Fietz, and E. F. Koch. *Journal of Appl. Phys.* **46**, 2244 (1975).

[112] D. C. Larbalestier and A. W. West. *Acta Mater.* **32**, 1871 (1984).

[113] L. D. Cooley, P. J. Lee, and D. C. Larbalestier. *Phys. Rev. B* **53**, 6638 (1996).

[114] A. Godeke. *Supercond. Sci. Tech.* **19**, R68 (2006).

[115] Q. Li, *Doubling in-field critical current in HTS coated conductors by a roll-to-roll ion irradiation process, MRS Spring Meeting 2016 in Phoenix,***EP13** (2016).

[116] K. Nakashima, N. Chikumoto, A. Ibi, S. Miyata, Y. Yamada, T. Kubo, A. Suzuki, and T. Terai. *Physica C: Superconductivity* **463**, 665 (2007).

[117] P. X. Zhang, L. Zhou, P. Ji, W. M. Blan, X. Z. Wu, and Z. H. Lai. *Supercond. Sci. Tech.* **8**, 15 (1995).

[118] V. F. Solovpov, H. J. Wiesmann, W. Li-Jun, M. Suenaga, and R. Feenstra. *IEEE Trans. on Appl. Supercond.* **9**, 1467 (1999).

[119] M. A. Kirk. *Cryogenics* **33**, 235 (1993).